



EPFL

Politecnico di Torino

Collegio di Ingegneria Chimica e dei Materiali

Corso di Laurea Magistrale
in Ingegneria dei Materiali

Tesi di Laurea Magistrale

**Carbon-Inorganic Multilayered Coatings
from Reactive Precursors**

Supervisors:

Dr. Bomal Enzo

Prof. Frauenrath Holger

External supervisor

Prof.ssa Bongiovanni Roberta Maria

Academic year 2020/2021

Riassunto

Introduzione

Il seguente lavoro di tesi ha come scopo la formazione e la caratterizzazione di *nanocoating* organometallici multistrato ottenuti da precursori molecolari, capaci di reticolare in strutture carboniose mediante il solo irraggiamento ultravioletto.

Il progetto illustrato nel seguente manoscritto è introdotto da un capitolo che descriverà lo stato dell'arte dei nanomateriali carboniosi, soffermandosi in particolare sulle principali tecniche di sintesi organica volte all'ottenimento di nanostrutture zero- e mono-dimensionali.

Verrà successivamente presentato il concetto di monostrato autoassemblante da precursori organici e la successiva trasformazione in una nanostruttura carboniosa mediante trattamenti termici o elettronici. Verranno infine introdotti i sistemi oligoinici e le tecniche di sintesi volte alla loro produzione. Tali sistemi, se opportunamente funzionalizzati, possono presentare fenomeni di *self-assembly* volti formazione di monostrati. A causa dell'elevata instabilità della catena insatura, tali strutture aggregate presentano un'elevata tendenza alla reticolazione e alla successiva carbonizzazione, grazie al solo contributo di una radiazione ultravioletta. In particolare, presso il laboratorio di materiali organici e macromolecolari dell'università politecnica federale di Losanna, da recenti ricerche sono state ottenute nanomembrane carboniose tramite l'utilizzo di esini anfifilici asimmetrici, capaci di formare monostrati su superfici ossidiche grazie alla presenza di un gruppo terminale acido e di carbonizzare a seguito di esposizione a radiazione ultravioletta. Tali nanostrutture, seppur caratterizzate da spessori dell'ordine dei nanometri, presentano elevate proprietà barriera, sia contro fenomeni corrosivi sia verso una ridotta generazione di elettroni secondari. L'utilizzo di surfactanti poliinici simmetrici, contraddistinti ovvero da gruppi terminali uguali, permetterebbe l'ottenimento di *coating* autoassemblanti organici multistrato. Come riportato nella letteratura scientifica, tali strutture possono essere ottenute utilizzando acidi organici difosfonici e cationi metallici. L'introduzione di gruppo fosfonici terminali a una struttura esinica garantirebbe un precursore capace di autoassemblarsi in strutture multistrato, oltre a poter essere trasformate in un nanomateriale carbonioso, mediante esposizione a radiazione ultravioletta.

Il lavoro sperimentale ha dunque l'obiettivo di ottenere, in prima battuta, un surfactante bolaanfifilico, caratterizzato da un nucleo centrale poliinico e da due gruppi terminali

fosfonati. Verrà successivamente valutata la tendenza del precursore a formare monostrati autoassemblanti su superfici ossidiche. Successivamente, si studierà la formazione di strutture multistrato mediante tecnica layer-by-layer, sfruttando l'utilizzo di un catione metallico come elemento pontante tra diversi monostrati organici. Verrà valutata la conversione del multistrato organico in un nanomateriale carbonioso mediante irraggiamento ultravioletto, e verrà analizzata la natura del materiale ottenuto. Infine, verranno quantificate le proprietà anticorrosive introdotte dalla nanostruttura su superfici di alluminio.

Parte sperimentale

Il surfactante oligoinico, l'acido esadeca-3,5,7,9,11,13-esin-1,16-difosfonico, è stato sintetizzato mediante 6 passaggi, seguendo la procedura di sintesi schematizzata in **Fig. 1**.

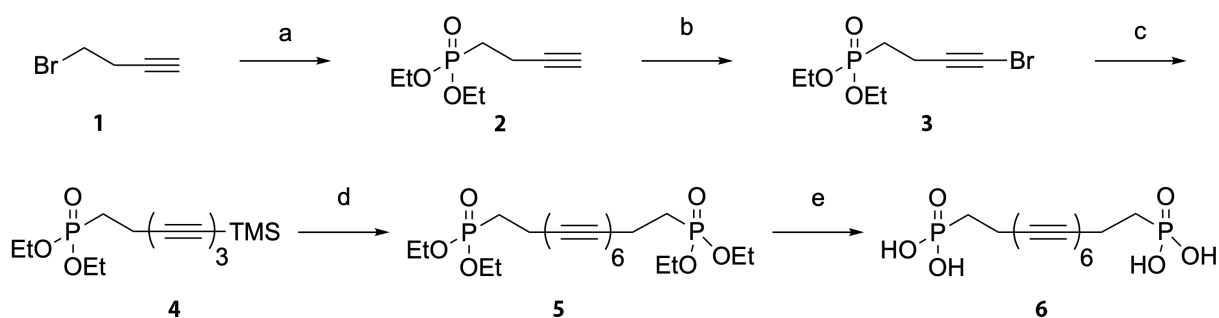


Fig. 1: Sintesi dell'acido esadeca-3,5,7,9,11,13-esin-1,16-difosfonico. Reagenti e condizioni descritti in dettaglio nel corpo principale della tesi.

Il 4-bromo-1-butino è stato scelto inizialmente sottoposto a una reazione di sostituzione di Michaelis-Becker, la quale ha permesso l'introduzione del gruppo fosfonato al posto del bromo terminale, con una resa stimata intorno al 35%.

L'alchino terminale ottenuto è stato bromurato tramite l'aggiunta di *N*-bromosuccinamide in presenza di nitrato d'argento come catalizzatore, con una resa del 90%. La presenza di un gruppo alogeno terminale è necessaria alla successiva reazione di accoppiamento ossidativo di Negishi con l'1,4-di(trimetilsilil)butadiino. Tale reazione, effettuata in due passaggi paralleli, necessita da un lato l'ottenimento dell'organozinco dal butadiino, dall'altro l'attivazione del palladio mediante riduzione, da +2 a 0, ottenuta tramite l'aggiunta di butilitio. L'introduzione contemporanea sia dell'organozinco che dell'alchino alogenato nella soluzione contenente il catalizzatore attivato ha permesso la formazione del trieno, con una resa del 76%.

La formazione dell'esino è stata effettuata mediante la procedura di accoppiamento di Eglinton-Galbraith, catalizzata da acetato di rame. Successivi step di purificazione hanno reso possibile l'ottenimento dell'oligoino protetto con una resa del 76%. La protezione offerta dai gruppi etilici terminali permette un miglior controllo sulla carbonizzazione incontrollata dell'esino. Una frazione di prodotto è stata sottoposta a cristallizzazione tramite lenta evaporazione del solvente a - 17 °C. La frazione cristallina ottenuta, caratterizzata da un aspetto aghiforme, è stata analizzata mediante tecnica cristallografica a raggi X. I risultati, riportati in **Fig. 2**, mostrano la struttura del precursore molecolare e la struttura della cella cristallina formata, contraddistinta dalla formazione di dimeri e dalla loro disposizione a spina di pesce. La lunghezza della catena carboniosa è stata valutata attorno a 2 nm, come distanza tra i due atomi di fosforo presenti all'interno della molecola.

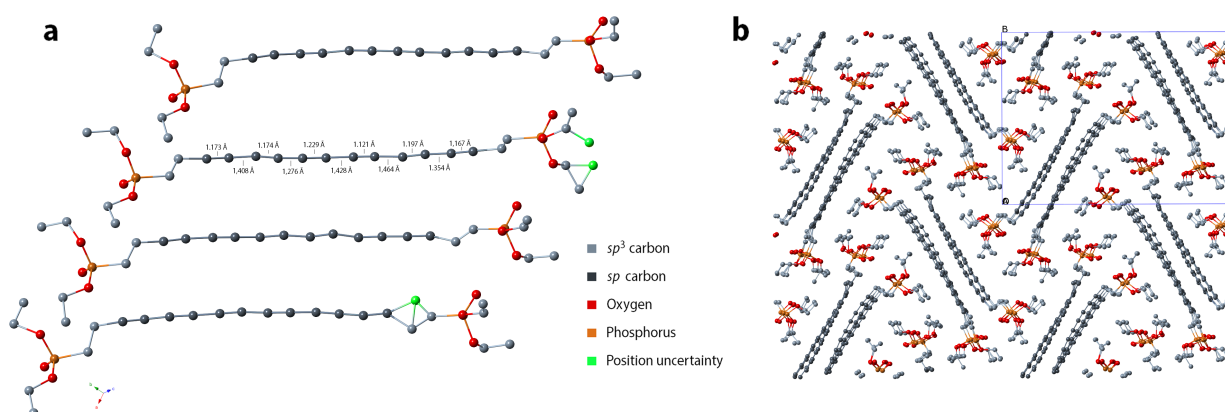


Fig. 2. **a.** Cluster del precursore carbonioso protetto dai gruppi fosfonati. Gli atomi rappresentati in verde rappresentano indeterminazione sulla posizione atomica.
b. Struttura cristallina assunta dalla molecola. Notasi la struttura a spina di pesce assunta dai dimeri oligoioinici.

La rimozione dei frammenti etilici a protezione dell'oligoino è stata effettuata mediante l'introduzione di una quantità in eccesso di TMS-Br. La successiva aggiunta di HCl 1 M ha permesso la precipitazione del prodotto deprotetto sotto forma di una polvere gialla altamente reattiva, che è stata velocemente filtrata e introdotta in una soluzione di metanolo e diclorometano per evitare l'insorgenza di fenomeni degradativi.

La resa del prodotto è stata determinata in maniera indiretta mediante una titolazione spettroscopica UV-Vis della soluzione ottenuta nello step precedente, applicando la legge di Lambert-Beer e conoscendo, da precedenti studi effettuati dal gruppo, il coefficiente di estinzione molare della struttura esinica, pari a $3 \cdot 10^6 \text{ cm}^{-1} \text{ M}^{-1}$. È stata riscontrata una concentrazione di 5.8 mM, equivalente a 0.174 mmol di prodotto e a una resa del 19%.

Tab. 1: Misure di angolo di contatto e ellipsometria di monostrati ottenuti per immersione a diverse concentrazioni e temperature.

	R.T	R.T	R.T	60 °C	60 °C	60 °C
	2 mM	0.2 mM	0.002 mM	2 mM	0.2 mM	0.002 mM
Angolo di contatto [°]	70 ± 1	66 ± 1	54 ± 2	67 ± 1	53 ± 2	61 ± 1
Ellipsometria [nm]	3.0 ± 0.3	1.2 ± 0.4	0.4 ± 0.2	3.9 ± 0.4	1.8 ± 0.2	1.0 ± 0.2

Successivamente è stata dimostrata la formazione di una struttura multistrato mediante approccio LbL: alla formazione del *monolayer* organico è seguita l'immersione del substrato in una soluzione 5 mM di acetilacetionato di zirconio $[Zr(AcAc)_4]$ in etanolo. È stato scelto lo zirconio come catione metallico per via dell'elevata tendenza a formare complessi con i gruppi fosfato, sia grazie alla buona solubilità del sale scelto in solventi polari. La saturazione dei legami superficiali porta alla formazione un monostrato costituito da cationi metallici complessati, avente carica residua positiva. A seguito di un'ulteriore immersione nella soluzione del precursore organico, la nascita di nuovi legami coordinativi con l'acido difosfonico favorisce lo sviluppo di un secondo monostrato organico. Il processo ciclico di immersione nelle due soluzioni può dunque essere ripetuto n volte per generare strutture multistrato di natura organometallica, identificate con la sigla $(PA\text{-}hex\text{-}PA/Zr^{4+})_n$. La struttura è terminata con la formazione di un monostrato terminale di acido octadecilfosfonico, in grado di ridurre sensibilmente l'energia superficiale della superficie, conferendole proprietà idrofobiche.

Come rappresentato in **Fig. 4**, i test ellipsometrici hanno dimostrato un incremento pressoché lineare dello spessore del *coating* all'aumentare del numero di strati di $(PA\text{-}hex\text{-}PA/Zr^{4+})$ depositati. È stato misurato un aumento progressivo di circa 4 nm per ogni ciclo di deposizione, segno dell'efficacia della tecnica LbL nella formazione del multistrato.

Successivamente, la presenza di difetti nella struttura multistrato è stata valutata mediante test di angolo di contatto statico e spettroscopie infrarosse di riflessione-assorbimento (IRRA).

È opportuno ricordare che, in un monostrato di acido octadecilfosfonico correttamente formato, le catene alchiliche terminali cristallizzano parzialmente. Tale monostrato, oltre a essere caratterizzato da angoli di contatto di 108-110°, presenta due picchi IR a 2850 e a 2920 cm^{-1} , dovuti rispettivamente dello stretching simmetrico e asimmetrico dei gruppi $-CH_2-$. Eventuali errori nella formazione del monostrato, a causa di difetti preesistenti negli strati

adsorbiti sottostanti, ridurrebbero la cristallinità delle catene alchiliche terminali, generando valori di angolo di contatto inferiori. Tali difetti di impacchettamento si ripercuoterebbero anche nella risposta ottica infrarossa, generando uno shift dei picchi a numeri d'onda più elevati. Dai test effettuati è stato riscontrato un angolo di contatto di circa 105° , indipendentemente dal numero di layer depositato sulla superficie. Ciò significa che, pur presentando difetti conformazionali, l'ulteriore introduzione di strati non peggiora il disordine strutturale del multistrato stesso. I test di spettroscopia IRRA hanno evidenziato i picchi caratteristici delle catene alchiliche a 2854 e a 2925 cm^{-1} per tutti i campioni valutati. Tale osservazione conferma la formazione di un monostrato terminale amorfo, prova di una formazione disordinata della struttura sottostante.

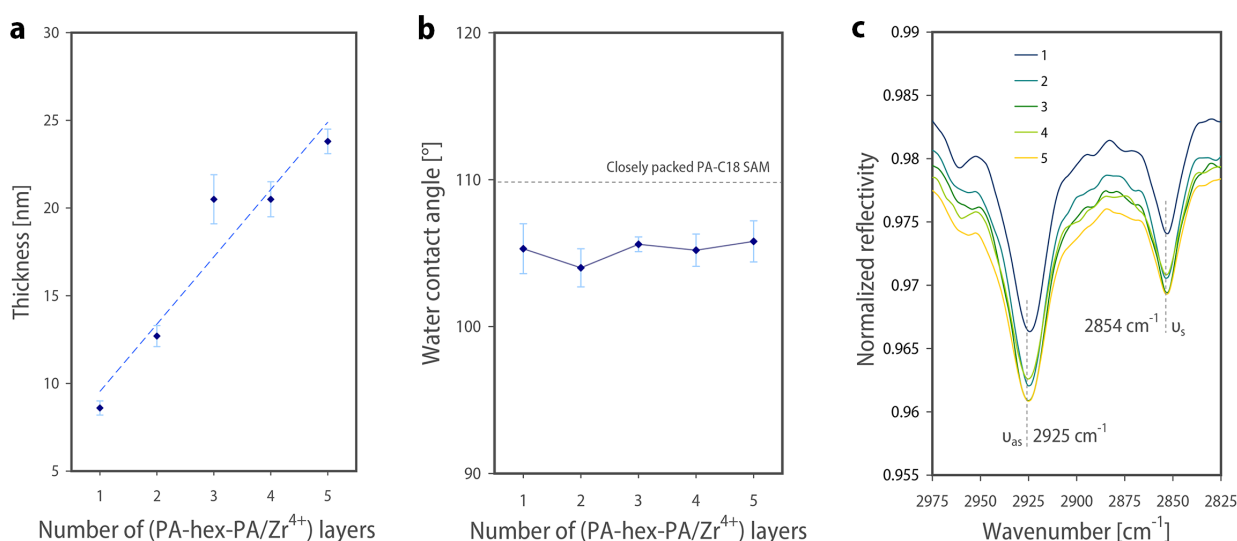


Fig. 4: **a.** Andamento dello spessore del *coating* a seguito dell'aggiunta di strati organometallici **b.** Angoli di contatto valutati all'aumentare del numero di strati depositati. **c.** Spettro IRRA dello stretching simmetrico e asimmetrico delle catene alchiliche presenti al termine delle strutture multistrato.

Confermata la formazione di una struttura multistrato, è stato necessario valutare la conversione del *coating* organometallico in una struttura carboniosa, mediante esposizione a radiazione ultravioletta. Lo studio è stato effettuato su una struttura formata da cinque strati di (PA-hex-PA/Zr⁴⁺), depositati su un substrato di allumina cristallina. L'irraggiamento è stato effettuato in argon, tramite una sorgente UV a 400W posta a una distanza di 20 cm dal campione. A diversi intervalli temporali, il campione è stato analizzato mediante spettroscopia UV-Vis.

La **Fig. 5a** rappresenta la risposta spettroscopica del substrato quando rivestito dal multistrato organico, a confronto con lo spettro ottenuto dall'analisi del precursore oligoinico in soluzione.

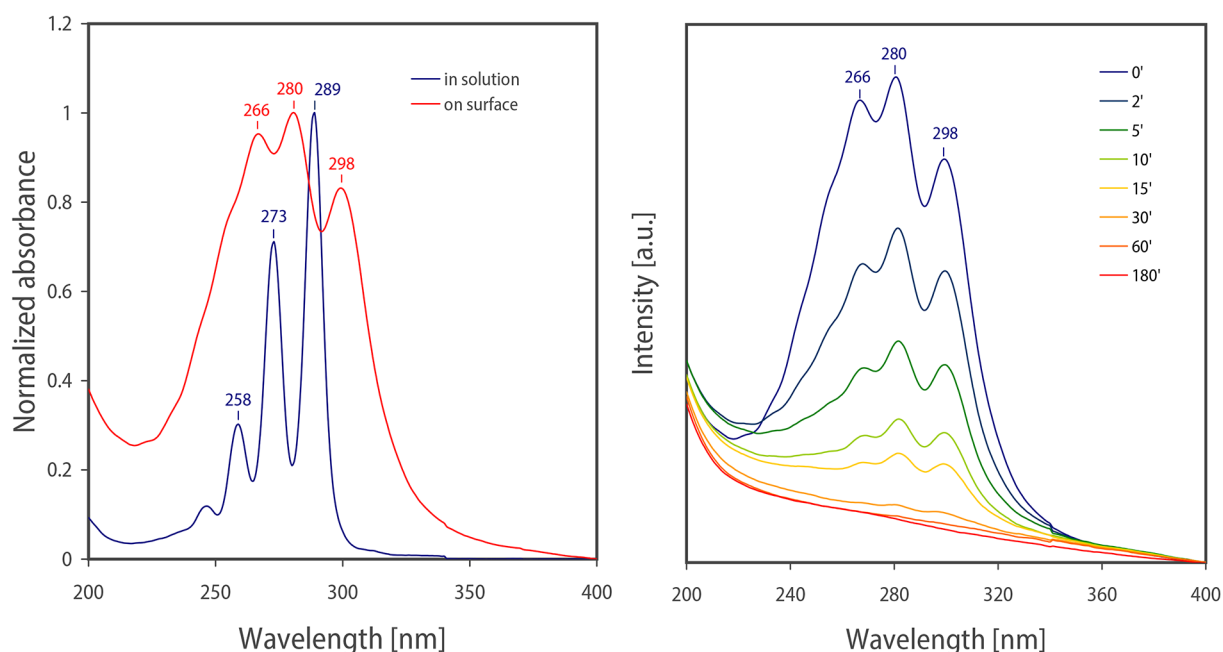


Fig. 5. a. Spettro UV-vis del substrato rivestito da cinque strati di (PA-hex-PA/Zr⁴⁺) sovrapposto allo spettro del precursore molecolare in soluzione. **b.** Evoluzione spettrale del multistrato durante il processo di carbonizzazione

I picchi spettroscopici relativi alla fase condensata mostrano un effetto di *redshift*, assieme ad un significativo aumento di ampiezza del segnale e ad una riduzione del rapporto tra l'intensità del primo e del secondo picco vibronico. Tali fenomeni sono prova della formazione di aggregati-H, a seguito della predominante disposizione cofacciale dei segmenti oligoinici nella struttura multistrato.

Il processo di carbonizzazione, assieme alla conseguente scomparsa della risposta spettrale delle unità oligoiniche, è rappresentato in **Fig. 5b**. Al progredire della dose ricevuta dal substrato, l'estinzione dello spettro oligoinico è segno di una continua trasformazione verso una struttura carbonizzata. La conversione totale avviene a seguito di un irraggiamento di tre ore, che si riduce al 95% a seguito di un'ora di esposizione.

La natura carboniosa del multistrato è stata analizzata mediante spettroscopia Raman. Come rappresentato in **Fig. 6**, lo spettro della struttura carbonizzata mostra i caratteristici picchi G e

D, rispettivamente a 294 cm^{-1} e a 1470 cm^{-1} , caratterizzati da un rapporto tra intensità I_D/I_G pari a circa 0.5. Tali valori sono riconducibili alla formazione di una struttura carboniosa amorfa, caratterizzata da un elevato disordine strutturale, dovuto probabilmente allo sviluppo di anelli grafenici distorti e/o allo sviluppo di strutture cicliche non aromatiche.

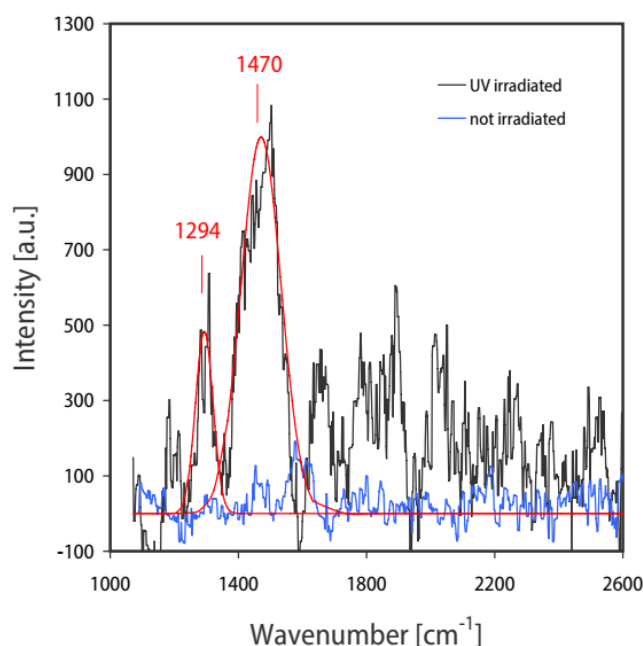


Fig. 6: Spettro Raman della struttura multistrato pre- e post- carbonizzazione

Per valutare eventuali difetti indotti dal processo di carbonizzazione, i precedenti campioni non carbonizzati sono stati sottoposti a irraggiamento UV per un'ora, e successivamente analizzati mediante ellipsometria, angolo di contatto e spettroscopia IRRA.

I risultati, riportati in **Fig. 7**, mostrano un'invarianza dello spessore dei multilayer a seguito di carbonizzazione, mentre il valore di bagnabilità superficiale ricalca gli stessi valori misurati precedentemente a struttura non carbonizzata. Tali risultati dimostrano come il processo di carbonizzazione non induca nella struttura alcun fenomeno di rottura del film o delaminazione. Ciò comporterebbe spessori più elevati, maggiori rugosità superficiale e, di conseguenza, un aumento dell'angolo di contatto, fenomeno che, tuttavia, non è stato osservato. Infine, i picchi IR delle catene alchiliche del monostrato terminale non mostrano variazioni significative pre- e post- carbonizzazione, a prova del fatto che tale processo non comporta la formazione di difetti superficiali e, con essi, un peggioramento della cristallinità del monostrato finale.

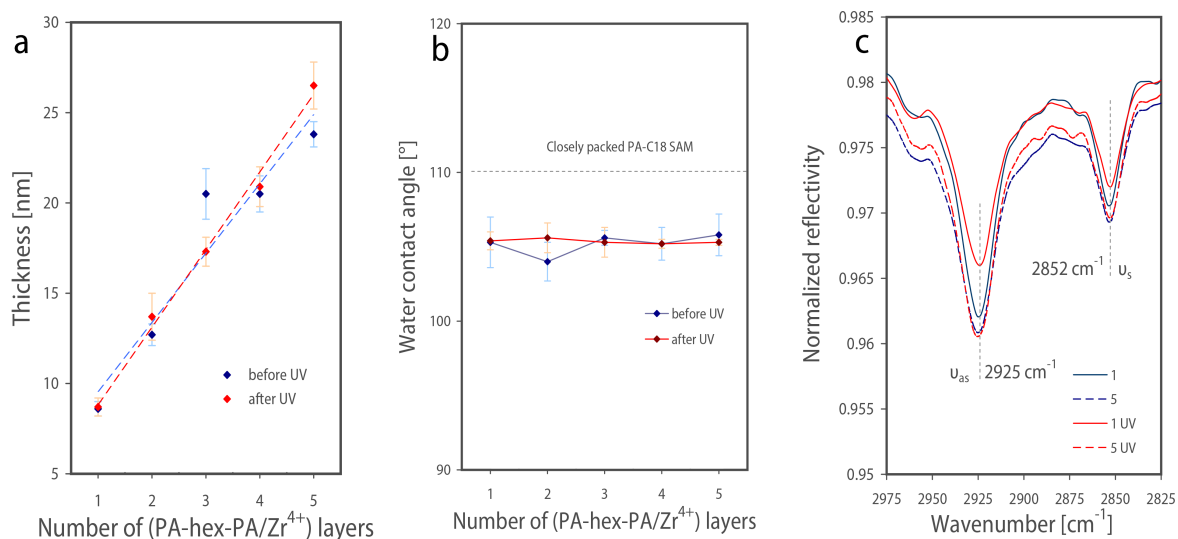


Fig. 7: Comparazione pre- e post- carbonizzazione tra: **a.** spessore del *coating* a diversi strati organometallici depositati, **b.** angoli di contatto su diverse strutture multistrato e **c.** spettri IRRA dei picchi alchilici su diverse strutture formate da uno e cinque monostrati organometallici.

Al fine di determinare la morfologia e la struttura del multistrato, è stata effettuata un'analisi di microscopia elettronica a trasmissione sulla *cross section* di un campione formato da 9 strati e carbonizzato. I risultati di tale analisi sono rappresentati in **Fig. 7**. La struttura carboniosa mostra uno spessore compreso tra 30 e 40 nm, senza segni di delaminazione o rotture, ma piuttosto un'estesa continuità strutturale e un'ottima adesione al substrato. Nonostante la differenza, non marcata, di numero atomico tra il carbonio (12) e lo zirconio (40), nessun contrasto di fase è stato osservato, probabilmente a causa della bassa risoluzione della tecnica o a un disordine strutturale intrinseco del *coating*. L'osservazione di tale differenza avrebbe infatti potuto confermare la corretta formazione di una struttura a strati.

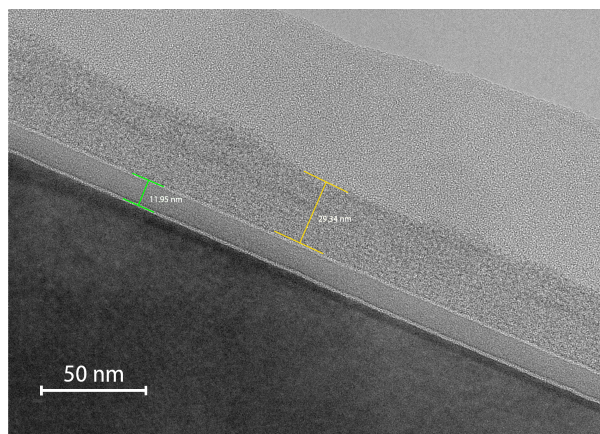


Fig.8: Microscopia a trasmissione di elettroni effettuata sulla *cross section* di una struttura multilayer formata da nove strati.

Come ultima analisi, la proprietà barriera offerta dal multistrato a fenomeni corrosivi è stata valutata. Una struttura multistrato formata da cinque *layer* e terminata con un monostrato di acido octadecilfosfonico è stata depositata su due substrati di alluminio lucidato a specchio. Un campione è stato ulteriormente sottoposto a carbonizzazione. Entrambi i provini, assieme a un campione di alluminio lucidato non trattato, sono stati sottoposti a misure potenziodinamiche. I risultati, riportati in **Tab. 2**, hanno permesso di determinare il potenziale superficiale prima della prova di corrosione, indice della resistenza del substrato a fenomeni degradativi elettrochimici, maggiore a seguito di un aumento positivo del parametro. Ulteriori analisi hanno evidenziato una riduzione pari a di un'ordine di grandezza sia della conduttanza superficiale sia della densità di corrente di corrosione, in riferimento al campione rivestito rispetto al provino di puro alluminio. L'ulteriore carbonizzazione del multistrato non induce un miglioramento delle proprietà barriera, bensì provoca un peggioramento della resistenza alla corrosione rispetto al multistrato non reticolato. Tale fenomeno potrebbe essere imputato all'aumento della rigidità del *coating* a seguito del processo di carbonizzazione, che renderebbe tale struttura sensibilmente più fragile a rotture causate da stress sottostanti, sviluppatasi durante il test potenziodinamico.

Tab. 2: Risultati del test di corrosione effettuati in mediante test potenziodinamico in una soluzione elettrolitica di solfato di sodio 1M, pH 2.

	Potenziale a circuito aperto [V]	Resistenza [MΩ]	Corrente di corrosione [$\mu\text{A cm}^{-2}$]
Alluminio puro	-0.62	0.48	5.10
Multistrato, non carbonizzato	-0.41	6.06	0.30
Multistrato carbonizzato	-0.51	3.28	0.63

Conclusione

Il seguente lavoro di tesi riporta la sintesi di un precursore oligoinico bolaanfifilico, caratterizzato dalla singolare proprietà di generare monostrati molecolari autoassemblanti, e carbonizzare a seguito di esposizione a radiazione ultravioletta. È stata osservata la formazione di un *coating* nanometrico mediante l'applicazione di tecnica LbL, tramite successive immersioni in una soluzione contenente il precursore organico e in una soluzione

di acetilacetato di zirconio. Il multistrato ottenuto è caratterizzato da un certo livello di disordine strutturale, indipendente dal numero di strati adsorbiti. Il processo di reticolazione del multistrato indotto dalla radiazione ultravioletta ha portato alla formazione di una struttura carboniosa amorfa, ben adesa al substrato e esente da fenomeni di delaminazione o rotture.

La presenza del multistrato su substrati di alluminio lucidato ne ha migliorato la resistenza alla corrosione, riducendo di un ordine di grandezza sia la conduttanza superficiale che la corrente di corrosione del substrato, aumentandone al contempo il potenziale superficiale. In tal senso, il processo di carbonizzazione non ha indotto un miglioramento della resistenza a corrosione rispetto al sistema non reticolato.

Ulteriori investigazioni sulla natura a strati del *coating* carbonioso potrebbero essere effettuate mediante analisi HREELS, operata sulla cross section del campione. La singolare proprietà del precursore molecolare nel formare strutture carboniose su superfici ossidiche mediante immersione e successivo irraggiamento UV potrebbe trovare interessanti applicazioni nel campo delle nanoparticelle, specie nella formazione di strutture *core-shell*.

Abstract

The present master thesis focuses on the use of a novel bolaamphiphilic hexayne as a molecular precursor for the formation of hybrid carbon-inorganic nanocoating. The molecule, hexadeca-3,5,7,9,11,13-hexayne-1,16-diylbis(phosphonic acid), displays a central, highly reactive oligoyne segment able to carbonize when exposed to mild UV irradiation at room temperature, while the terminal phosphonic heads lead the molecular to form a self-assembled monolayer onto oxidic surfaces. By introducing a metallic cation, which acts as a bridging element between different organic layers, a multilayer structure can be obtained, and eventually carbonized by UV irradiation.

The target molecule was obtained from 4-bromo-1-butyne, protected at first by diethylphosphonate, followed by bromination of the terminal alkyne, Negishi coupling with 1,4-bis(trimethylsilyl)butadiyne to get the asymmetric triyne, a modified Eglinton-Galbraith homocoupling that furnishes the hexayne, and finally the deprotection of the terminal phosphonates by removal of the ethyl moieties, to furnish the diphosphonic acid.

The self-assembly of the hexayne at the solid-liquid interface was investigated and optimized. Different multilayers were successfully produced by a layer-by-layer approach, as proven by ellipsometry. As displayed by water contact angle and IRRA spectroscopy, the multilayers were characterized by a disordered layered architecture. UV-induced crosslinking turned the organic multilayered structure into a continuous, disordered amorphous carbon coating. TEM analysis proved its nanometric nature, as well as its structural stability and optimal adhesion onto the substrate. As highlighted by potentiodynamic polarization measurements, the metallic-carbon coating, when grown onto aluminum substrates, provided an effective barrier against corrosion, reducing the corrosion current density and the surface conductance up to one order of magnitude when compared to bare metal surfaces. Moreover, a shift to higher open circuit potential was recorded for the coated substrate, enforcing the effect of the multilayered coating as corrosion protection solution for aluminum surfaces.

List of abbreviation

AFM	atomic force microscopy
ALD	atomic layer deposition
CNT	carbon nanotube
d	doublet (NMR spectroscopy)
δ	chemical shift (NMR spectroscopy)
DCM	dichloromethane
DLC	diamond like carbon
eq	equivalent
Et ₂ O	diethylether
ESI	electrospray ionization
GNF	graphene nanoflake
GNR	graphene nanoribbon
GQD	graphene quantum dot
HREELS	high resolution electron energy loss spectroscopy
HRMS	high resolution mass spectroscopy
HCl	hydrochloric acid
IPA	isopropyl alcohol
LbL	layer-by-layer
LCC	linear carbon chain
m	multiplet (NMR spectroscopy)
MeOH	methanol
NBS	n-bromosuccinamide
NAHMDS	bis(trimethylsilyl)amide
OPC	open circuit potential
PA-C18	octadecylphosphonic acid
PAH	polycyclic aromatic hydrocarbon
ppm	part per million
PVD	plasma vapour deposition
q	quadruplet (NMR spectroscopy)
QTOF	quadrupole time-of-flight
Ra	Roughness average

r.t.	room temperature
s	singulet (MNR spectroscopy)
SAM	self-assembled monolayer
SEM	scanning electron microscopy
t	triplet (MNR spectroscopy)
TLC	thin-layer chromatography
TMS	tetramethylsilyl group
UV	ultraviolet
WCA	water contact angle
Zr(AcAc) ₄	Zirconium (IV) acetylacetonate

Table of contents

Riassunto	1
Abstract	13
List of abbreviations	15
1 Introduction	19
1.1 Carbon, a Brief Introduction.....	19
1.2 Synthesis of Carbon Nanomaterials.....	22
1.3 Solution-based Templateless Synthesis.....	23
1.3.1 0D Carbon Nanomaterials.....	23
1.3.2 1D Carbon Nanomaterials.....	25
1.4 Template-based Synthesis.....	26
1.5 Self-assembled Monolayers towards 2D Carbon Nanomaterials.....	27
1.5.1 Towards Multilayered Self-assembled Nanostructures.....	30
1.5.2 Layer-by-layer Technique for the Formation of Multilayers.....	31
1.6 Carbon Nanomaterials from Oligoynes.....	33
1.6.1 Oligoyne Synthesis.....	34
1.6.2 Hexayne Self-assembly for Carbon Nanomaterials Preparation.....	36
1.7 Statement of the Problem.....	39
2 Results and discussions	41
2.1 Synthesis of the Hexayne Bolaamphiphile.....	41
2.2 Optical Properties of the Hexayne Bolaamphiphile.....	46
2.3 Self-assembled Monolayer from the Hexayne Bolaamphiphile.....	46
2.4 Formation of the Multilayer Structure by LbL Deposition.....	48
2.5 Carbonization of the Multilayer Structure.....	51
2.6 Effect of Carbonization on multilayer Disorder.....	54
2.7 Structural Analysis of the Multilayer Coating.....	55
2.7.1 Surface Evaluation by AFM.....	55
2.7.2 TEM Analysis of the Multilayer Cross Section.....	57
2.8 Corrosion Tests.....	58
3 Conclusion and Outlooks	61
4 Materials and Methods	63
5 Bibliography	71
6 Appendix	79

1. Introduction

1.1 Carbon, a Brief Introduction

"I could tell an endless number of stories about carbon atom that becomes colors or perfumes in flowers; or other which, from tiny algae to small crustaceans to fish, gradually return to carbon dioxide to the water of the sea, in a perpetual, frightening round-dance of life and death, in which every devourer is immediately devoured, of other which instead attain a semi-eternity in the yellowed pages of some archival document, or the canvas of a famous painter; or those to which feel the privilege of forming part of a grain of pollen and left their fossil imprint in the rocks for our curiosity; or others still that descended to become part of the mysterious shape-messengers of the human seed, and participated in the subtle process of division, duplication; and fusion from which each of us is born."

The passage cited above, written by Primo Levi in *The periodic table*, remarkably summarizes the ubiquity of carbon, which is virtually everywhere in the world around us, representing the sixth most common element in the universe and the 17th in the Earth's crust.^[1] For some kind of "fate", carbon had the privilege to play the most important role on the scene of life. Since then, it continued to show its crucial function in many breakthroughs of mankind's history, from the discovery of fire, passing through the industrial revolution, and up to nowadays, with the development of the organic chemistry and the overabundance of carbon-based synthetic materials. Nowadays, carbon continues to be regarded with interest in the field of nanoscience, with positive relapses in several aspects of materials engineering and nanotechnology.

The secret of carbon's omnipresence in nature resides in its unique properties to form different types of covalent bonds by what is called hybridization of atomic orbitals, a crucial step that enables carbon to form different compounds, with huge variability both in molecular shape, chemical properties, and reactivity.

For a long time, carbon was conventionally supposed to be mainly found in its sp^3 and sp^2 hybridized states, respectively described by four and three hybridized orbitals. A bulk carbon allotrope with sp^3 hybridization is diamond. The tetrahedral geometry that carbon assumes in

this material is in first place responsible for its transparency, high hardness, high energy band gap and electrical insulation, besides being characterized by the highest thermal conductivity among all the other classes of materials.

Graphite, the bulk carbon allotrope with an sp^2 hybridization, is the most stable carbon material under standard conditions. Here, carbon atoms have a trigonal arrangement with three sp^2 orbitals disposed in plane at 120° each, with the unmodified p orbital placed perpendicularly. This electronic configuration allows the formation of 2D carbon sheets which tends to form stacked layers due to weak Wan der Waals interactions along the layer normal direction. This structural organization is responsible for the low hardness and the optimal electrical conductivity that graphite shows.^[2]

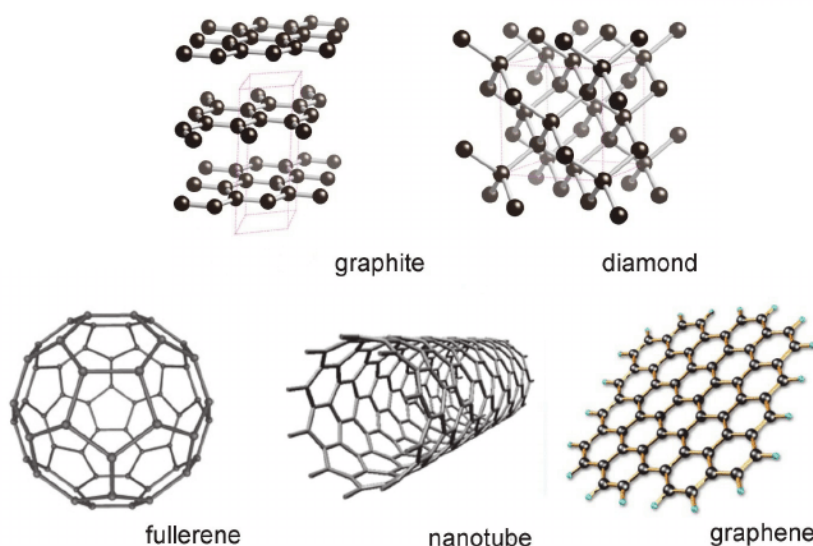


Fig. 1: Fullerenes, carbon nanotubes and graphene are examples of carbon nanoallotropes.

The development of analysis techniques able to detect and characterize matter at the nanometric level has brought the discoveries of other carbon allotropes, which are represented, together with the “canonical” ones, in **Fig. 1**. Curl, Kroto, Smiley and coworkers inaugurated the “carbon era” by isolating and characterizing fullerenes in 1985.^[3] After that, the pace in carbon nanomaterials research speeded up, with the discovery of multiwalled carbon nanotubes by Iijima and coworkers in 1991, obtained as side product of a carbon arc discharge.^[4] Only two years later, Iijima (and, independently, Bethune at IBM) observed buckytubes, that is, single walled carbon nanotubes.^{[5][6]} Graphene, while first observed in 1962 by Bohem et al.^[7], was the last nanoallotrope to be fully characterized, by the work of Geim and Novoselov^[8], which isolated it by mechanical exfoliation method.

It is worth noting that both groups behind the discovery of fullerenes and graphene received a Nobel prize, demonstrating the high importance of the scientific community toward the potential that carbon could play in industrial and technological applications. The physical properties of these nanoallotropes are in fact deeply different from the most known bulk carbon materials: fullerenes can enter superconductivity state upon doping,^[9] while carbon nanotubes and graphene show unique electronic and mechanical properties.

Graphene is a transparent, zero-band gap material with excellent barrier properties, while carbon nanotubes show tunable electronic properties according to their structure and diameter. Moreover, both graphene and carbon nanotubes exhibit outstanding mechanical properties, with experimental studies reporting Young's modulus as high as 950 GPa for nanotubes ^[10] (about five times higher than steel) and 0.5 TPa for a self-standing graphene film.^[11]

Carbyne, also referred to as linear carbon chain (LCC), is the hypothetical carbon allotrope entirely formed from carbon atoms in *sp* hybridization, whose very existence has been argued for a long time.^[12] Traces of carbyne have been found in meteorites,^[13] and spectroscopic traces of it were traced back in space as fundamental constituents of the interstellar medium,^[14] but all the attempts undertaken to synthesize it at laboratory scale have failed. Theoretically, due to its high reactivity and its tendency to react into a graphitic-like compounds, carbyne is highly unstable and explosive. In 2016, an international team of researchers lead by Dr. Pichler took a step forward in the quest for carbyne synthesis, establishing the formation of LCC by encapsulating in a double walled carbon nanotube up to 6000 *sp*-hybridized carbon atoms, as represented in **Fig. 2**.^[15] In 2020, thanks to the work of Kastner et al.,^[16] by studying the characteristic Raman signal shift under increasing hydrostatic pressure, the Young's modulus of the encapsulated LCC has been estimated. With 20 TPa, encapsulated LCCs were claimed to be way stiffer than carbon nanotubes or graphene, which the authors proposed to have potential uses in nanotechnology and nanodevices.

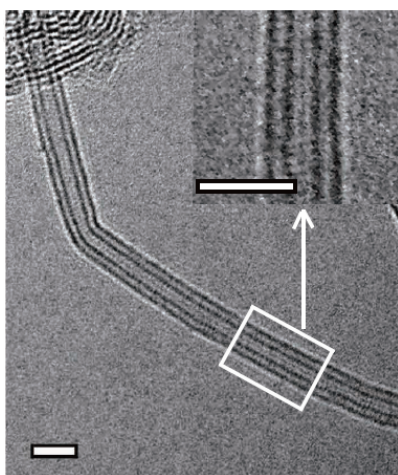


Fig 2: TEM analysis of a LCC inside a double walled nanotube.
Image reproduced with permission from Springer Nature [15].

1.2 Synthesis of Carbon Nanomaterials

Each class of carbon nanoallotropes, from fullerenes to the newly synthesized LCC structure, requires specific synthesis paths to be followed, but all of them usually require harsh conditions (high pressure, high temperatures and energy), especially for top-down approaches, which involve the breaking down of the bulk material into nanosized structures.

These procedures usually impede a precise structural control over the final morphology. Techniques such as arc-discharge^[17] or laser ablation^[18], mainly used to produce 0D and 1D nanostructures, usually introduce broad size distributions and defects, besides requiring high quantity of pure bulk carbon as starting material.

Bottom-up approaches, on the other side, represent an alternative designed to obtain carbon-based nanomaterials from atoms or molecular precursors. These techniques, which are based on chemical deposition techniques^[19] in the case of graphene and carbon nanotubes synthesis, allow for a good control over the nanomaterial size and properties. Unfortunately, the low scalability and the reduced yield severely limits their use mainly to specific research-based applications.

Chemical synthesis approaches represent another possibility to produce carbon-based nanomaterials from reactive molecular precursors. These methods, compared to the previous bottom-up approaches, do not require high temperatures or energetic deposition methods, but they are usually carried out using organic chemistry in a liquid environment, in which the precursors are soluble and free to react. The enhanced control over the synthetic parameters

permits the formation of pure nanomaterials. Moreover, high variability on nanomaterial architecture and functionalization can be achieved by tailoring the molecular precursors. This method is suitable for lab-scale production only, since it shows severe limitations to be scaled up to industrial levels, mainly for the high costs and the environmental issues related to the use of toxic compounds and solvents.

The following subchapters will be devoted to the formation of carbon nanomaterials from reactive precursor in solution-based environments, through self-assembly approaches.

1.3 Solution-based Templateless Synthesis

1.3.1 0D Carbon Nanomaterials

0D nanomaterials are characterized by finite length, usually under 100 nm, in all three dimensions. Apart from buckyballs, the domain of 0D carbon nanomaterials includes graphene nanoflakes (GNFs), that is, graphene fragments with lateral dimensions of up to about 10 nm. Since their structure is composed of few condensed benzene rings, these molecules belong to the family of polycyclic aromatic carbon (PAHs). The limited size of these nanomaterials, compared to graphene, introduces interesting electronic properties. The discretization of the atomic orbitals of the system, in fact, induces the formation of an electronic band gap dependent on the number of aromatic rings and their edge configurations.

^[20] A precise control over the synthesis of GNFs would allow the formation of well-defined semiconductor nanomaterials, with interesting relapses as conductive ink ^[21] or for molecular sensing applications.^[22] Solution-based approaches, thanks to their good control over the nanomaterial shape, represent a useful method for their precise synthesis. GNFs can be straightforwardly synthesized from cyclodehydrogenation of PAHs. For example, Müllen et al.^[23] developed a synthetic approach which makes use of phenylene dendrimers, obtained by Diels-Alder reaction between phenylacetylene and tetraphenylcyclopentadienone, to produce large graphene flakes by cyclodehydrogenation, up to 222 carbon atoms, as represented in **Fig. 3**.^[24]

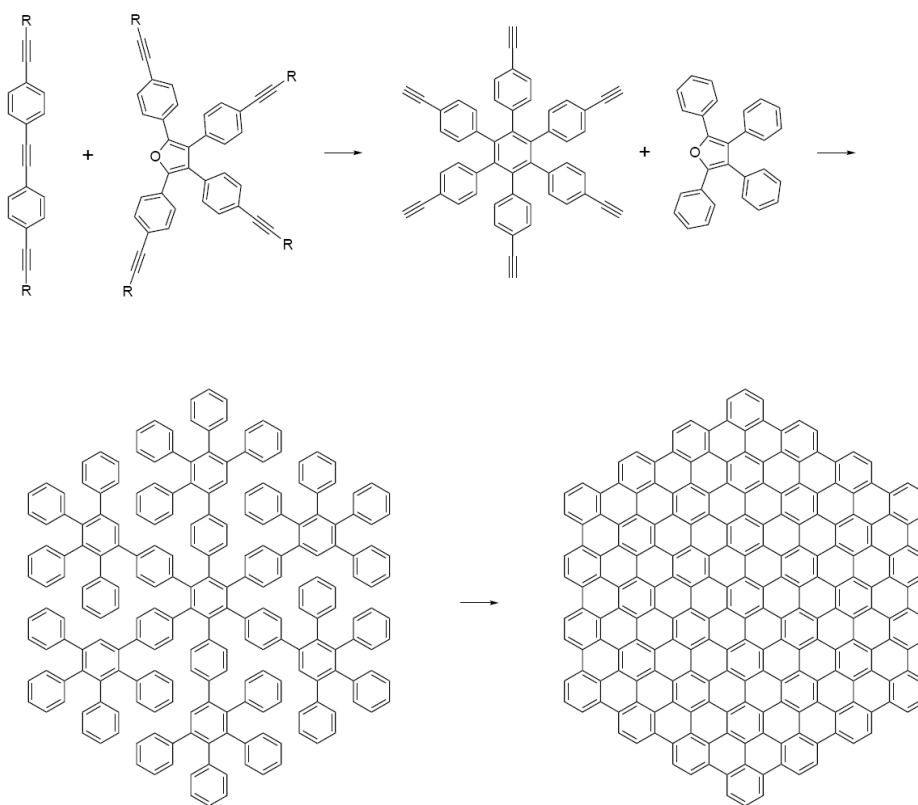


Fig. 3: Synthesis of large graphene flakes by cyclodehydrogenation from phenylene dendrimers *via* Diels-Alder reaction.

By templateless synthesis, it is also possible to extend the size of graphene nanoflakes to larger aggregates, which are technically referred to as graphene quantum dots (GQDs). With lateral dimension usually in the range between 10 and 100 nm, these 0D nanomaterials exhibit strong photoluminescence. For this reason, they may have a great potential in the fields of electronics, optics and biomedical applications.^[25] GQDs can be synthesized from hexabenzocoronene, after previous self-assembly in silica template, followed by pyrolysis and exfoliation.^[26] As shown by Park et al.^[27], GQDs can be obtained by a full solution based approach, by using a monosaccharide as precursor. Another approach can be represented by microwaves assisted one pot method, as reported by Fresco-Cala et al.^[28]. By introducing urea and glucose in a solution of phosphonic acid, the group succeeded in obtaining photoluminescent GQDs, by exposing the mixture to microwave radiation.

Overall, solution-based approaches for the synthesis of 0D carbon nanomaterials have revealed to be an effective method for the production of GNFs and GQDs, with good control over the nanomaterial shape and structure.

1.3.2 1D Carbon Nanomaterials

1D carbon nanomaterials are characterized by a spatially extended structure along one dimension, as in graphene nanoribbons (GNRs) and carbon nanotubes (CNTs).

Alongside GNFs and GQDs, CNTs show interesting tunable electronic properties, with an electronic band gap inversely dependent on the structure diameter or with the development of a metallic behaviour when specific chirality rules are respected ^[29]. Solution-phase organic synthesis, thanks to its strict determination of molecular structure, could provide good morphological control over CNTs. However, the poor solubility of the intermediates would prevent such an approach to be used for nanotube growth, limiting the size of the obtained nanomaterials. The combination of organic chemical synthesis and CVD approach represents a possible solution for the synthesis of carbon nanomaterials, by seeding with a well-defined cyclic organic precursor to control the diameter and the size of the growing structure. As reported by Scott et al. ^[30], hemispherical polyarenes can be exerted as seeds for the growth of CNTs by consecutive annulation reactions from pentabenzocorannulene, despite the low yield of the reaction. An interesting approach for the synthesis of tunable single-walled CNTs was proposed by Itami et al. ^[31]. By using cycloparaphenylenes as starting seed onto copper surface, the carbon nanotube was grown with CVD method on top of the organic ring, which fixed the diameter and the chirality of the carbon nanomaterial obtained.

GNRs can be easily obtained by templateless approaches, with all the benefits that organic synthesis enables for better morphological control. GNRs show morphology-dependent electronic properties. Indeed, the edge configuration can be zigzag or armchair, which influences the electronic behaviour from metallic to semiconducting, respectively with a band gap inversely dependent on the ribbon width. ^[32]

The solution-based synthesis of GNRs can be achieved by step-growth polymerization by Diels-Alder reactions ^[33] or by alkyne benzannulations followed by cyclization reaction. ^[34]

These methods are, however, characterized by low control over the polymerization step due to the nature of step-growth polymerization, which negatively impacts the electronic properties of the nanostructures.

1.4 Template-based Synthesis

Solution-based templateless approaches, which already showed their limitation for 1D carbon nanomaterials, are even harder to adapt to the synthesis of 2D carbon nanomaterials, due to the intrinsic difficulty to maintain the reactions in a confined plane. Apart from the established dispersion problems, structural defects in the nanomaterial shape could occur during the synthesis, leading to curvature and distortion phenomena in the growing 2D nanomaterial.^[35]

To partially solve the problem, the introduction of a template can play a positive role in confining the precursor while allowing its planar self-assembly. By following this approach, Cai et al.^[36] synthesized tailored GNRs by exploiting the surface-assisted coupling of monomers to form linear polyphenylenes, which were later subjected to a cyclodehydrogenation reaction to give GNRs. Thanks to the surface-assisted synthesis, the researchers showed that this method enables the formation of well-defined GNRs, characterized by lower variability in terms of shape and morphology with respect to the ones from templateless methods.

Surfaces have also been used in the formation of graphdiyne, a 2D carbon nanoallotrope characterized by both sp^2 and sp hybridization. In particular, Li et al.^[37] have reported the formation of a graphdiyne monolayer on copper surfaces by immersion in a solution of hexaethylnylbenzene at 60°C and subsequent surface-catalyzed dehydrogenation.

The formation of graphene from template-based approaches, on the other side, has been affected by several difficulties and limitations. Lopes et al.^[38] successfully synthesized graphene at the interface between a oily, benzene-containing phase and a liquid phase used to provide the $FeCl_3$ catalyst. Large graphene sheets of up to 10 μm^2 , were obtained and characterized by Raman spectroscopy, as well as with different atomic-resolution microscopies, which highlighted their low structural quality. Moreover, a significant amount of catalyst was found trapped in the carbon nanomaterial, especially various iron oxide species, which drastically influence its electronic behaviour.

At present, no synthetic solution-based approach has been reported so far to coat a surface with a graphene monolayer in the scientific community, mainly due to the intrinsic difficulty in maintaining a continuous, defect free coating over a large surface, rather than several drawbacks related to the precursor compounds and their organization. As these investigated precursors are generally freely distributed in one of the phases, they do not assemble at interfaces, which leads to a lack of control over the properties of the nanomaterials.

1.5 Self-assembled Monolayer toward 2D Carbon Nanomaterials

As highlighted in the previous chapter, the catalytic character of surfaces can play an active role in the formation of carbon nanomaterials from reactive precursors but, at the same time, low coverage, morphology and thickness defects do not allow for the formation of extended 2D carbon nanomaterials. Ideally, the best approach in the formation of 2D nanomaterials would imply the direct assembly of the organic precursor onto the substrate and its further conversion into a carbon-rich nanomaterial. From this point of view, self-assembled monolayers (SAMs) could represent an interesting solution.

SAMs are formed from surfactants that should have a polar head and a hydrophobic tail, which can be decorated with further chemical groups. When in presence of a solid-liquid interface, such amphiphiles tend to place the polar head group close to the surface, forming a well-packed self-assembled monolayer (SAM), as represented in **Fig. 4**. The process is fostered by the physico-chemical interaction between the molecule's polar head and the substrate, as well as secondary hydrophobic forces among the hydrophobic tails. In some cases, the interaction between the polar head group of the amphiphilic molecule and the surface results in the formation of a covalent bond with the surface. Some useful combinations of anchor groups and surfaces include thiols on gold, or phosphonic acids and carboxylic acids on metal oxide surfaces.^[39] Eventually, the tail group provides some functionality to the monolayer and determines the interaction of the assembly with the environment, as well as its surface energy.

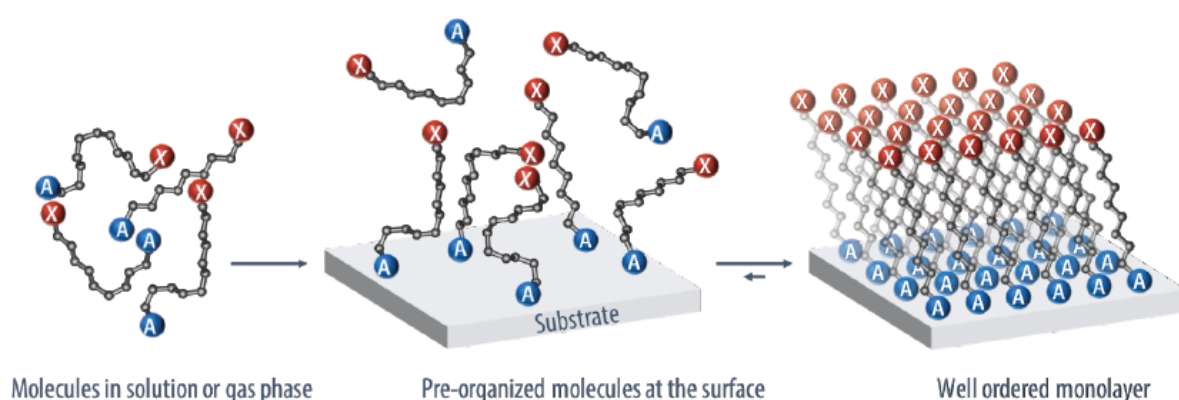


Fig. 4: Formation of a SAM at the solid interface from amphiphiles.
Image reproduced from [40].

One of the first reported examples of a SAM was studied by Nuzzo and Allara,^[41] who observed the formation of a densely packed organic layer onto gold surfaces when immersed in a solution of alkane disulphides. They found that the precursor molecule can tightly bind to the surface, covering all attachment sites, with the alkyl chain pointing away from the surface. In such a way the molecules form a dense, well-packed monolayer.

For SAMs, the coverage process is a two-step self-assembly process, consisting in an initial fast adsorption step and in a second, slower step of molecular organization.^[42] After few seconds from immersion, molecules start to approach and bind to the surface in a disordered fashion. Over time, the surface adsorption kinetics slow down, since only low-energy sites remain exposed on the surface. At the same time, the interaction between the hydrophobic tails starts to develop, leading the system towards a high degree of order.^[42] Differently from surface-catalysed nanomaterials, the organic monolayer that forms at the surface is not mechanically stable and retains a fluid-like behaviour in most cases.

Carbon nanomaterials can be produced from SAMs. For example, Shin et al.^[43] induced the formation of a SAM on silicon oxide substrates from different alkyl amphiphiles. The self-assembled structure was then protected by a nickel layer and treated by annealing at 900°C to allow the graphitization and the formation of different, stacked graphene layers. It is interesting that different graphene structures can be obtained according to the surfactant used to induce SAM formation. For instance, an octyl-substituted SAM leads to the formation of two to three graphene layers, while the octadecyl substituted SAM to an average of four to five graphene layers. In all cases, a defect-rich, heterogeneous graphene nanostructure is obtained.

Turchanin and Götzhäuser,^[44] by taking advantage of the self-assembly of thiol-based aromatic molecules, developed carbon nanomembranes from SAMs. More specifically, the group synthesized end-functionalized thiol polyarenes that undergo self-assembly on gold surfaces. The most interesting aspect developed by the researcher lays on the ability of polyarenes to crosslink when irradiated by an electron beam, which causes the radical cleavage of the phenyl hydrogen atoms. The consequent radical generation allows crosslinking and the formation of a continuous, carbon monolayer, characterized by high mechanical stability.

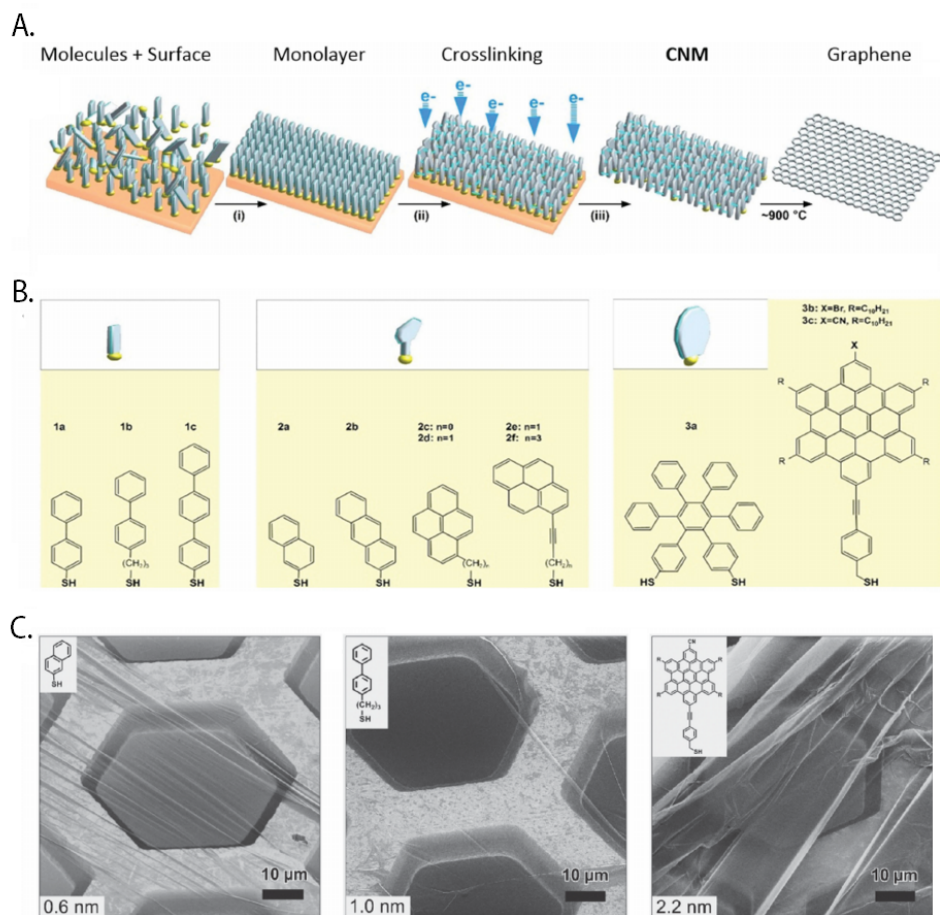


Fig. 5: (a) Schematic representation of the carbon nanomembrane formation of a graphitic monolayer from the self-assembly of thiol-terminated polyarenes after electron beam irradiation and annealing. The high variability of the hydrocarbon segment allow the formation of several precursors (b), which deeply impact the nanocoating nature in term of thickness and porosity (c). Image reproduced with permission from John Wiley and Sons [44].

By playing on the chemistry of the precursor, such as the length and geometry of the polyaromatic molecule, the group succeeded in tuning the carbon film thickness and its porosity, as represented in **Fig. 5**. Annealing at 1000°C under ultra-high vacuum condition permit the transformation of the amorphous carbon coating into nanocrystalline graphene sheets, if desired.

The carbon nanomembranes displayed strong mechanical stability even before annealing, since they were able to withstand the application of pressures, of up to few bar without breaking.^[45]

Overall, the findings reported here demonstrate the possibility to form carbon nanomembranes from SAMs. Still, a large energetic input is required to promote the transformation from the organic SAM onto a graphenic, mechanically stable carbon nanostructure. Under these conditions, every functional group that could have been introduced in the SAM by tuning the amphiphile tail group of the amphiphile, is inevitably lost.

1. 5.1 Towards Multilayered Self-assembled Nanostructure

Among the families of precursors that undergo SAM formation, bolaamphiphiles represent an interesting class of surfactants. Characterized by two polar head groups in α and ω positions as illustrated in **Fig. 6**, bolaamphiphiles are the basis of many self-assembled materials, especially in the field of ion transport, optoelectronics, drug and gene delivery.^[46]

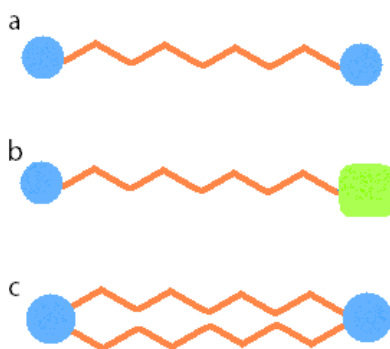


Fig. 6: Different classes of bolaamphiphiles, (a) symmetric , (b) unsymmetric and (c) double-chained. Orange colouring indicates the hydrophobic segment, while blue and green colour stands for different, hydrophilic groups.

Differently from amphiphiles, whose nature and self-assembly have been extensively studied,^[47] the self-assembly of bola-surfactants in liquid systems or at the liquid/solid, liquid/air interface cannot be straightforwardly determined. In general, when confined to an interface, bolaamphiphiles can assume two different configurations, depending on the rigidity of the central hydrophobic block.^[48] Molecules with a rigid backbone or a very short spacer tend to orient perpendicularly to the interface while, in the case of a longer or more flexible spacer, bolaamphiphiles bind with both terminal groups to the substrate, as shown in **Fig. 7**.

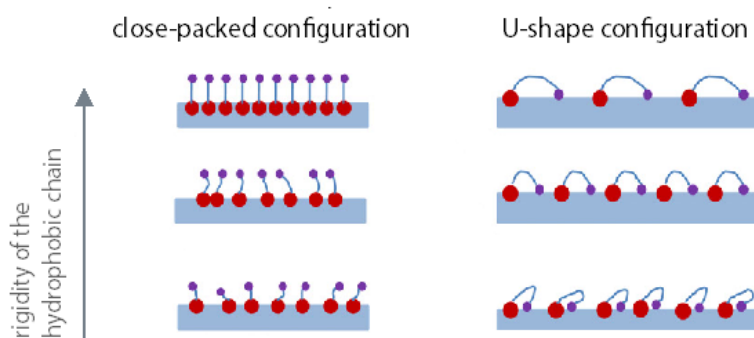


Fig. 7: Self-assembled monolayer from bolaamphiphile, with close-packed and U-shape configuration of the central backbone. Image reproduced with permission from John Wiley and Sons [49].

1.5.1 Layer-by-layer Technique for the Formation of Multilayers

The tendency of bolaamphiphiles to form a SAM can be further exploited thanks to the presence of a second polar terminal group, which introduces a diffuse charge on the SAM-terminated surface. Acidic groups, for instance, can bear a negative charge when dissociated, while amino groups can become positively charged. The layer-by-layer (LbL) deposition technique provides a straightforward method to form multilayered structures on a surface, by taking advantage of the surface charge to deposit countercharged material.

This technique, introduced in the 1991,^[50] plays with the residual charge that remains after the surface adsorption of a chemical species, usually by immersion or by other liquid deposition techniques such as spray coating, doctor blade, roll coating. The charged substrate can in fact attract other chemical species characterized by opposite charge. This second absorption reverses the surface charge at the interface, enabling the deposition of the first chemical species and so on.

Of course, the LbL technique is not only limited to the development of electrostatic forces between the precursors, but also hydrophobic interactions, hydrogen and coordinative bonds can be used between precursors to grow multilayered structures.^[51] LbL films, compared to SAMs, offer the possibility to create heterogeneous multilayered architectures, with thickness variability and can be exerted as a tool to introduce several functionalities in the film. For this purpose, it is necessary that the adsorption of the bolaamphiphile on the surface results in the formation of a closely packed monolayer. An eventual U shape-configuration will not allow the formation of a multilayer structure by LbL deposition.

The scientific literature has already investigated the formation of complex architectures from

bolaamphiphiles. In 1988, Mallouk et al.^[52] were the first to show that zirconium (IV) organobisphosphonates can form particularly stable surface multilayers that can be built up by self-assembly. More specifically, the deposition technique was performed by a first covalent attachment to the surface with a phosphonic acid anchoring agent. Subsequently, the functionalized substrates were exposed alternately to an aqueous solution of Zirconium (IV) chloride and 1,10-decane bis(phosphonic acid) to yield the multilayered film. In particular, the zirconium-phosphonate system has demonstrated to be effective in the formation of multilayered assemblies by LbL technique, because both components are of good solubility but form together an insoluble layered structure.^[53] Thanks to the strong ionic coordination bonds formed between the phosphonic head groups and the zirconium ions, the multilayered structure possesses a high thermal, chemical and mechanical resistance. In particular, the heterogeneous multilayered coating was found to have effective applications as dielectric and corrosion-protective coatings.^[53]

A similar approach was followed by Kang et al.^[54], who produced zirconium- and hafnium-alkyl bisphosphonate multilayer films by cyclic immersion in aqueous solutions. In particular, they proved the formation of a multilayered structure by X-ray reflectivity, while an increase in structural disorder was observed by AFM at higher layer numbers.

By taking inspiration from the work of Turchanin and Götzhäuser, Hamoudi et al.^[55] developed an interesting strategy to obtain a carbon-metal intercalated multilayered structure. A bipyridine-based bolaamphiphile, endcapped by two thiol moieties, was deposited by immersion onto a gold surface to form a SAM. Consequent immersion in a nickel-rich solution allows the metallic cations to complex the thiol and pyridine moieties, forming a rich, capping metallic stratum. This positively charged monolayer can act as substrate for the formation of a second layer by immersion in the bipyridine solution, as shown in **Fig. 8**. Eventually, the organic coating was crosslinked by electron beam irradiation, leading to a self-standing carbon nanomembrane. The group also showed that, after exposing to high-temperature annealing, the coating maintains its layered structure while still displaying a graphitic carbon morphology.

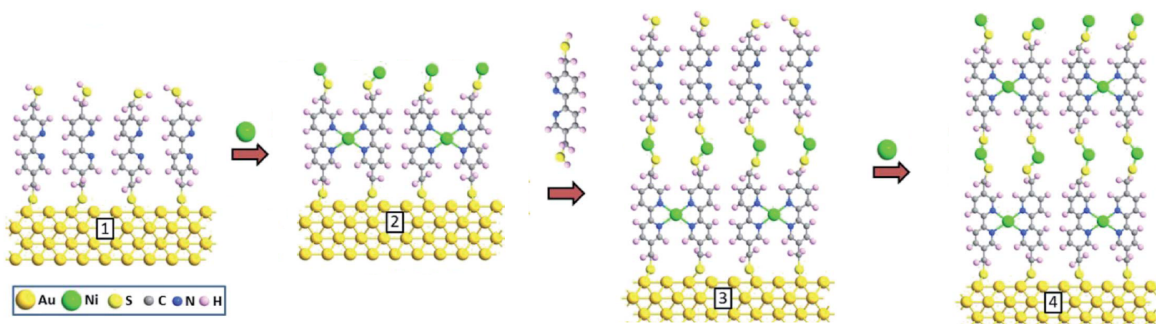


Fig. 8: LbL deposition technique applied to the formation of nickel-bipyridine multilayer. Image reproduced from [55].

1.6 Carbon Nanomaterials from Oligoynes

As previously shown, organic precursors adjoined with a surface-anchor group, can undergo SAM formation. This closely packed, organic monolayer can be eventually transformed into a self-standing, carbon nanomembrane by electron beam irradiation or when exposed to high temperature annealing. However, the conditions under which this transformation occurs are often incompatible with the presence of organic functionalization in the precursor molecules. Furthermore, the substrates used to induce the formation of the multilayer could not bear the high-energy electron irradiation or annealing used to transform the organic coating into a carbon nanomembrane. In order to prevent the loss of functional groups in the carbon coating and substrate damages, milder conditions need to be found.

One way to circumnavigate the problem is using metastable carbon-rich molecules instead of stable polycyclic aromatic compounds. In the last decade, oligoynes precursors have been regarded as interesting precursors for the formation of carbon nanomaterials.^[56] Previous studies performed by Hlavatý et al.^[57] showed that hexatriynes can spontaneously polymerize to form multi-walled carbon nanotubes up to 200 nm in length. Similar research has been carried out by Ding et al., who synthesized carbon nanospheres from tetraynes.^[58] In both cases, an 800°C annealing was still needed to induce complete graphitization of the condensed alkyne systems.

Instead of high temperatures, a different approach for the carbonization based on UV irradiation of oligoynes can be envisaged.^[59] As demonstrated by Enklemann,^[60] diacetylenes can be turned into polydiacetylenes by UV exposure and under specific geometric restrictions. To allow this topochemical polymerization to occur, a defined intermolecular distance of

about 4.9 Å needs to be established between the diacetylene monomers. Moreover, the diacetylene units should show a 45° tilt angle with respect to the packing axis, in order to bring the appropriate carbon atoms into a reactive distance of about 3.5 Å, as represented in **Fig. 9**.

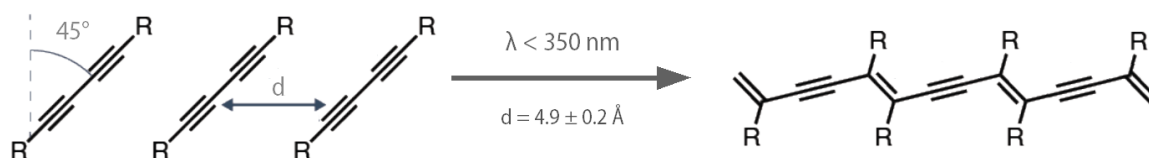


Fig. 9: Topochemical polymerization of diacetylenes by UV irradiation. The geometrical conditions are highlighted in grey.

According to Tykwinski et al.,^[59] the chemical stability of oligoynes tends to reduce drastically when more acetylenic units are added to the *sp* chain. This destabilization contributes to lowering the energetic requirements for topochemical polymerization and/or carbonization to occur. On the other side, their inherent instability represents one of the hardest difficulties to overcome during the synthesis of higher oligoynes.

1.6.1 Oligoyne Synthesis

In comparison to the common presence of *sp*² and *sp*³ hybridized carbons in natural compounds, *sp* hybridization is less common, although some organisms indeed produce polyynes, that is, organic molecules characterized by alternating single and triple bonds. These acetylenic-containing compounds can be isolated from plants, common garden vegetables, or bacteria.^[61] Spanning from pigments, toxins and flavoring, natural occurring polyynes can even be used as pharmaceuticals, such as antifungal ^[62] and antiretroviral agents.
[63]

As early as 1869, Glaser described the first acetylene coupling by observing the oxidative dimerization of copper (I) phenylacetylide when exposed to a basic environment.^[64] In 1959, Eglinton and Galbraith^[65] developed a synthetic path towards symmetric oligoynes, through an oxidative coupling of terminal alkynes, *via* the introduction of a stoichiometric amount of a copper salt (II) in pyridine. In 1962, Hay introduced a modified version of the Glaser coupling, by the use of TMEDA complex of copper (I) chloride.^[66] Both these methods are known as homocoupling methods as they allow the formation of symmetric oligoynes only.

By contrast, the mechanism introduced by Cadiot and Chodkiewick in 1969^[67] enables the formation of unsymmetric alkynes. The reaction involves the preparation of a halogenated acetylene, which is further coupled with a terminal alkyne by means of a copper (I) catalyst. The procedure has the disadvantage of often low conversions in the case of higher oligoynes. ^[59] An interesting approach in the synthesis of unsymmetric oligoynes was introduced by Negishi et al.^[68] Thanks to the palladium catalyst in the reaction media, the selectivity problems, which characterize the previous Cadiot-Chodkiewick coupling, are overcome, since it acts as the active center for the further cross-coupling reaction of a haloacetylene with an *in-situ* generated zinc acetylide. A schematic representation of the main alkyne coupling reactions is shown in **Fig. 10**.

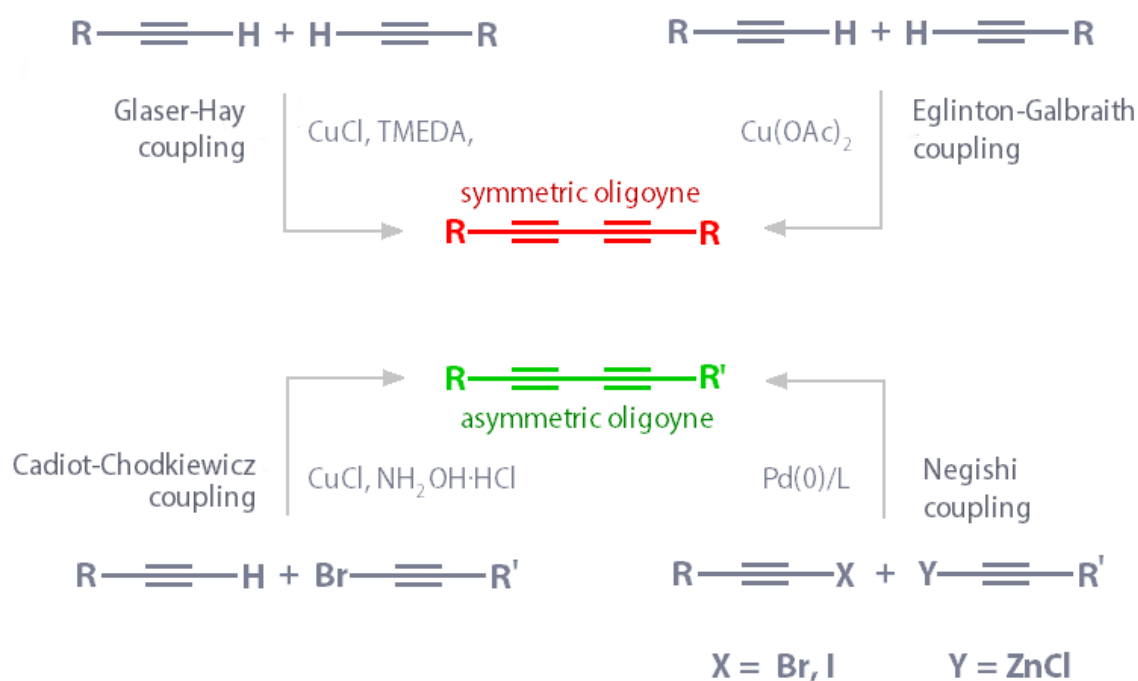


Fig. 10: Some approaches in the synthesis of symmetric and unsymmetric oligoynes.

As already highlighted, the synthesis of oligoynes tends to be more and more demanding with increasing length of the *sp*-hybridized carbon segment, due to the increasing reactivity of such segments, especially when *sp*-carbon atoms are closer than the reactive distance (3.4 Å) in the solid state.^[60] Crosslinking can thus easily occur during the synthesis, leading to the formation of a carbon residue that cannot be recovered. Moreover, the high heat generated in the process represents a safety hazard, due to the risk of explosion which characterizes higher oligoynes. The approach used for the formation of longer oligoynes is the introduction of terminal protective groups, which sterically hinder the reactive carbon chain to crosslink.^[69] This

solution works particularly well up to 8–10 acetylenic units.^[59] Further elongation of the *sp* chain could be made possible with the introduction of a rotaxane cage around the reactive carbon chain, which prevents its topochemical polymerization and bending. An interesting example has been reported by Schrettl et al.,^[70] who took advantage of two threaded α -cyclodextrin hosts which encapsulated the oligoynes chain. This host-guest complex was found to shield and stabilize the reactive segment against photochemical degradation or cross-linking.

1.6.2 Hexayne Self-assembly for Carbon Nanomaterials Preparation

Acetylenic coupling reactions enable the preparation of oligoynes surfactants. Specifically, the Frauenrath group developed a synthetic route which allows the formation of unsymmetric and symmetric hexaynes, with a large variability of terminal groups ^[71]. Symmetric hexaynes have been obtained by straightforward application of Eglinton-Galbraith homocoupling conditions, while the synthesis of unsymmetric molecules was performed by following the same protocol but with the addition of a sacrificial triyne, which contributed to raise the reaction yield by a factor of nine compared to a similar synthesis performed under Negishi coupling pathway. Phosphonic acid, carboxylic acid, amine and thiol functions have been successfully introduced as terminal group of a central hexayne chain, as represented in **Fig. 11**.

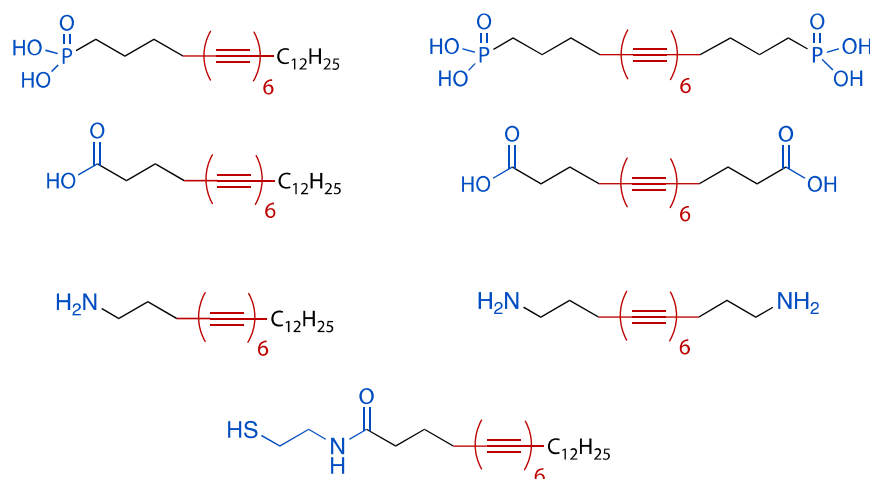


Fig. 11: Different hexayne containing amphiphiles and symmetric hexayne bolaamphiphiles developed by the Frauenrath group. Image reproduced with permission from John Wiley and Sons [69].

The amphiphilic nature of the substituted hexaynes allow them to undergo monolayer formation, especially at the solid-liquid interface. The reactive *sp*-hybridized backbones, when closely packed in a monolayer, can be crosslinked by UV irradiation, resulting in a continuous 2D carbon nanomaterial.

As shown by Bomal et al.^[71], the hexayne amphiphiles can undergo self-assembly at the solid/liquid interface. In particular, the bisphosphonic acid and the dicarboxylic acid showed not complete monolayer formation, probably due to the formation of U-shape structures at the interface. The same group exploited methyl octacos-5,7,9,11,13,13-hexynoate to form carbon nanosheets at the liquid/air interface using a Langmuir trough apparatus, as represented in **Fig. 12**.^[72] The formation of the monolayer at the air-water interface was then followed by a UV irradiation step to induce the carbonization of the structure, and the conversion was followed by infrared absorption reflection (IRRA) spectroscopy, which revealed the disappearance of the hexayne peak at 2100 cm^{-1} . Furthermore, a reduction in thickness after carbonization has been observed, as well as a lateral expansion of the film. This might indicate the formation of graphenic tiles from polyacetylenic units, which are characterized by a larger surface area compared to the cross-sectional area of the hexayne precursor.

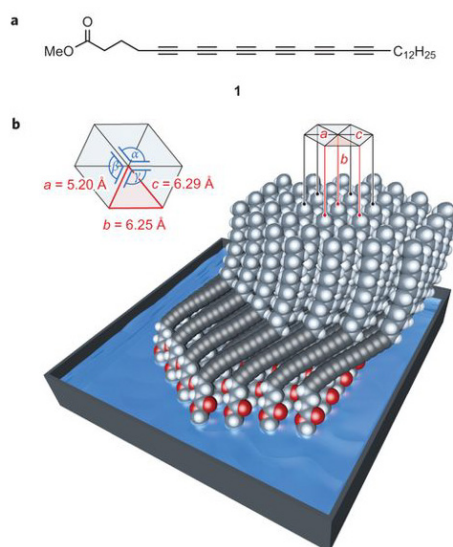


Fig. 12: **a)** Representation of the amphiphilic molecules used in the formation of the carbon nanolayer. **b)** Structural model of the self-assembly of the molecules. Image reproduced with permission from Springer Nature [72].

The concept of the UV-induced carbonization of hexayne was further extended to the solid/liquid interface by Yeo et al.^[73], to obtain carbon nanocoating on alumina surface. The SAM was obtained by immersion of plasma activated alumina coated wafer substrates in a solution of the precursor in isopropanol. After performing IRRA spectroscopy and water contact angle (WCA) analysis, it was shown that a dense and continuous monolayer structure was obtained, however, characterized by structural disorder in the terminal alkyl sublayer. As **Fig. 13** shows, the carbonization of the SAM induced the formation of a carbon nanocoating on top of the surface. Moreover, the carbon nanocoating corrosion protection properties were evaluated, and showed an increase in polarization resistance.

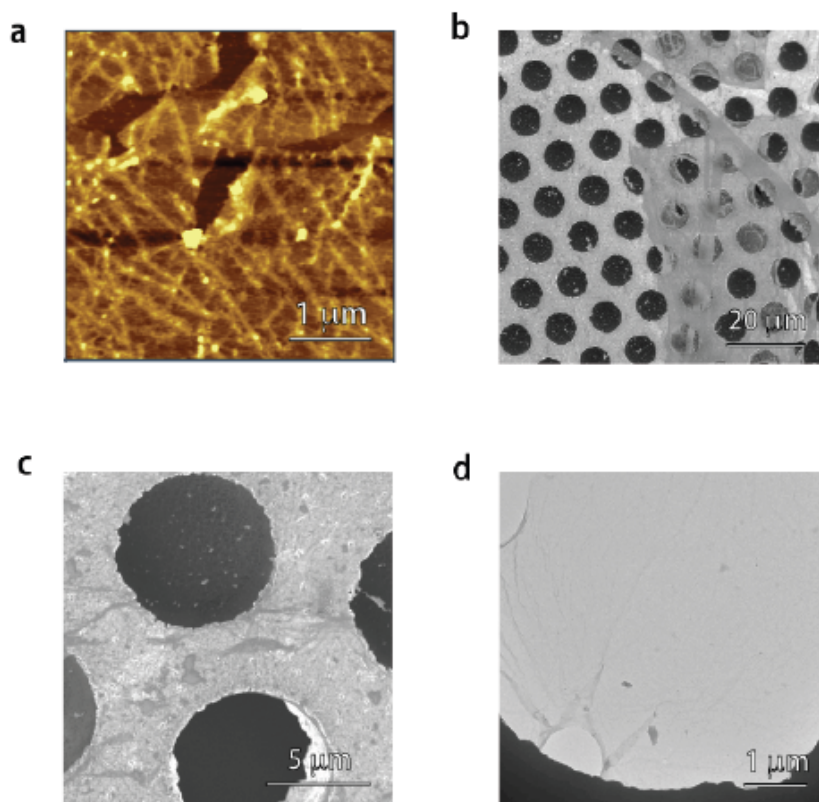


Fig. 13: (a) atomic force microscopies of the transferred carbon monolayer. SEM results are shown on fig. b and c, while transmission electron micrograph is represented in d. Images reprinted from [73].

1.8. Statement of the Problem

Higher oligoynes are interesting molecular precursors for the formation of carbon nanomaterials^[57,58] thanks to their versatile chemistry and the high reactivity of the *sp*-hybridized carbon segment, which can crosslink once exposed to mild-UV radiation at room temperature. The hexaynes can be functionalized with surface-active head groups that allow the precursor to form a SAM,^[73] which can eventually be transformed into a continuous carbon nanocoating upon UV-irradiation and used for corrosion protection.

The aim of the present master thesis is to extend the hexayne monolayer approach to a more complex architecture, by creating a self-assembled multilayer structure by applying an LbL approach to a bisphosphonic acid hexayne / zirconium (IV) system, able to undergo carbonization upon UV light exposure, thus leading to a multilayer carbon nanostructure.

The experimental work will aim to solve the following research questions.

Can we form a self-assembled multilayer structure that include a a hexayne surfactant?

For this purpose, we will synthesize a specific hexayne that is bolaamphiphilic and investigate its self-assembly at the surface. Once the optimal self-assembly are found we will prepare the multilayers structure and demonstrate the incremental increase in thickness that results from it.

Can we obtain a carbon coating from the multilayers by UV irradiation?

We will investigate the conversion of the organic multilayers into a carbonaceous structure. Then, we will determine the nature of the carbon nanomaterial by Raman spectroscopy and investigate whether the carbonization step induces defects or delamination.

Does the organometallic coating contribute to corrosion protection?

We will investigate whether the presence of the carbonaceous multilayer coating induces an increase in the surface resistance and a decrease in the corrosion current density when compared to bare aluminium by a potentiodynamic polarization analysis.

2. Results and Discussion

2.1 Synthesis of the Hexayne Bolaamphiphile

The first step in the preparation of the multilayer coating is the synthesis of the carbon precursor, a hexayne bolaamphiphile represented in **Fig. 14**. This molecule shows self-assembly capabilities towards surfaces, thanks to the terminal phosphonic acid groups. Such a bolaamphiphile could behave both as a primer, since it should form an ordered monolayer on a metal oxide substrate, as well as a bridging element between consecutive cationic layers. The presence of ethylene spacers increases the tendency of the molecule to form an ordered monolayer on the surface, since it would decrease the gyration angle between the terminal phosphonic head groups and the central hexayne backbone, thus limiting the occurrence of U-shape configurations. Moreover, the presence of the hexayne moiety allows the stratified structure to carbonize when exposed to mild UV irradiation. It should hence be possible, with such a precursor, to form carbon rich layers alternated by a diffuse layer of cations, attracted by ionic bonds to the phosphonic acid terminating head groups.



Fig. 14: structure of hexadeca-3,5,7,9,11,13-hexayne-1,16-diylbis(phosphonic acid), target molecule of the synthetic path.

In order to obtain the target hexayne molecule, we designed a pathway that allows its synthesis in six steps, as represented in **Fig. 15**.

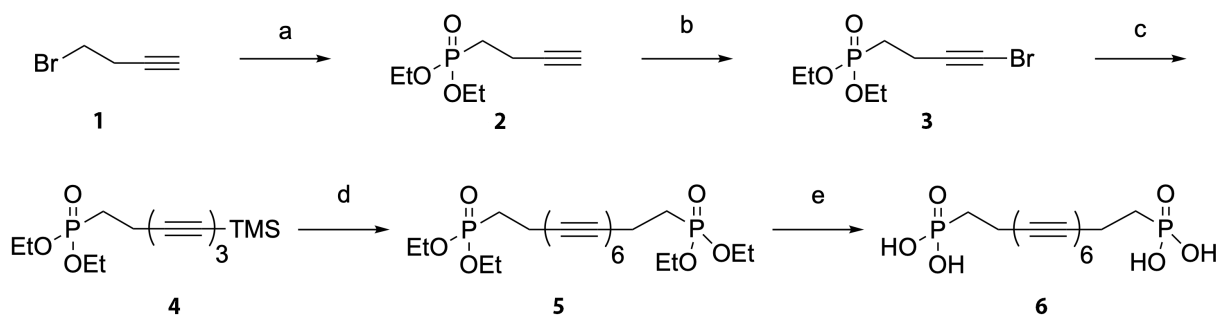


Fig. 15: synthesis of the biposphonic acid hexayne. Reagents, conditions and yield: **[a]** diethyl phosphide, NaHDMS; DCM, r.t., 12h; 35% **[b]** BrNHS, AgNO₃; DCM/MeCN, r.t., 3h; 90% **[c]** MeLi.LiBr, nBuLi, ZnCl₂, Pd(dppf)Cl₂, 1,4-bis(trimethylsilyl)butadiyne; THF/toluene, 0°C, 48h, light shielded; 76% **[d]** CsF, Cu(OAc)₂; DCM/MeOH/2,6 lutidine, r.t., 4h; 76% **[e]** TMS-Br, HCl; DCM, 3h; 19%

As a starting point, 4-bromo-1-butyne was subjected to a Michaelis-Becker reaction^[74] with diethyl phosphite. The reaction was conducted in DCM using sodium bis(trimethylsilyl)amide (NaHMDS) as a base, to deprotonate the diethyl phosphite and promote its substitution of the bromide leaving group of the precursor. After having verified the completion of the reaction, the product was washed and purified by column chromatography using a mixture DCM/MeOH solution (97.5:2.5) as the eluent to give compound **2** in 35% yield. The low yield could be partially attributed to the low molecular weight of the precursor which, conjointly with the presence of the phosphonate head group, could have increased the solubility of the final product in water, used during the washing step. Furthermore, the low molecular weight of the product suggests a low boiling point and a higher tendency toward evaporation during the drying step. The ¹H-NMR spectrum confirms the presence of the diethyl phosphonate group, with the signals at 1.2 ppm and at 3.97 ppm, corresponding to the terminal hydrogen atoms of the -CH₃ and to the adjacent -CH₂- moieties of the protecting ethyl group. The signal at 2.35 ppm corresponds to the hydrogen atoms close to the triple bond, while the remaining hydrogens, the two belonging to the alkyl chain close to the phosphorous as well as the terminal hydrogen of the triple bond, fall in the peak at 1.87 ppm. According to ¹³C-NMR spectroscopy, the presence of the new carbon of the ethyl moieties of the phosphonates can be found at around 16.4 ppm for the terminal -CH₃ and at 61.7 ppm for the -CH₂- close to the oxygen. The presence of the triple bond can be observed at around 82.7 ppm and at 69 ppm, which respectively indicate the carbon next to the triple bond and

the terminal $\equiv\text{CH}$ carbon. The presence of the phosphonate group was confirmed by the ^{31}P -NMR spectrum, which shows a sharp peak at 28.89 ppm.

The following step consisted in the bromination of the terminal alkyne, by the addition of *N*-bromosuccinamide (NBS) in presence of silver nitrate as a catalyst, which resulted in diethyl (4-bromobut-3-yn-1-yl)phosphonate **3** with a yield of 90%. The ^1H -NMR spectrum confirmed the disappearance of the terminal alkyne hydrogen, and the ^{13}C -NMR analysis proves the bromination by the shift of the terminal alkyne signal from 69 ppm to 39 ppm.

Subsequently, the length of the *sp*-hybridized backbone of the molecule was increased through a Negishi coupling procedure.^[71] In more detail, 1,4-bis(trimethylsilyl)butadiyne was selectively cleaved from one of the silyl groups and further lithiated by the addition of $\text{MeLi}\cdot\text{LiBr}$. Then, a transmetalation to form the zinc acetylide was performed by introducing zinc chloride to the mixture. Simultaneously, the suspension of the platinum catalyst $\text{Pd}(\text{dppf})\text{Cl}_2$ in toluene was activated by the introduction of *n*-BuLi. The first solution was introduced in the second flask at the same time as compound **2**. The mixture was allowed to react for two days and, after successful TLC analysis, quenched. The hereby described Negishi coupling gave the desired product **4** in 76% yield, after purification by column chromatography using a mixture of DCM/MeOH (97.5:2.5) as eluent. The formation of the triyne backbone was revealed by the appearance of new peaks in the ^{13}C -NMR spectrum, at 88.6 ppm, 86.7 ppm, 66.8 and 62.4 ppm, respectively, together with the complete disappearance of the brominated carbon peak at 39 ppm.

The formation of the symmetric hexayne **5** was performed by a modified Eglinton-Galbraith homocoupling reaction, inspired by the work of Tykwinsky and coworkers.^[75] Cesium fluoride was used for the *in situ* removal of the TMS end group, while copper (II) acetate was used as the catalyst. After 4h of stirring, the product was washed, dried and purified by column chromatography in DCM/MeOH 95:5. The desired product **5** was obtained as a brown powder in 76% yield. The disappearance of the peaks at 0.01 ppm and 0 ppm, respectively in the ^1H -NMR and in the ^{13}C -NMR spectra proves the successful removal of the TMS protecting group.

One fraction of the protected hexayne was diluted in DCM and introduced in a refrigerated environment at -17°C to slowly evaporate the solvent and prevent spontaneous reaction inside

the crystal.^[76] Fiber-like crystal were obtained and X-ray crystallographic analysis was performed. Despite the low crystal quality obtained (R_1 value almost 20%), a structure was resolved. The crystal lattice, as well as an extended reproduction of the crystal structure, is shown in **Fig. 16**.

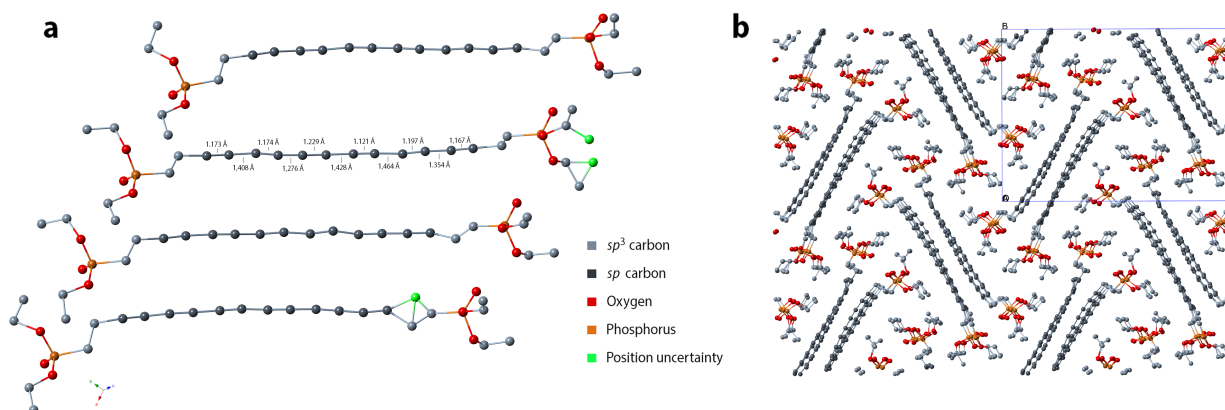


Fig. 16: A solid state molecular cluster of **5** (a), together with its crystal structure (b).

The characteristic double herringbone architecture assumed by the hexayne cores is easily spotted. Atoms in green represent position uncertainty.

The structural disorder that affects the quality of the crystal structure is mainly due to terminal ethyl protecting groups, that sterically hinder the formation of a more compact structure. This effect can be observed in **Fig.16a**. It is also interesting to observe the triple-single bond alternation pattern in the polyynyl backbone. In particular, the average triple bond length is 1.20 Å, while the average single bond distance is 1.39 Å. These values are close to the typical carbon bond values previously reported for polyynyl systems,^[77] and highlight the fact that the structure itself keeps a polyynyl character rather than a cumulene one. The intermolecular distance between the terminal phosphorous atoms has been evaluated to be around 21.5 Å.

Moreover, it is worth noting the herringbone configuration assumed by the polyynyl core in the solid state, together with the formation of parallel aggregated dimers. A similar structure was also reported by S. Eisler et al.,^[59] although without the presence of dimers.

The final part of the synthetic route was devoted to the deprotection of the phosphonate, by removing the terminating diethyl moieties. A large excess of trimethylsilyl-bromide was added to a solution of the phosphonate hexayne **5** in DCM. Once the reaction was finished, the addition of 1 M HCl leads to the precipitation of a fine yellow powder, which was quickly

filtered and redissolved in a mixture of MeOH/DCM to avoid degradation. To further reduce product loss which would have arisen from a second drying step, the reaction yield was evaluated indirectly by first measuring the solution volume and then by evaluating its concentration by UV-Vis spectroscopy. In more detail, we related the absorption of the main peak of the hexayne to the concentration of our sample, by the application of the Lambert-Beer equation (**eq.1**), where the absorbance (**A**) is correlated to the molarity (**M**) and optical path (**l**) of the analyzed solution, by mean of the extinction coefficient ϵ_λ , which was determined to be $3 \cdot 10^6 \text{ cm}^{-1} \text{ M}^{-1}$ by previous studies conducted by the Frauenrath group.

$$A = l \cdot M \cdot \epsilon_\lambda \quad \text{eq.1}$$

A concentration of 5.8 mM was found for the stock solution, that is equivalent to 0.174 mmol of **6**, which implies a yield of 19%. The ^1H -NMR spectrum shows only two peaks at 2.5 ppm and at 1.85 ppm, corresponding to the protons of the alkyl spacer, while the ^{13}C -NMR analysis reports the signals of the twelve carbon atoms of the *sp*-hybridized backbone in the range between 59.53 and 80.57 ppm. These results, together with mass spectroscopy analysis, provide good evidence for the formation of the desired hexayne bolaamphiphile **6**. Overall, the total yield of the synthesis procedure is about 3% over all steps. The most important product loss arose in the first phosphonation reaction for reasons explained above and mainly during the deprotection step, particularly during the filtration of the precipitate, due to premature crosslinking of the hexayne. It is worth noting that 12 carbon atoms out of 16 (39% of the total molecular weight) are in a *sp*-hybridized state in the final synthesized product. This confirms the molecule's carbon-rich nature and explains its high reactivity to undergo carbonization in presence of light or heat, especially when kept in the solid state. For this reason, the target molecules were maintained in diluted environment at a concentration of 5.8 mmol, shielded away from light by wrapping the flask in aluminum foil.

2.2 Optical Properties of the Hexayne Bolaamphiphile

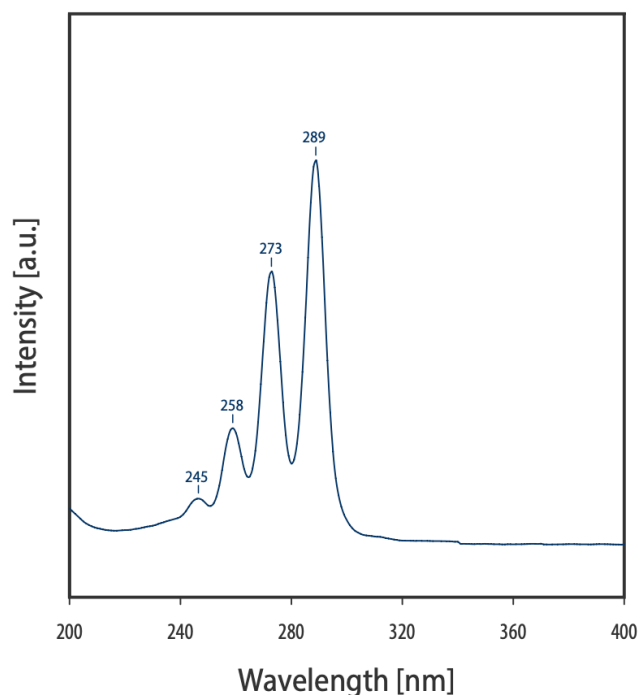


Fig. 17: UV-Vis spectrum of **6** in MeOH, with the 4 main absorption peaks of the hexayne segment, respectively at 289, 273, 258 and 245 nm.

As described in the experimental section, UV-Vis spectroscopy has been carried out to determine the concentration of hexayne solution. The hexayne is a chromophore, with a characteristic fingerprint at 200-300 nm, as shown in **Fig.17**.

Apart from the main absorption peak at 289 nm, the presence of the hexayne backbone introduces several vibrational fine structure absorption peaks respectively at 273, 258 and 245 nm. The resulting fingerprint resembles the typical response of hexayne-containing compounds as already reported by the scientific community.^[75, 78] Due to the high symmetry of the hexayne bolaamphiphile, which forbids the lowest-lying $S_0 \rightarrow S_1$ transition to occur, the nature of the main peak is due to higher-energy $S_0 \rightarrow S_n$ absorptions.^[79]

2.3 Self-assembled Monolayer from the Hexayne Bolaamphiphile

The next step is the study of the self-assembly capability of **6** on oxide surfaces and the evaluation of the best conditions required to form a well-ordered SAM at the solid-liquid

interface. In particular, the influence of the precursor concentration, as well as the temperature at which the immersion was carried out was evaluated, while the immersion time was kept equal to 1 h, and IPA was used as the solvent in all experiments. We thus tested SAM formation by immersing the substrate at three different concentrations (2, 0.2 and 0.02 mM) both at room temperature and at 60°C.

Since it is particularly challenging to establish the presence of a well-ordered monolayer on a surface, its formation has been assessed by comparing the surface properties of the coated substrates with the results coming from a SAM of hexane-1,6-bisphosphonic acid. This molecular precursor, shown in **Fig. 17**, is known to undergo effective SAM formation on alumina surfaces, changing its wettability to a WCA of around 40°, as reported in literature ^[80] and confirmed by previous studies performed by the group.

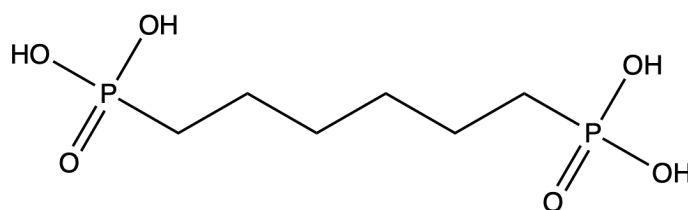


Fig. 17: Hexane-1,6-bisphosphonic acid. The phosphonic acid head groups allows closely packed monolayer formation at the solid-liquid interfaces on AlO_x surfaces.

If an effective SAM formation is hypothesized to happen on the activated alumina substrate, then a similar coverage of phosphonic head will have to be achieved. Similarly to the case of hexane-1,6,-bisphosphonic acid SAM, the surfaces should display WCA values close to 40°. At the same time, the thickness of the adsorbed organic monolayer was evaluated by ellipsometry. Consequently, a well-formed monolayer should display an ellipsometric thickness close to 2 nm, while showing a WCA value close to 40°. Results are shown in **Tab.1**.

Tab. 1: Water contact angle analysis and ellipsometric measurements performed on alumina coated wafer samples, after immersion in hexayne IPA solution at different concentrations and temperatures. The best condition found for SAM formation is highlighted in green.

	R.T 2 mM	R.T 0.2 mM	R.T 0.002 mM	60 °C 2 mM	60 °C 0.2 mM	60 °C 0.002 mM
Water contact angle [°]	70 ± 1	66 ± 1	54 ± 2	67 ± 1	53 ± 2	61 ± 1
Ellipsometry [nm]	3.0 ± 0.3	1.2 ± 0.4	0.4 ± 0.2	3.9 ± 0.4	1.8 ± 0.2	1.0 ± 0.2

Immersion at room temperatures are characterized by lower SAM homogeneity, as found in the high absolute error of the thickness which characterizes the measurements, especially in the case of 0.2 mM and the 0.02 Mm solution. At 60°C, the lowest contact angle was found to be around 53° for the 0.2 mM solution, the closest to the theoretical value of a closely-packed phosphonic acid monolayer, as previously reported. Independently from the immersion temperature, lower concentrations led to incomplete monolayer formation, as represented by the low ellipsometric thickness values. On the contrary, immersions in 2 mM solutions resulted in monolayers thicker than the target value of 2 nm, which could indicate the formation of aggregates that form prematurely in the concentrated solution and precipitate to the surface.

From these results, immersion in a 0.2 mM solution at 60°C for 1 h represents the best condition to build PA-hex-PA monolayers onto aluminum oxide surfaces, since both WCA and thickness are similar in value to the theoretical assessment previously determined for this monolayer.

2.4 Formation of the Multilayer Structure by LbL Deposition

Once the best condition for the formation of the organic monolayer from **6** had been defined, the formation of the multilayer structure by LbL was evaluated. As thoroughly described in the **Materials and Methods** section, the plasma-activated alumina substrates were immersed in the 0.2 mM IPA solution of **6** for 1 h at 60°C. After SAM formation, the substrate was washed, dried, and immersed in a solution of a zirconium complex to allow for the development of the metallic layer. Zirconium acetylacetonate $[\text{Zr}(\text{AcAc})_4]$ was chosen as a precursor due to its high solubility in polar solvents.^[53] After the second immersion, an organometallic bilayer, which will be referred to as (PA-hex-PA/Zr⁴⁺), is thus obtained. This cycle can be repeated n times to give a multilayer structure (indicated as (PA-hex-PA/Zr⁴⁺) _{n}), which will be terminated with a capping SAM of octadecylphosphonic acid, as shown in **Fig. 18**.

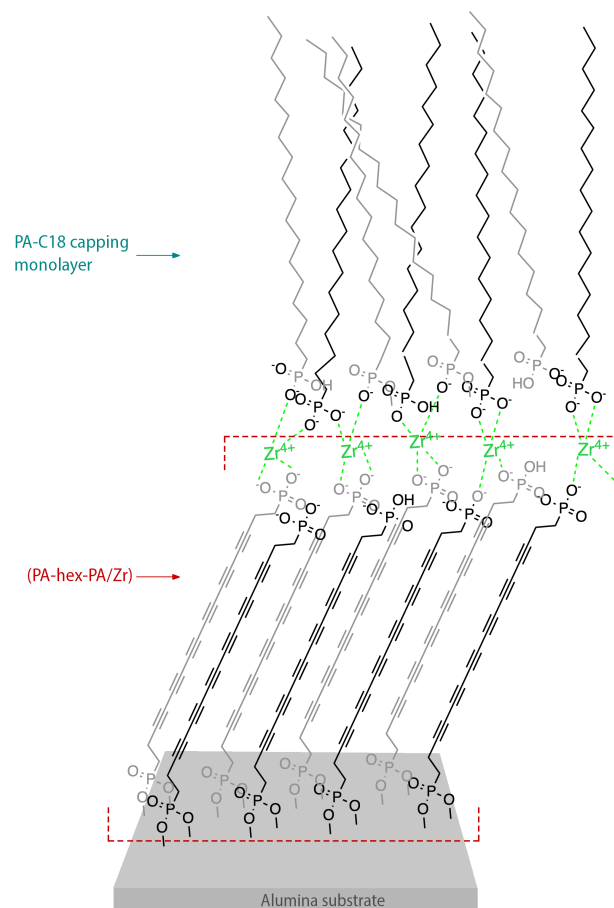


Fig. 18: Schematic representation of the multilayered structure. In the red brackets the (PA-hex-PA/Zr⁴⁺) building block, which is repeated several times to lead the multilayer. A final PA-C18 SAM terminates the multilayer.

In order to evaluate the formation and the growth of multilayered structure, samples from one to five (PA-hex-PA/Zr⁴⁺) layers have been produced and analyzed by ellipsometry, as represented in **fig. 19a**. The thicknesses increment follows a linear trend, with a 4 nm increment for each added (PA-hex-PA/Zr⁴⁺) layer, which is higher than the expected value of 2 nm. This finding could be related to some defects formation in the multilayer structure. In any case, the linear thickness increment up to five layer indicates the effectiveness of the LbL deposition technique towards the formation of a multilayer structure.

As shown by ellipsometry, the addition of layers over pre-existing ones could likely introduce an overall increase in structural disorder in the final architecture. In particular, the final capping monolayer would be influenced by the order of the ones previously deposited, especially in terms of its order and packing density. The presence of a disordered substrate would in fact induce the formation of a defect-rich PA-C18 monolayer, characterized by

gauche defects in the alkyl chains, which results in a less crystalline, close packed monolayer with respect to a pristine SAM fabricated on a flat alumina surface. To evaluate this aspect, WCA analysis and IRRA spectroscopy have been performed on the multilayer structures.

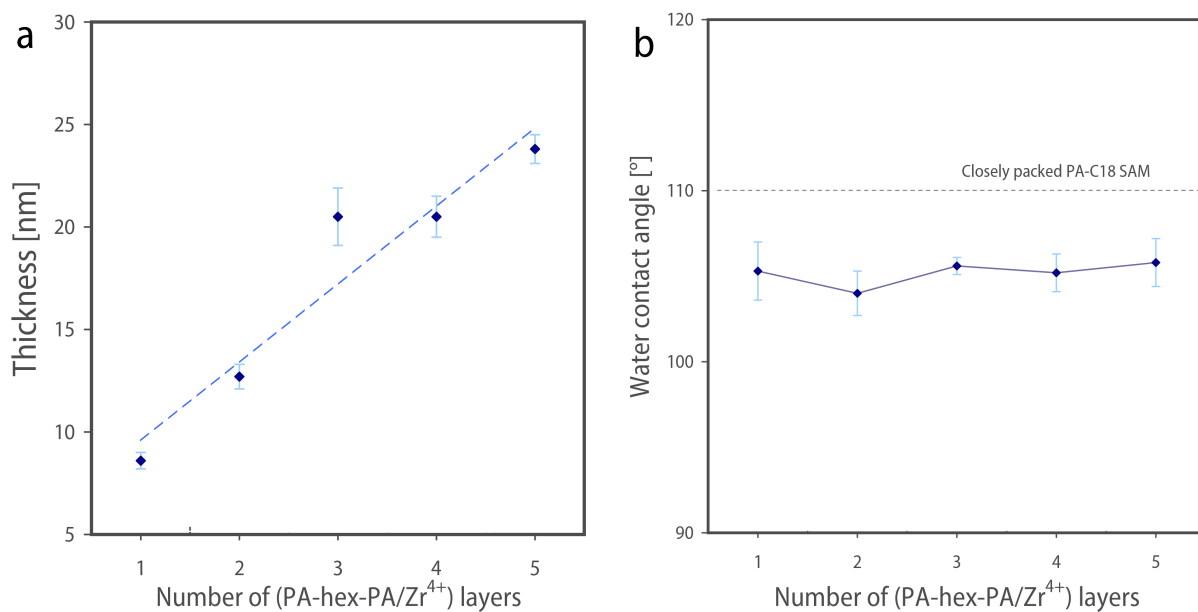


Fig. 18: Ellispometry (a) and WCA analysis (b) of substrates coated with up to five layer of (PA-hex-PA/Zr⁴⁺) and terminated with a PA-C18 monolayer.

As depicted in **Fig. 18b**, the water contact angles remained constant for different numbers of layers. According to Bauer et al.,^[81] the wettability of a PA-C18 SAM coated surface is characterized by a WCA of about 110°. All samples showed lower water contact angles compared to the reference value, and tended to stabilize at around 105° with increasing layer numbers. This indicates the formation of a dense monolayer with a certain degree of disorder. Nevertheless, it is interesting to notice that the WCA stays constant with an increasing number of layers, which indicates the formation of a comparable zirconium layer, with similar densities, at each step. The WCA values measured for all the samples, together with their low variation, reinforce the hypothesis of an ordered multilayer coating formation comprising some degree of disorder.

To further assess the structural disorder of the multilayered structures, IRRA spectroscopy was performed on all samples to evaluate the crystallinity of the terminal octadecylphosphonic acid monolayer. Indeed, as reported in the literature, a useful parameter to characterize the ordering of the monolayer is the position of the methylene symmetric and

asymmetric stretching modes, which tend to shift to higher frequencies with decreasing conformational order of the alkyl chain. Well-formed aliphatic monolayers are characterized by alkyl chain retaining all-*trans* configuration, with an IR peak position of the symmetric stretching mode lower than 2850 cm^{-1} and an asymmetric stretching mode lower than 2920 cm^{-1} .^[82]

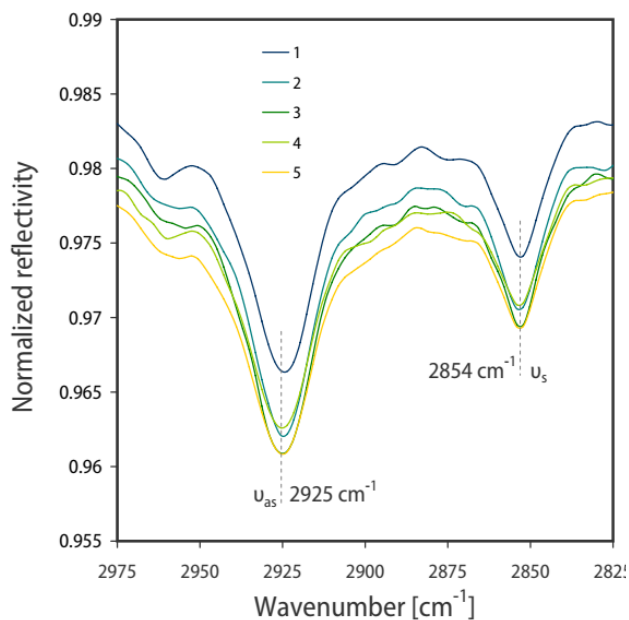


Fig. 19 : IRRAS spectra of the multilayer coatings at varying number of (PA-hex-PA/Zr⁴⁺) layers. The two characteristic peaks of the symmetric and asymmetric vibrational are highlighted.

Fig. 19 reports the IRRAS spectra for different multilayer architectures at increasing number of (PA-hex-PA/Zr⁴⁺) deposited layers. For all multilayer samples, the end-capping PA-C18 monolayers displayed a shift a higher frequency for both the asymmetric and the symmetric vibrational mode. This is in agreement with the presence of *gauche* conformations in the alkyl segments and thus corroborates a certain degree of disorder in the multilayer structure that, however, remains constant over the number of layers.

2.5 Carbonization of the Multilayer Structure

With the effective formation of the multilayer architecture by LbL deposition proven, we proceeded to investigate its conversion from stacked layers of hexayne molecules to a carbon multilayer structure upon UV irradiation. UV-Vis spectroscopy represents an interesting means to evaluate this transition, since the UV fingerprint of the hexayne is expected to

disappear as the carbonization proceeds. The study was carried out on a five-layer system (PA-hex-PA/Zr⁴⁺)₅ on a single-crystalline alumina substrate, which allows UV light to pass through.

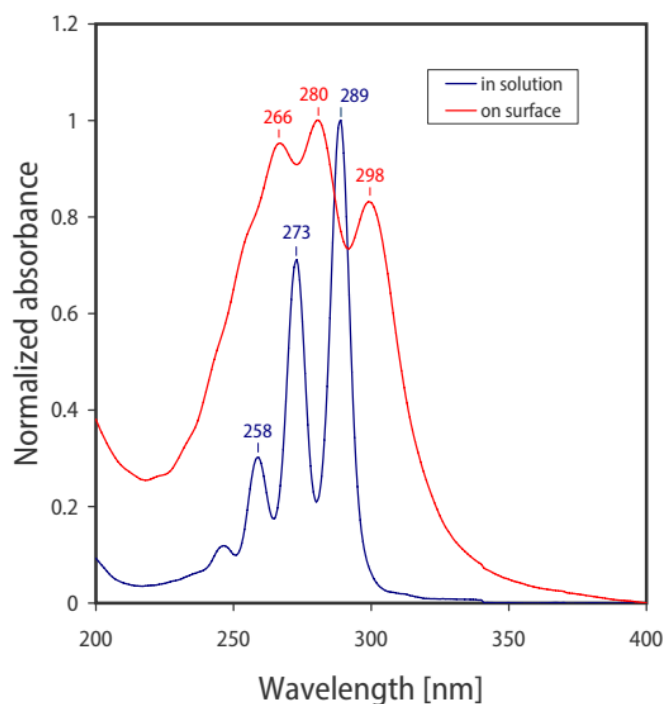


Fig. 20: UV-Vis spectra comparison between the unprotected hexayne in IPA and the same molecule self-assembled on AlOx surfaces

As depicted in **Fig. 20**, the formation of multilayers introduced a marked blue shift of the peaks (up to 9 nm for the peak at 289 nm) compared to the spectral fingerprint of the hexayne in IPA solution. The peaks of the self-assembled multilayer structure before irradiation became also significantly broadened and showed a reduced intensity ratio of the first to the second vibronic transition, from 1.41 in solution to 0.83 in the multilayer structures. These observations are in line with the formation of spectroscopic H-aggregates which suggests the predominant cofacial arrangement of the hexayne chromophores within the layered nanostructure into a dense, multilayer structure.^[71]

In **Fig. 21**, the disappearance of the hexayne signal with increasing irradiation time can be observed. The total conversion was achieved after three hours of irradiation. One hour of exposure ensures the conversion of more than 95% the molecular multilayer structure into an carbon multilayer coating.

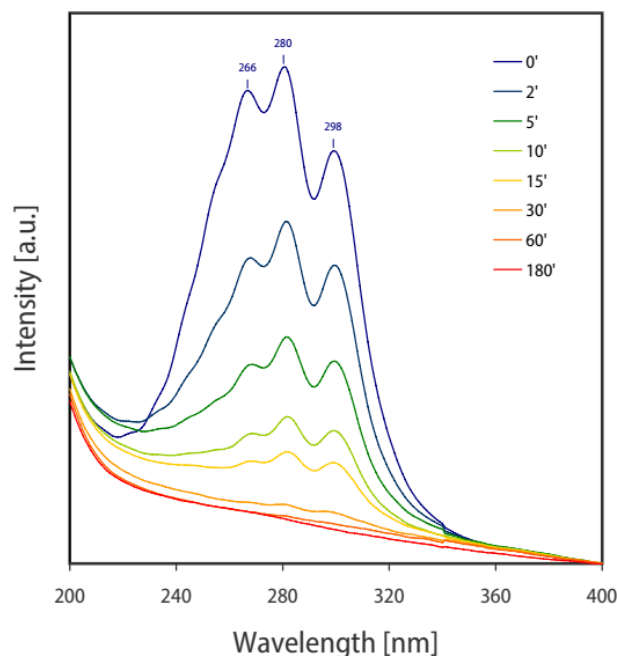


Fig. 20: Cumulative spectra of $(\text{PA-hex-PA/Zr}^{4+})_5 + \text{PAC18}$ multilayer on crystalline alumina substrate, before ($0'$) and at different UV irradiation time.

To further evaluate the carbonization process and its outcome, Raman spectra of the $(\text{PA-hex-PA/Zr}^{4+})_5$ multilayer on an alumina-coated wafer sample were recorded before and after UV irradiation. The relatively high carbon content on the sample surface allowed Raman signal detection without the need of surface-enhanced techniques. However, the recorded signals are characterized by a low sensitivity and high signal-to-noise ratio as a result.

Thanks to the Raman analysis, it is possible to determine the nature of the carbon structure after crosslinking. According to Ferrari et al.^[83], the typical Raman spectrum of an sp^2 -rich system (i.e., disordered graphite) shows the so-called G band at around 1590 cm^{-1} and the D band at around 1350 cm^{-1} . **Fig. 22** shows the spectra of the molecular multilayer as well as the carbonized structure. The two typical bands for the carbon nanomaterials were fitted by a Gaussian distribution, showing their maxima to be at 1294 cm^{-1} and at 1470 cm^{-1} , respectively, for the D and the G band. The observed shifts of both the typical carbon signal are in line with the characteristic signals developed by amorphous carbon. The presence of the D band compared to the G band and their intensity ration of $I_D/I_G \simeq 0.5$ prove the presence of disorder in the carbonaceous nanocoating. The Raman spectrum of the not irradiated multilayer, on contrary, does not display the signature peaks of carbon nanomaterials, further indicating that no premature carbonization occurs in the molecular multilayer.

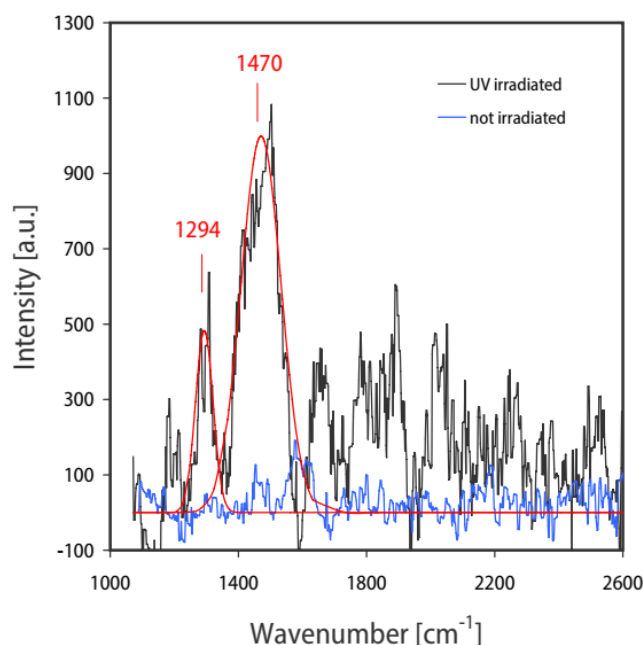


Fig. 22: Raman spectra of the not-irradiated (in blue) and of the UV-induced (in grey) crosslinked multilayer. The typical fingerprints of the carbonaceous material (D band at 1294 cm^{-1} and G band at 1498 cm^{-1}) are fitted, in red, by two Gaussian curves.

In summary, UV-irradiation effectively induces the crosslinking of the hexayne multilayer, which displays a $>95\%$ conversion after 1h of UV-light exposure. The low-temperature carbonization results in a disordered carbon nanomaterial which shown no sign of a graphitic structure development.

2.6 Effect of Carbonization on Multilayer Disorder

To evaluate the effect of carbonization on the structural stability of the multilayer, as well as the formation of defects induced by the process, such as increased roughness, local delamination or cracks, the coated samples (from one to five multilayers) were investigated by ellipsometry, WCA analysis, and IRRA spectroscopy. The results from the analyses are shown in **Fig. 23**, in comparison to the results obtained before UV irradiation.

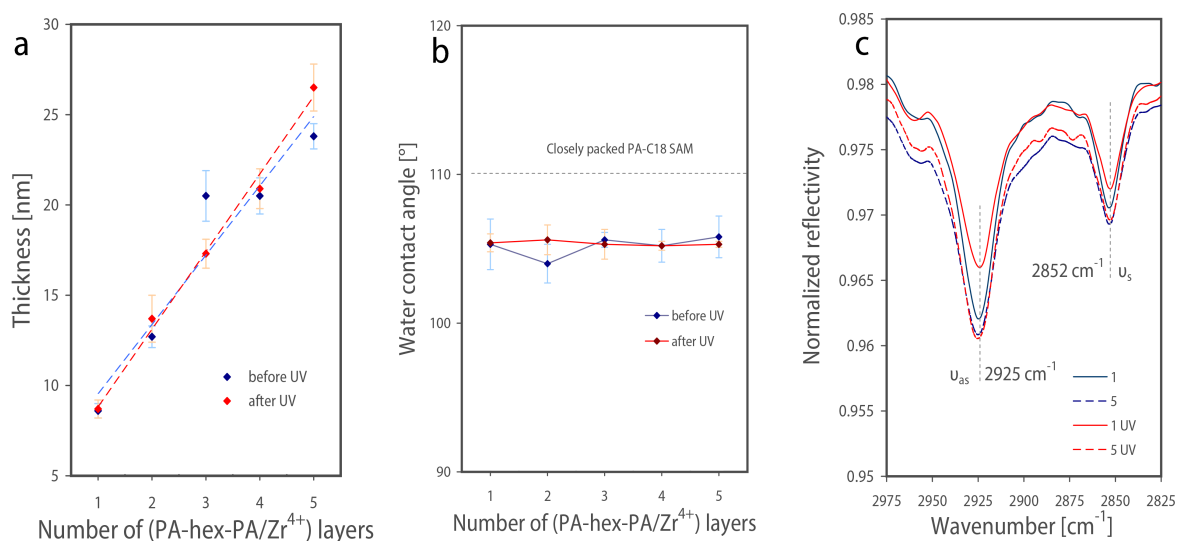


Fig. 23: Ellipsometry analysis of the multilayer coating before and after UV irradiation (a), together with WCA analysis (b) and IRRA spectroscopy (c).

After carbonization, the multilayer structure displays a similar thickness increment if compared to the data before UV irradiation. The similar ellipsometric results reported in **Fig. 23a** give no indication of delamination or film breakage after crosslinking. Moreover, it is interesting to note how topochemical polymerization does not induce shrinkage nor expansion in the *z* direction, which would on the contrary introduce cracks in the carbon films, rather than leading to different thickness values. WCA analysis produced comparable contact angle values before and after UV irradiation, indicating a similar surface system with similar wetting properties, as visible in **Fig. 23b**. The IRRA spectroscopy measurements performed on the UV-irradiated samples did not show a shift the -CH₂ signals to higher frequencies as a consequence of carbonization. In line with the WCA and ellipsometry analysis, this shows that no morphological changes, such as cracks or coating failure, occur during crosslinking.

2.7 Structural Analysis of the Multilayer Coating

2.7.1 Surface Evaluation by AFM

AFM was used to evaluate the changes in surface roughness with an increasing number of deposited layers, as well as eventual cracks or defects that could have arisen in the carbon coating during UV irradiation. The AFM surface maps of samples coated with a (PA-hex-PA/Zr⁴⁺) SAM or five (PA-hex-PA/Zr⁴⁺)₅ layers before and after carbonization are shown in

Fig. 24, with a close-up in **Fig. 25**. Going from one to is accompanied by more roughness and deposits, as represented in **Tab. 2**, where it is straightforwardly visible how the average surface roughness increases at higher layer number. The irradiation step plays a variable effect on the coating. In the five-layer coating, no cracks or wrinkles can be observed. Moreover, the surface roughness does not evolve significantly before and after irradiation.

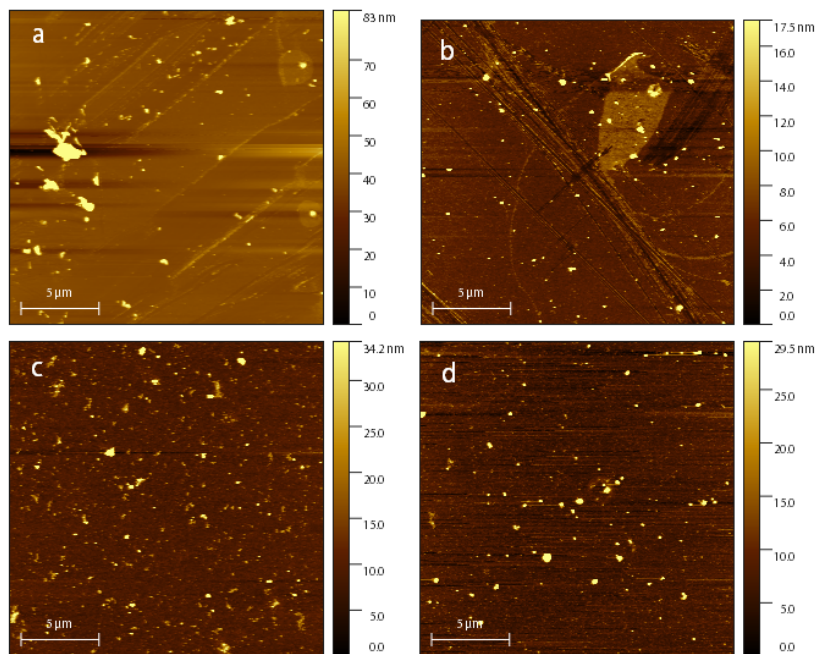


Fig. 24: AFM surface measurement of a deposited (PA-hex-PA/Zr⁴⁺) before (a) and after UV irradiation (b) and 5 layers both before (c) and after carbonization (d).

By contrast, the monolayer sample shows the development of a wrinkled pattern, which could be due to local deformation of the deposited film during carbonization, in agreement with the three-fold increment of the surface roughness after crosslinking. The phenomenon is supposedly not noticeable at a higher number of deposited layers, because the presence of nanoaggregates renders the surface rough and heterogeneous even before carbonization.

Table 2: Effect of carbonization on the average surface roughness (R_a) of the multilayered coating at different number of deposited layers.

	Not carbonized	carbonized
1 layer (PA-hex-PA/Zr ⁴⁺)	224 pm	716 pm
5 layer (PA-hex-PA/Zr ⁴⁺)	1703 pm	1550 pm

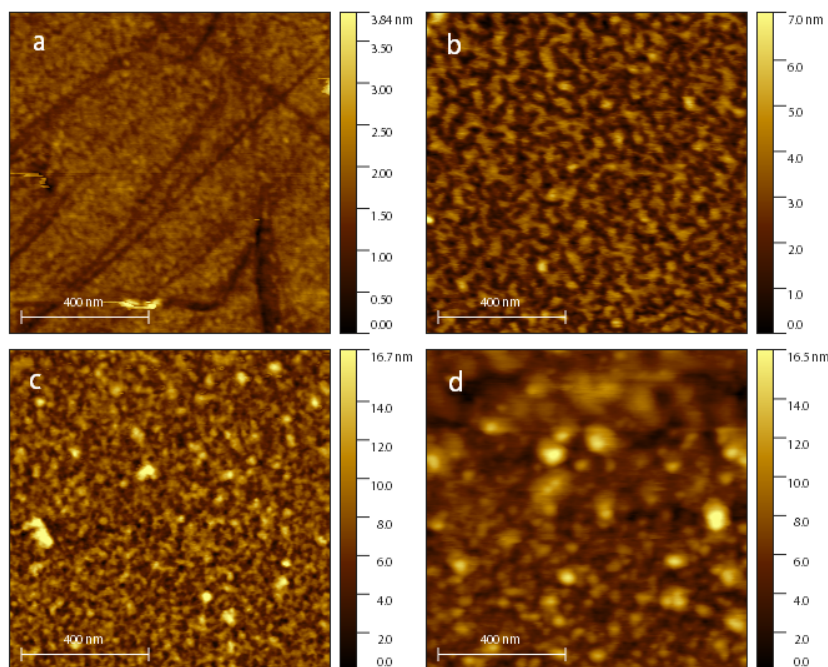


Fig. 25: AFM surface measurement close-up of a deposited hexayne-zirconium layer before (a) and after UV irradiation (b) and 5 layers both before (c) and after carbonization (d).

2.7.2 TEM Analysis of the Multilayer Cross Section

To obtain a complete picture of the multilayer structure, it was analyzed by means of high-resolution TEM. To better observe the carbon multilayer, the analysis was performed on a nine-layer system (PA-hex-PA/Zr⁴⁺)₉, end-capped with PA-C18 and after UV-irradiation. In the TEM micrographs shown in **Fig. 26**, it is possible to observe the dark silicon substrate and the alumina coating with the carbon-based multilayer on top. It is also possible to spot some remaining of the glue used to prepare the sample, placed on top of the carbon coating and characterized by lighter color. Theoretically, since the atomic number of carbon and zirconium are different, it should have been possible to observe a contrast between the carbon-rich layers and the zirconium layers. This could have been a strong proof of the layered nature of the organometallic coating. Unfortunately, even at the highest magnification, with the objective lens and without defocusing (which could introduce misleading artifacts), no tonal contrast could be observed. This, on the other side, may be interpreted to be the result of structural disorder of the carbon coating.

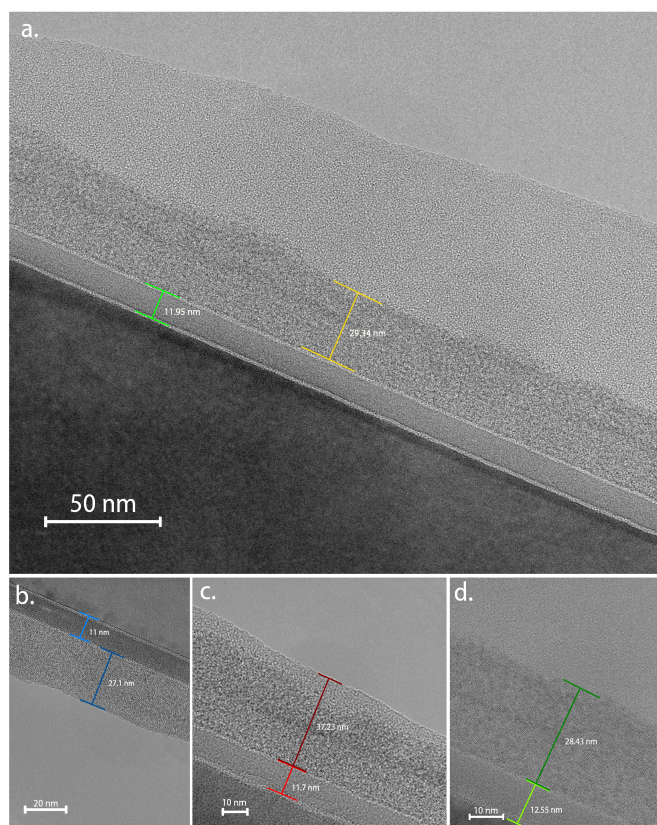


Fig. 26: TEM cross section images of a (PA-hex-PA/Zr⁴⁺)₉ multilayered structure on alumina coated silicon wafer, taken at different magnifications.

Nevertheless, TEM analysis shows the formation of a continuous, nanometric coating, without cracks or delamination phenomena, supporting the consistency of the previous analyses, as well as the effectiveness of the LbL deposition technique.

2.8 Corrosion Tests

Potentiodynamic measurements were performed on polished pure aluminum substrates coated with a five-layer system (PA-hex-PA/Zr⁴⁺)₅ and end-capped with a monolayer of octadecylphosphonic acid, one of which was further subjected to carbonization to study the effect of crosslinking the hexayne monolayers on corrosion protection. Compared to the bare aluminum specimen, the presence of the multilayered structure increased the surface resistance from 0.48 MΩ to 6.06 MΩ. As shown in the Tafel plot in **Fig. 27**, the coated sample displayed a decrease in both the anodic and the cathodic currents by about one order of magnitude, which leads to an overall reduction in the corrosion current density from 5.1 to 0.30 μA cm⁻². Moreover, we observed a shift in the open circuit potential (OCP), the voltage that characterizes the sample surface during the corrosion evaluation, when no current is

being applied to the corrosion system. The change from -0.62 to -0.41 V demonstrates the efficacy of the coating in increasing the resistance of the substrate to the corrosive effect of the electrolyte, making the surface more resistant to corrosion phenomena.

However, the subsequent carbonization of the multilayered structure appeared to decrease the corrosion resistance parameters to some extent. In particular, the decrease in the surface resistance (from 6.06 to 3.28 $M\Omega$) as well as an increase in the corrosion current density (from 0.3 to 0.63 $\mu A\ cm^{-2}$) indicates less effective corrosion protection, as further shown by the negative shift in the OCP, as shown in **Tab. 3**.

A possible explanation might be the increase in rigidity of the carbonized coating, which might promote the formation of nanoscopic cracks in response to the surface stresses internally developing during the corrosion test. Moreover, it is worth remembering that the pure aluminum surface is characterized by a residual but not negligible roughness, which could have prevented the homogeneous formation of a multilayered carbon coating.

Tab. 3: Polarization resistance and corrosion current densities extrapolated from the potentiodynamic tests.

	Open Circuit Potential [V]	Polarization resistance R_p [$M\Omega$]	Corrosion current density J_{corr} [$\mu A\ cm^{-2}$]
Bare aluminum	-0.62	0.48	5.10
Coated, not carbonized	-0.41	6.06	0.30
Coated and carbonized	-0.51	3.28	0.63

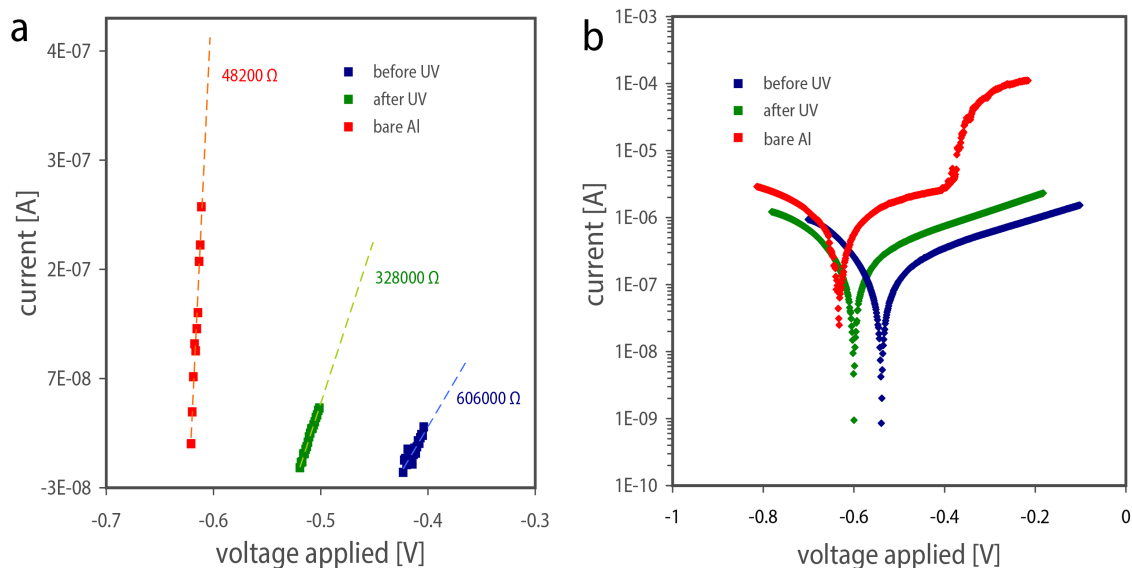


Fig. 27: Potentiodynamic polarization measurements performed on bare aluminum sample as well as on $(\text{PA-hex-PA/Zr}^{4+})_5 + \text{PA-C18}$ coated aluminum samples. Polarization resistance are evaluated in fig. a, while Tafel plots are represented fig. b.

Overall, the multilayered structure on top of the aluminum samples increases the corrosion protection while inducing a more noble behavior of the aluminum substrate towards the corrosive electrolytic environment. Moreover, the lower corrosion current densities displayed by the samples indicated slower corrosion kinetics, which translates in better maintenance of the substrate integrity in the corrosive medium.

3. Conclusions and Outlook

Oligoynes are promising molecular precursors for the formation of carbon nanomaterials, thanks to their high reactivity and their tendency to carbonize when exposed to mild UV irradiation at room temperature. These molecules can comprise additional chemical functionalization, which gives them interesting self-assembly capabilities. As shown in this thesis, we successfully prepared an organometallic multilayer coating on alumina substrates by exerting the self-assembly capability and the UV-induced carbonization of alternating layers of a hexayne bisphosphonic acid and zirconium.

A six-step synthesis was carried out to obtain the hexayne bisphosphonic acid, which consisted in the introduction of the protected phosphonate, the bromination of the terminal alkyne, the Negishi coupling with 1,4-bis(trimethylsilyl)butadiene, the modified Eglinton-Galbraith homocoupling and the cleavage of the protective ethylenic groups from the phosphonate was obtained in an overall yield of 3% as a highly reactive yellow solid.

We evaluated the best conditions to grow a SAM from the hexayne, and then explored an LbL approach to form a multilayer structure. The deposition technique was found to be suitable and effective in the formation of multilayer, since a linear increase in thickness upon each added (PA-hex-PA/Zr⁴⁺) layer was recorded. The structure of the multilayer was found to be independent of the number of deposited SAMs, as it displayed similar wettability and similar ordering of the terminal capping layer, despite displaying a certain degree of structural disorder. The consequent carbonization of the metalorganic multilayers by UV irradiation resulted in the formation of a mechanical stable, amorphous nanocoating, which, however, showed no clear sign of a layered zirconium-carbon architecture. The carbonization process did not induce any shrinkage or expansion in the coating, without the development of cracks or delamination that could undermine the structural stability of the carbon coating. Eventually, potentiodynamic analysis assessed the effectiveness of the coating as solution for corrosion protection, since the presence of the carbon multilayer increases the surface polarization resistance, while reducing the corrosion current density, both by about one order of magnitude compared to bare aluminum substrates.

As an outlook, a deeper investigation of the multilayer structure could be envisaged by HREELS to evaluate in more detail the zirconium distribution in the coating. Moreover, the cation could be substituted with other positively charged elements, such polymers or charged 2D nanomaterials, which could potentially introduce better corrosion properties. Finally, the continuous carbon structure resulting from adsorption and subsequent UV-irradiation could be further used in the formation of carbon coating on nanoparticles for example leading to core-shell architectures.

4.1 Materials and methods

All the reagents used in the synthesis hereby described were purchased from available commercial sources and used without any purification step. Chromatography solvents were purchased as reagent grade solvent and further distilled before use by mean of rotary evaporator. Several types of substrates were used for the self-assembly of the phosphonic acids. Aluminum oxide (AlO_x) substrates were fabricated by atomic layer deposition (ALD, *BENEQ TFS200*) of a 10 nm AlO_x layer onto silicon wafer substrates. Commercial r-plane sapphire (Al₂O₃) substrates were purchased from *Alineason Materials Technology GmbH, Germany*. Substrates suitable for IRRA spectroscopy has been produced by sputtering gold on silicon wafer before a thin film of TiO₂ has been deposited on top, to reduce the mechanical stress that could developed prior direct application of the terminal 10 nm AlO_x film. Commercial aluminum substrates (99.999% purity), purchased from *Koch-Light Laboratories Ltd, UK*, were polished with silicon carbide paper (2400 and 4000 grade) and a 1/4 μm diamond suspension in order to obtain an aluminum surface with a mirror finish.

Synthesis procedure

[2] Diethyl but-3-yn-1-ylphosphonate

Diethyl phosphite (3.12 g, 22.56 mmol, 1.18 eq) was added to a solution of NaHMDS (11.28 g, 22.56 mmol, 1.18 eq) in THF (50 mL) at -10°C. The mixture was stirred for 15 min, then a solution of 4-bromo-1-butyne (2.55 g, 19.18 mmol, 1 eq) in THF (50 mL) was added and the system was stirred overnight. The reaction was quenched by the addition of HCl 1M. The organic phase was washed three times with DCM, then twice with HCl 1M, once with NaOH 1M, twice with brine and eventually dried over Na₂SO₄. The product was dried and purified by column chromatography (silica gel, eluent DCM/MeOH 97.5:2.5) to yield diethyl tetr-3-ynylphosphonate **2** as yellowish oil (1.34 g, 7.04 mmol, 35%).

¹H NMR (400 MHz, Chloroform-*d*) δ 4.09 – 3.85 (m, 4H), 2.35 (qt, *J* = 7.8, 3.3 Hz, 2H), 1.87 (dtt, *J* = 11.6, 8.8, 4.7 Hz, 3H), 1.20 (dp, *J* = 10.6, 3.7 Hz, 6H). ¹³C NMR (101 MHz, CDCl₃) δ 82.79, 82.59, 69.05, 69.03, 61.79, 61.72, 25.93, 24.52, 16.45, 16.39, 12.53. ³¹P NMR (162 MHz, CDCl₃) δ 28.89. HRMS (APPI/LTQ-Orbitrap) *m/z*: [M + H]⁺ Calcd for C₈H₁₆O₃P⁺ 191.0832; Found 191.0811.

[3] Diethyl (4-bromobut-3-yn-1-yl)phosphonate

To a solution of BrNHS (1.27 g, 7.14 mmol, 1.01 eq) in dry MeCN (50 mL) were added consecutively **2** (1.34 g, 7.04 mmol, 1 eq) and AgNO₃ (0.347 g, 2.04 mmol, 0.29 eq). The reaction mixture has been stirred for 3h under Ar atmosphere, then quenched by the addition of HCl 1M (50 mL). The organic phase was washed three times with DCM, twice with HCl 1M, once with brine and eventually dried over Na₂SO₄. The fraction was then concentrated to obtain **3** as a yellowish oil (1.7 g, 6.32 mmol, 90%).

¹H NMR (400 MHz, Chloroform-*d*) δ 4.03 (dtd, *J* = 11.4, 7.3, 4.6 Hz, 4H), 2.50 – 2.35 (m, 2H), 1.98 – 1.82 (m, 2H), 1.26 (td, *J* = 7.3, 3.6 Hz, 6H). ¹³C NMR (101 MHz, CDCl₃) δ 78.55, 78.35, 61.84, 61.78, 39.34, 39.32, 25.62, 24.21, 16.47, 16.41, 13.83, 13.79. ³¹P NMR (162 MHz, CDCl₃) δ 28.72. HRMS (APPI/LTQ-Orbitrap) *m/z*: [M + H]⁺ Calcd for C₈H₁₅BrO₃P⁺ 268.9937; Found 268.9947.

[4] Diethyl (8-(trimethylsilyl)octa-3,5,7-triyn-1-yl)phosphonate

To a solution of bis-trimethylsilylbutadiyne (2.027 g, 10.43 mmol, 1.65 eq) in dry THF (13,2 mL) at 0°C was added MeLi • LiBr solution in Et₂O (2.2 M, 4.6 mL, 10.11 mmol, 1.6 eq) drop-wisely under argon and stirred 30 min at room temperature. The resulting mixture was cooled down at 0°C and ZnCl₂ (1.9 M in THF, 5.5 mL, 10.43 mmol, 1.65 eq) was slowly added and stirred for other 30 min. In parallel, Pd(bis-diphenylphosphinoferrrocene) dichloride (106 mg, 0.13 mmol, 0.02 eq) was dissolved in dry toluene (66.13 mL). The suspension was cooled down to 0°C, *n*-BuLi (2.5 M in hexane, 0.28 mL, 0.7 mmol, 0.11 eq) was carefully added drop by drop and stirred 30 min at room temperature. Flasks were again cooled down to 0°C, consequently the zinc-diacetylide solution was transferred in the second flask by mean of a canula, while **3** was added simultaneously with a syringe. The resulting mixture was stirred for two days at room temperature covered with an aluminum foil to prevent exposure to light. Et₂O and a saturated solution of NH₄Cl were added to quench the reaction.

The resulting biphasic mixture was fractionated, and the organic-rich phase washed twice with NH₄Cl, once with brine before being dried with anhydrous Na₂SO₄ and concentrated *in vacuo*.

The crude obtained was purified by column chromatography (silica gel, eluent DCM/MeOH 97.5:2.5) to give **4** as a brown oil (1.48 g, 4.768 mmol, 76%).

¹H NMR (400 MHz, Chloroform-*d*) δ 3.91 (qdd, *J* = 7.6, 6.7, 4.4 Hz, 4H), 2.41 (ddd, *J* = 12.7, 8.4, 7.1 Hz, 2H), 1.86 – 1.73 (m, 2H), 1.13 (t, *J* = 7.0 Hz, 6H), 0.00 (d, *J* = 0.7 Hz, 9H). ¹³C NMR (101 MHz, CDCl₃) δ 88.59, 86.68, 78.94, 78.75, 66.82, 66.80, 62.50, 62.43, 62.41,

61.35, 25.78, 24.37, 16.99, 16.93, 14.23, 14.20, 0.00. ³¹P NMR (162 MHz, CDCl₃) δ 28.02. HRMS (ESI/QTOF) m/z: [M + H]⁺ Calcd for C₁₅H₂₄O₃PSi⁺ 311.1227; Found 311.1233.

[5] Tetraethyl hexadeca-3,5,7,9,11,13-hexayne-1,16-diylbis(phosphonate)

CsF (398.4 mg, 2.62 mmol, 1.1 eq) and Cu(OAc)₂ (0.65 g, 3.58 mmol, 1.5 eq) were added to a solution of **4** (0.74 g, 2.38 mmol, 1 eq) in a mixture of DCM/MeOH/2,6-lutidine (20 mL/20mL/ 7mL) and stirred for 4 h. The reaction was quenched by the addition of water and DCM, then the organic phase was purified once with water, twice with HCl 1M, once with brine and finally dried over Na₂SO₄. The resulting oil fraction was concentrated and purified by column chromatography (silica gel, eluent DCM:MeOH 95:5) and then dried, to obtain **5** as a solid brown powder (0.43 g, 0.9 mmol, 76%). The product was kept in a solution of DCM to avoid carbonization.

¹H NMR (400 MHz, Chloroform-*d*) δ 4.07 – 3.90 (m, 8H), 2.51 (dt, *J* = 13.0, 7.8 Hz, 4H), 1.87 (dt, *J* = 17.4, 7.7 Hz, 4H), 1.20 (t, *J* = 7.1 Hz, 12H). ¹³C NMR (101 MHz, CDCl₃) δ 79.40, 79.21, 66.32, 66.30, 62.39, 62.37, 61.96, 61.93, 61.90, 61.86, 61.77, 61.11, 25.02, 23.60, 16.42, 16.36, 13.79, 13.75. ³¹P NMR (162 MHz, CDCl₃) δ 27.59. HRMS (ESI/QTOF) m/z: [M + Na]⁺ Calcd for C₂₄H₂₈NaO₆P₂⁺ 497.1253; Found 497.1257.

[6] Hexadeca-3,5,7,9,11,13-hexayne-1,16-diylbis(phosphonic acid)

TMS-Br (0.75 mL, 5.4 mmol, 6 eq) was added dropwise to a solution of **5** (0.43 g, 0.9 mmol, 1 eq) in DCM at 0°C. The reaction was stirred 3 h and then quenched by the addition of DCM. The solution was introduced in a separatory funnel and **6** was precipitated by the addition of HCl 1 M. The precipitate was filtered, collected by the addition of MeOH/DCM and quickly dissolved in a mixture of MeOH/DCM to avoid degradation.

The solution was then distilled, even though the presence of new precipitate required another filtration step and consecutively stabilization in MeOH/DCM mixture. Compound **6** was obtained as an orange solution in MeOH/DCM (30 mL, 5.8 mM, 0.174mmol, 19%), which has been kept away from light to avoid further carbonization.

¹H NMR (400 MHz, Methanol-*d*₄) δ 2.62 – 2.42 (m, 2H), 1.94 – 1.78 (m, 2H). ¹³C NMR (101 MHz, MeOD) δ 80.57, 80.37, 64.73, 62.17, 61.48, 60.49, 59.53. ³¹P NMR (162 MHz, MeOD) δ 25.73. HRMS (ESI/QTOF) m/z: [M + H]₋₁⁻ Calcd for C₁₆H₁₁O₆P₂⁻ 361.0036; Found 361.0036.

TLC analysis and chromatography

TLC plates were provided by Merck (silica gel 60 F254). TLC detection was performed by immersion in KMnO_4 or by exposure to UV light (254 nm). Silica gel Geduran Si 60 from Merck (40 – 60 nm) was used to perform column chromatography.

NMR analysis

AVANCE 400 NMR instrument from Bruker was used to evaluate respectively ^1H , ^{13}C and ^{31}P NMR spectra for the final molecule as well as for all the products obtained during the intermediate reaction steps.

UV-Vis spectroscopy

Ultraviolet-visible spectroscopy (UV-Vis) measurements were performed with JASCO V-670 spectrometer. To evaluate the concentration of **6** in the MeOH/DCM solution, UV-Vis spectroscopy was used. The stock solution has been diluted respectively in 500, 1000 and 1500 parts of isopropanol and the absorbance spectra was registered for all the solution. Lambert-Beer law was applied to evaluate the concentration of the diluted samples, by assessing the absorbance of the peak at 298 cm^{-1} , which was correlated to an extinction factor of 3000000 by previous studies carried out by the Frauenrath group. The result was finally multiplied by the diluting factor to obtain the concentration of the stock solution.

X-ray crystal diffraction

X-ray diffraction analysis was performed on a needle-like crystal of **5**, obtained by slow evaporation of a solution in DCM at -17°C .

Substrate cleaning and surface activation

The self-assembly procedure was performed on smooth wafer surfaces (10 x 18 mm) covered by a thin layer of Al_2O_3 ($\approx 10\text{ nm}$) deposited by Atomic Layer Deposition. All substrates were sonicated in IPA for 10 min, washed with IPA and dried under argon flow. Surface activation was performed by mean oxygen plasma (*Diener electronic Femto*).

Bisphosphonic acid hexayne self-assembly

A solution of **6** was prepared in IPA and filtrated with a syringe filter (0.22 μm pore size PTFE membrane) before any immersion.

Different solution concentrations at two different temperatures (room temperature and 60°C)

were investigated to determine the best self-assembly condition of **6**. After the immersion time, each sample was removed from solution, rinsed with isopropanol, and dried over argon flow.

Zirconium monolayer and multilayer formation

The formation of the Zirconium layer on top of the self-assembled monolayer of **6** was performed by immersion of the (PA-hex-PA) coated samples in a solution of $\text{Zr}(\text{acac})_4$ at 5 mM in ethanol.

The immersion has been performed for 1h at room temperature, then the substrates were removed from the solution, rinsed with ethanol, and dried over argon flow. The immersion process in the bisphosphonic acid solution and then in the zirconium solution can be repeated n times to form the multilayered structure $(\text{PA-hex-PA}/\text{Zr}^{4+})_n$.

On all $(\text{PA-hex-PA}/\text{Zr}^{4+})_n$ coated samples a final immersion in octadecylphosphonic acid 0.2 mM solution in IPA at 60°C for 1h is performed to terminate the multilayered structure. After immersion, samples are removed from the PA-C18 solution, rinsed with IPA and dried over argon flow, as depicted in **fig. 29**.

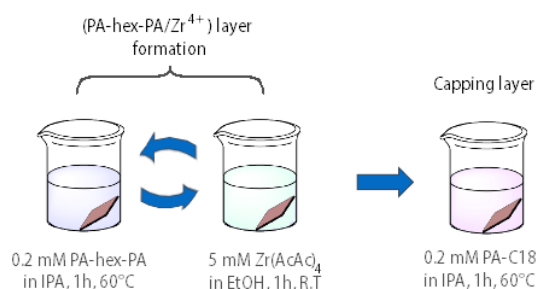


Fig. 29: Schematic representation of the LbL method for the formation of the multilayered coating.

Static water contact angle (WCA) analysis

Water contact angle analyses have been performed using a *Krüss DSA30* contact angle goniometer setup. De-ionized water (*MilliQ grade, Merck Millipore*) was used to form the sessile drop on the sample surface, which shape was subsequently fitted to the Young-Laplace equation using the in-built software *AVANCE* to determine the WCA. At least three WCA measurements were performed at different locations on each sample. The mean WCA value was recorded, together with its standard deviation.

Thickness evaluation by ellipsometry

Thickness evaluation has been performed on all coated sample, by using a *SEMILAB SE-2000* ellipsometer. For each sample measurement were done at three different locations and the reflected beam spectra were recorded at angle of 65° , 70° and 75° to the surface normal direction. The

in-built software *SEA* has been used to fit the ellipsometric data. The alumina layer thickness was set according to previous ellipsometric measurements, while the organic phase was modeled as a Cauchy diffused layer with constant refractive index of 1.4 and b-parameter equal to $0 \mu\text{m}^2$.

UV irradiation and carbonization

The irradiation step was performed at room temperature using a 400W iron doped UV light. The sample to be irradiated was placed in a glass flask and flushed with argon thrice before sealed.

The sealed flask was then placed at about 20 cm far from the UV lamp, and the irradiation was performed for 1 hour.

AFM surface measurements

Surface topographies were recorded by tapping mode atomic force microscopy (AFM) in air on an *Asylum Research Cypher S* scanning probe microscope (*Oxford Instruments, UK*). Silicon cantilever (*Mikromasch HQ:NSC18/AL BS*) were used for imaging.

Each image recorded by AFM was scanned at a resolution of 256 lines at 0.7 Hz and analyzed with the *Gwiddion* software to determinate the morphology, as well as the roughness and the surface profile. For each sample, a starting area of $20 \times 20 \mu\text{m}^2$ was initially scanned to evaluate the surface morphology, while the average surface roughness (Ra) was determined from scan areas of $1 \times 1 \mu\text{m}^2$.

Raman spectroscopy

Raman spectroscopy measurements were carried out in a Renishaw inViaTM confocal Raman microscope using a laser wavelength of 532 nm and 405 nm. The laser power was optimized to obtain a good signal-to-noise ratio in the spectra.

TEM sample preparation and analysis

In order to analyze the UV-irradiated nine multilayer carbon coating by high resolution transmission electron microscopy (HR-TEM), a cross section of the specimen was produced. The substrate was cut by scratching the rear surface with a diamond cutter, and by impressing a small pressure on the formed defect. The central stripe of the sample was cut away and further split in half. The two parts were glued together by applying a thermosensitive paste on the organic-coated surface. The resulting sample was then polished, and one corner was ion-milled to get a thin film of the coating cross section. TEM analysis was performed with the high resolution *ThermoFischer Scientific Talos F200S G2* microscope, with an accelerating voltage of 200 kV and a spot size of 8, using the low dose unit to limit beam damage to the nanocoating during image acquisition at high magnifications. Cross section images were taken in bright field, as well as with the introduction of the objective lens.

Infrared Reflection-Absorption (IRRA) spectroscopy

IRRAS spectra have been recorded using the *VERTEX 80/80v* FT-IR interferometer by *Bruker*, characterized by a liquid nitrogen cooled MCT detector. The *p* polarized mid IR beam was focused on the surface of the sample, at an angle of 80°.

Sample preparation for potentiodynamic polarization

Potentiodynamic polarization measurements, where the current response is measured as the cell potential, *V*, is varied, were carried out at room temperature (25°C) using a three-electrode electrochemical cell connected to a *Metrohm Autolab PG potentiostat*. A platinum wire was used as the counter-electrode, silver/silver chloride (Ag/AgCl in 3.0 mol L⁻¹ aqueous KCl) as the reference electrode, and 0.2 mol L⁻¹ aqueous sodium sulfate (Na₂SO₄) as the electrolyte. Samples of polished high-purity aluminum substrates coated with the carbon nanocoating were used for potentiodynamic polarization measurements to evaluate the degree of corrosion protection provided by the carbon multilayer, before and after UV irradiation. An aluminum substrate cleaned by sonication in isopropanol for 10 minutes was used as the reference sample (bare Al). Before each measurement, the open circuit potential (OCP) of the cell, measured with respect to the reference electrode, was monitored for approximately 20 minutes until a stable value was attained. Subsequently, two potential sweeps were applied to the cell: first a smaller potential sweep from -10 mV to +10 mV relative to the OCP, then a larger potential sweep from -0.1 V to +0.2 V relative to the OCP. Both potential sweeps were applied at a scan rate of 1 mV⁻¹.

Analysis of Potentiodynamic Polarization Data

The polarization resistance, R_p , indicative of the sample's corrosion resistance, were determined as the reciprocal of the slope of the linear $I-V$ plot obtained at a small overpotential range of ± 10 mV with respect to the OCP . At a larger overpotential range of -0.1 V to $+0.2$ V, the current responses were plotted on a semi-logarithmic Tafel plot. The anodic and cathodic Tafel constants, β_a and β_c , were extracted from the Tafel curves, and with the R_p , the corrosion current density, i_{corr} , was determined using the Stearn-Geary equation:

$$i_{corr} = \frac{\beta_a \beta_c}{2.3 \times R_p \times (\beta_a + \beta_c) \times A_{WE}}$$

where $A_{WE} = 0.38$ cm² which is the area of the working electrode that was exposed to the electrolyte.

5. Bibliography

1. Zhang, Y. & Yin, Q. Z. Carbon and other light element contents in the Earth's core based on first-principles molecular dynamics, *Proceedings of the National Academy of Science* **27**, 19579-19583 (2012).
2. Nasir, S. *et al.* Carbon-based nanomaterials/allotropes: a glimpse of their synthesis, properties and some applications, *Materials* **11**, 295 (2018).
3. Kroto, H. W., Heath, J. R., O'Brien, S. C., Curl, R. F. & Smalley, R. E. C60: Buckminsterfullerene, *Nature* **318**, 162-163 (1985).
4. Iijima, S. Helical microtubules of graphitic carbon, *Nature* **354**, 56-58 (1991).
5. Iijima, S. & Toshinari, I. Single-shell carbon nanotubes of 1-nm diameter, *Nature* **363**, 603-605 (1993).
6. Bethune, D. S., Kiang, C. H., de Vries, M. S., Gorman, G., Savoy, R., Vazquez, J. & Beyes, R. Cobalt-catalysed growth of carbon nanotubes with single-atomic-layer walls, *Nature* **363**, 605-607 (1993).
7. Boehm, H. P. *et al.* Dünnsche Kohlenstoff-Folien, *Zeitschrift für Naturforschung* **17**, 150-153 (1962).
8. Novoselov, K. S., Geim, A. K. *et al.* Electric field effect in atomically thin carbon films, *Science* **306**, 666-669 (2004).
9. Buntlar, V. & Weber, H. W. Magnetic properties of fullerene superconductors, *Superconductor Science and Technology* **9**, 599-615 (1996).
10. Yu, M.-F. *et al.* Strength and breaking mechanism of multiwalled carbon nanotubes under tensile load, *Science* **287**, 637-640 (2000).
11. Frank, I. W., & Tanenbaum, D. M. Mechanical properties of suspended graphene sheets, *Journal of Vacuum Science & Technology B: Microelectronics and Nanometer Structure Processing, Measurement, and Phenomena* **25**, 2558-2561 (2007).
12. Chuan, X.-Y., Wang, T.-K. & Donnet, J.-B. Stability and existence of carbyne with carbon chains, *New Carbon Materials* **20**, 83-91 (2005).
13. Hayatsu, R., Scott, R. G., Studier, M. H., Lewis, R. S. & Anders, E. Carbynes in meteorites: detection, low-temperature origin, and implication for interstellar molecules, *Science* **209**, 1515-1518 (1980).
14. Jansta, J. & Dousek, F. Some aspects of existence of elementary carbon with sp²-hybridized bonds, *Carbon* **18**, 433-437 (1980).

15. Shi, L. *et al.* Confined linear carbon chains as a route to bulk carbyne, *Nature Materials* **15**, 634-640 (2016).
16. Kastner, J. & Kunzmany, H. Reductive preparation of carbyne with high yield. An *in situ* raman scattering study, *Macromolecules* **28**, 344-353 (1995).
17. Arora, N. & Sharma, N. N. Arc discharge synthesis of carbon nanotubes: comprehensive review, *Diamond and Related Materials* **50**, 135-150 (2015).
18. Moise, C.-C. & Enachescu, M. High-quality carbon nanomaterials synthesized by excimer laser ablation, *Application of laser ablation* (2016).
19. Manawy, Y. M. *et al.* A review of carbon nanomaterials' synthesis via the chemical vapor deposition (CVD) method, *Materials* **11**, 822 (2018).
20. Zhang, Q., Wu, T. C., Kuang, G., Xie, A. & Lin, N. Investigation of edge states in artificial graphene nano-flakes, *J. Phys.: Condens. Matter* **33**, 225003 (2021).
21. Huang, X., Pan, K. & Hu, Z. Experimental demonstration of printed graphene nano-flakes enabled flexible and conformable wideband radar absorber, *Scientific Reports* **6**, 38197 (2016).
22. Narang, J., Malhotra, N., Singhal, C., Bhatia, R., Kathuria, V. & Jain, M. Graphene nanoflakes on transparent glass electrode sensor for electrochemical sensing of anti-diabetic drug, *Bioprocess and Biosystem Engineering* **40**, 537-548 (2017).
23. Müllen, K. Evolution of graphene molecules: structural and functional complexity as driving forces behind nanoscience, *ACS Nano* **8**, 6531-6541 (2014).
24. Simpson, C. D., Müllen, K. *et al.* Synthesis of a giant 222 carbon graphite sheet, *Chemistry – A European journal* **8**, 1424-1429 (2002).
25. Chung, S., Revia, R. A. & Zhang, M. Graphene quantum dots and their applications in bioimaging, biosensing, and therapy, *Advanced Materials* **33**, 19044362 (2021).
26. Yang, Y., Wu, D., Han, S., Hu, P. & Liu, R. Bottom-up fabrication of photoluminescent carbon dots with uniform morphology via a soft-hard template approach, *Chemical Communication* **49**, 4920-4922 (2013).
27. Lee, S. H. *et al.* Synthesis of single-crystalline hexagonal graphene quantum dots from solution chemistry, *Nano Letters* **19**, 5437-5442 (2019).
28. Fresco-Cala, B., Soriano, M. L., Sciortino, A., Cannas, M., Messina, F. & Cardenas, S. One-pot synthesis of graphene quantum dots and simultaneous nanostructured self-assembly via a novel microwave-assisted method: impact on triazine removal and efficiency monitoring, *RSC Advances* **52**, 29939-29946 (2018).
29. Fischer, J. E. & Johnson, A. T. Electronic properties of carbon nanotubes, *Current*

- Opinion in Solid State and Materials Science* **4**, 28-33 (1999).
30. Scott, L. T. Methods for the chemical synthesis of carbon nanotubes: an approach based on hemispherical polyarene templates, *Pure and Applied Chemistry* **89**, 809-920 (2017).
 31. Itami, K. & Maekawa, T. Molecular nanocarbon science: present and future, *Nano Letters* **20**, 4718-4720 (2010).
 32. Ezawa, M. Peculiar width dependence of the electronic properties of carbon nanoribbons, *Physical Review B* **73**, 045432 (2006).
 33. Narita, A., Chen, Z., Chen, Q. & Müllen, K. Solution and on-surface synthesis of structurally defined graphene nanoribbons as a new family of semiconductors, *Chemical Science* **10**, 964-975 (2019).
 34. Yang, W., Lucotti, A., Tommasini, M. & Chalifoux, W. A. Bottom-up synthesis of soluble and narrow graphene nanoribbons using alkyne benzannulations, *Journal of the American Chemical Society* **138**, 9137-9144 (2016).
 35. Márquez, I. R., Castro-Fernández, S., Millán, A. & Campaña, A. G. Synthesis of distorted nanographenes containing seven- and eight-membered carbocycles, *Chemical Communications* **54**, 6705-6718 (2018).
 36. Cai, J. et al., Atomically precise bottom-up fabrication of graphene nanoribbons, *Nature* **466**, 470-473 (2010).
 37. Li, G., Li, Y., Liu, H., Guo, Y., Li, Y. & Zhu, D. Architecture of graphdiyne nanoscale films, *Chemical Communications* **46**, 3256-3258 (2010).
 38. Lopes, L. C. et al. Facile room temperature synthesis of large graphene sheets from simple molecules, *Chemical Science* **9**, 7297 (2018).
 39. Love, J. C., Estroff, L. A., Kriebel, J. K., Nuzzo, R. G. & Whitesides, G. M. Self-assembled monolayers of thiolates on metals as a form of nanotechnology, *Chemical Reviews* **105**, 1103-1170 (2005).
 40. Bomal, E. Carbon materials from oligoyne surfactants, EPF Lausanne (2020).
 41. Nuzzo, R. G. & Allara, D. L. Adsorption of bifunctional organic disulfides on gold surfaces, *Journal of the American Chemical Society* **105**, 4481-4483 (1983).
 42. Vos, J. G., Foster, R. J. & Keyes, T. E. Interfacial supramolecular assemblies, Wiley & Sons (2003).
 43. Shin, H.-J. et al. Transfer-Free Growth of Few-Layer Graphene by Self-Assembled Monolayers. *Advanced Materials* **23**, 4392-4397 (2011).
 44. Turchanin, A. & Götzhäuser, A. Carbon nanomembranes, *Advanced Materials* **28**,

- 6075-6103 (2016).
45. Angelova, P. & Götzhäuser, A. Carbon nanomembranes, *Physical Science Review* **2**, 20160105 (2017).
 46. Li, Z. & Lin, Z. Self-assembly of bolaamphiphiles in 2D nanosheets via synergistic and meticulous tailoring of multiple noncovalent interactions, *ACS Nano* **15**, 3152-3160 (2015).
 47. Israelachvili, J. N., Mitchell, D. J. & Ninham, B. W. Theory of self-assembly of lipid bilayers and vesicles. *Biochimica and Biophysica Acta - Biomembranes* **470**, 185–201 (1977).
 48. Nuraje, N., Bai, H. & Su, K. Bolaamphiphilic molecules: assembly and applications, *Progress in Polymer Science* **38**, 302-343 (2013).
 49. Dhasaiyan, P. & Prasad, B. L. V. Self-assembly of bolaamphiphilic molecules, *The Chemical Record* **17**, 597-610 (2016).
 50. Decher, G. & Hong, J. D. Build-up of ultrathin multilayer films by a self-assembly process: II. Consecutive adsorption of anionic and cationic bipolar amphiphiles and polyelectrolytes on charged surfaces, *Berichte der Bunsengesellschaft für physikalische Chemie* **95**, 1430-1434 (1991).
 51. Wang, Y., Angelatos, A. S. & Caruso, F. Template synthesis of nanostructures materials via layer-by-layer assembly, *Chemistry of Materials* **20**, 848-858 (2008).
 52. Lee, H., Kepley, L. J., Hong, H. G., Akhter, S. & Mallouk, T. E. Adsorption of ordered zirconium phosphonate multilayer films on silicon and gold surfaces, *Journal of Physical Chemistry* **92**, 2597-2601 (1988).
 53. Stockhause, S. et al. Organic/inorganic functional materials for light-emitting devices based on conjugated bisphosphonates, Wiley (2003).
 54. Kang, D. W., Nam, T. G., Kim, E.-R., Lee H. L. D.-R. & Lee, K. B. Self-assembly of metal (IV) alkyldylbisphosphonate multilayer films on gold and silicon substrates, *Molecular Crystals and Liquid Crystals* **295**, 193-196 (1997).
 55. Hamoudi, H., Berdiyrov, G. R., Ariga, K. & Esaulov, V. Bottom-up fabrication of the multi-layer carbon metal nanosheets, *RCS Advances* **10**, 7989-7993 (2020).
 56. Tahir, M. N., Nyayachavadi, A., Morin, J. F. & Rondeau-Gagné, S. Recent progress in the stabilization of supramolecular assemblies with functional polydiacetylenes. *Polymer Chemistry* **9**, 3019–3028 (2018).

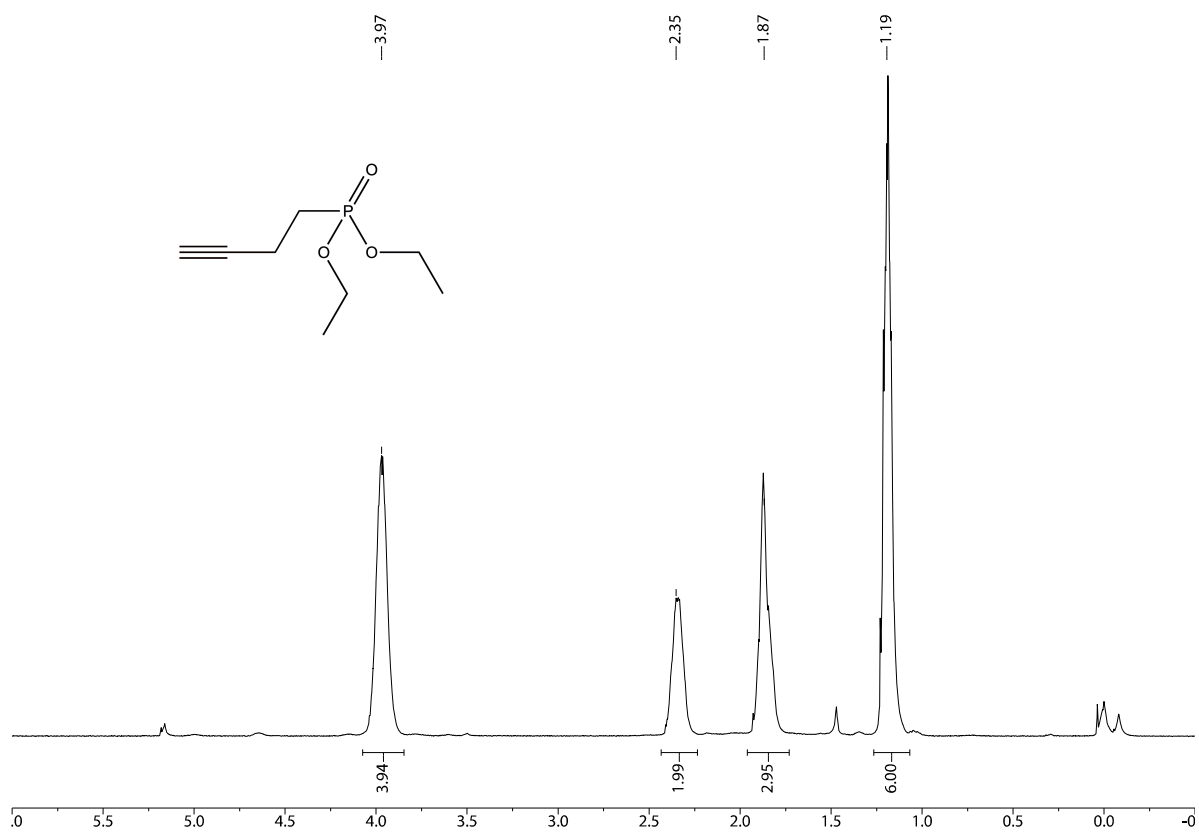
57. Hlavatý, J., Kavan, L., Kasahara, N. & Oya, A. Polymerisation of 1-iodohexa-1,3,5-triyne and hexa-1,3,5-triyne: a new synthesis of carbon nanotubes at low temperatures, *Chemical Communications*, 737–738 (2000).
58. Ding, L. & Olesik, S. V. Synthesis of Polymer Nanospheres and Carbon Nanospheres Using the Monomer 1,8-Dihydroxymethyl-1,3,5,7- octatetrayne. *Nano Letters* **4**, 2271–2276 (2004).
59. Eisler, S., Slepko, A. D., Elliott, E., Luu, T., McDonanld, R., Hegmann, F. A. & Tykwinski, R. R. Polyynes as a model for carbyne: synthesis, physical properties, and nonlinear optical response, *Journal of the American Chemical Society* **127**, 2666-2676 (2005).
60. Enkelmann, V. Structural Aspects of the Topochemical Polymerization of Diacetylenes. *Advanced Polymer Science* **63**, 91–136 (1984).
61. Shi Shun, A. L. K., & Tykwinski, R. R. Synthesis of naturally occurring polyynes, *Angewandte Chemie International Edition* **45**, 1034-1057 (2006).
62. Zidorn, C. *et al.* Polyacetylenes from the Apiaceae Vegetables Carrot, Celery, Fennel, Parsley, and Parsnip and Their Cytotoxic Activities, *Journal of Agricultural and Food Chemistry* **53**, 2518–2523 (2005).
63. Block, E., Guo, C., Thiruvazhi, M. & Toscano, P. J. Total Synthesis of Thiarubrine B [3-(3-Buten-1-ynyl)-6-(1,3-pentadienyl)-1,2-dithiin], the Antibiotic Principle of Giant Ragweed (*Ambrosia trifida*), *Journal of the American Chemical Society* **116**, 9403–9404 (1994).
64. Gläser, C. Beiträge zur Kenntniss des Acetylenylbenzols, *Berichte der deutschen chemischen Gesellschaft* **2**, 422-424 (1869).
65. Eglinton, G. & Galbraith, A. R. 182. Macrocyclic acetylenic compounds. Part I. Cyclotetradeca-1 :3-diyne and related compounds, *Journal of the Chemical Society*, 889-896 (1959).
66. Hay, S. A. Oxidative Coupling of Acetylenes. II, *Journal of Organic Chemistry* **27**, 3320–3321 (1962).
67. Cadiot, P. & Chodkiewicz, W. Chemistry of Acetylenes, Viehe, H. G. Ed., 597–647 (1969).
68. King, A. O., Okukado N. & Negishi, E. Highly general stereo-, regio-, and chemo-selective synthesis of terminal and internal conjugated enynes by the Pd-catalysed reaction of alkynylzinc reagents with alkenyl halides, *Chemical Communications* **19**, 683-684 (1977).

69. Simpkins, S. M. E., Weller, M. D. & Cox, L. R. β -Chlorovinylsilanes as masked alkynes in oligoyne assembly: synthesis of the first aryl-end-capped dodecayne, *Chemical Communications* **39**, 4035-4037 (2007).
70. Schrettl, S., Contal, E., Hoheisel, T. N., Frtizsche, M., Balog, S., Szilluweit, R. & Frauenrath, H. Facile synthesis of oligoyne amphiphiles and their rotaxanes, *Chemical Science* **6**, 564-574 (2015).
71. Bomal, E., Croué, V., Yeo, R., Scopelliti, R. & Frauenrath, H. Hexayne Amphiphiles and Bolaamphiphiles, *Chemistry – A European Journal* **26**, 8907-8915 (2020).
72. Schrettl, S. *et al.*, Functional carbon nanosheets prepared from hexayne amphiphile monolayers at room temperature, *Nature Chemistry* **6**, 468-476 (2014).
73. Yeo, R. *et al.*, Solution-borne protective carbon monolayer coatings, *to be published*
74. Murphy, P. J. *Organophosphorus reagents: a practical approach in chemistry*, Oxford University Press (2004).
75. Chalifoux, W. A. & Tykwinski, R. R. Synthesis of polyynes to model the sp-carbon allotrope carbyne. *Nature Chemistry* **2**, 967–971 (2010).
76. Jahnke, E., Weiss, J., Neuhaus, S., Hoheisel, T. N. & Frauenrath, H. Synthesis of diacetylene-containing peptide building blocks and amphiphiles, their self-assembly and topochemical polymerization in organic solvents, *Chemistry – A European Journal* **15**, 388-404 (2009).
77. Banhart, F. Elemental carbon in the sp hybridization, *Chemtext* **6** (2019).
78. Matsutani, R., Inoue, K., Wada, N. & Kojima, K. Wavelength dependence of polyyne preparation by liquid-phase laser ablation using pellet targets, *Chemical Communications* **47**, 5840-5842 (2011).
79. Zirzmeier, J. *et al.* Optical gap and fundamental gap of oligoynes and carbyne, *Nature Communications* **11**, 4797 (2020).
80. Pathak, A. *et al.* Disorder-derived, strong tunneling attenuation in bis-phosphonate monolayers, *Journal of Physics of Condensed Matter* **28**, 094008 (2016)
81. Bauer, T., Schmaltz, T., Lenz, T., Halik, M., Meyer, B. & Clark, T. Phosphonate- and carboxylate-based self-assembly monolayers for organic devices: a theoretical study of surface binding on aluminum oxide with experimental support, *Applied Material Interfaces* **5**, 6073-6080 (2013).
82. Maxisch, M., Thissen, P., Giza, M. & Grundmeier, G. Interface chemistry and molecular interactions of phosphonic acid self-assembled monolayers on oxyhydroxide-covered aluminum in humid environment, *Langmuir* **27**, 6042-6048

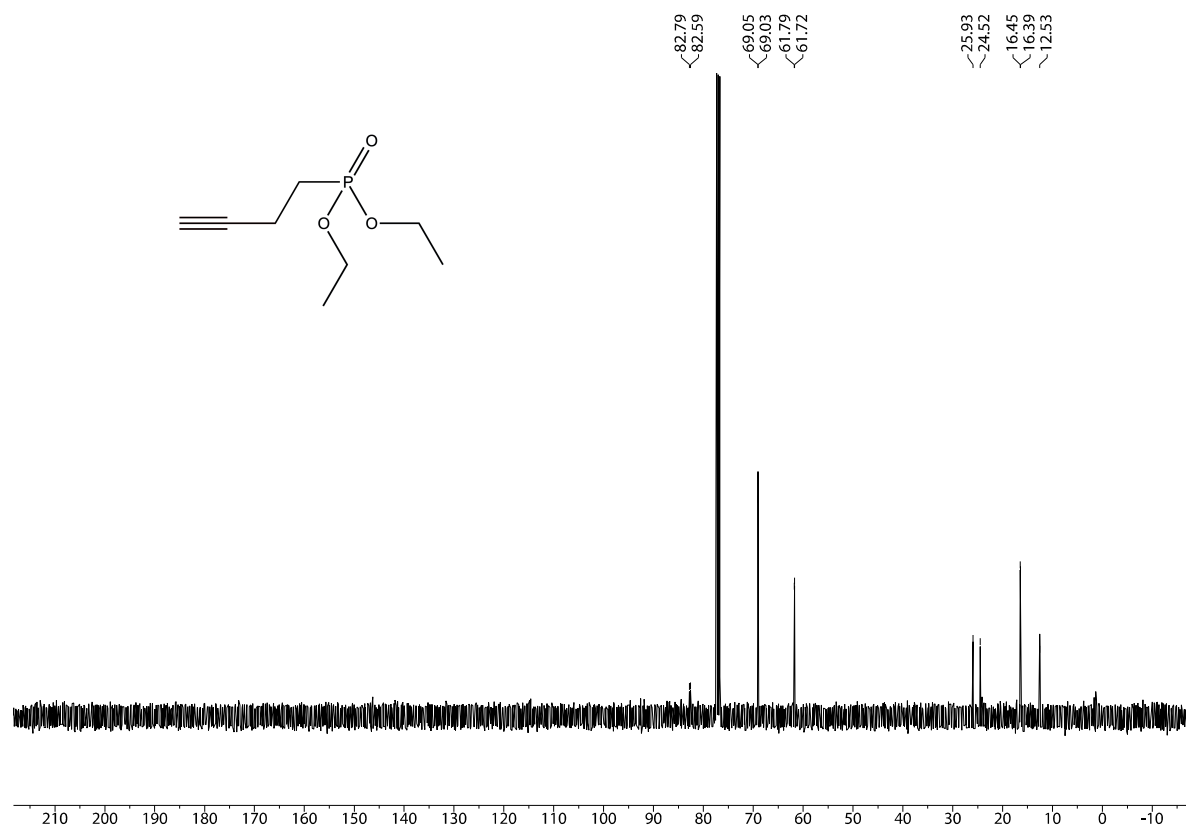
(2011).

83. Ferrari, A. C. & Robertson, J. Interpretation of Raman spectra of disordered and amorphous carbon, *Physical Review B* **61**, 14095-14107 (2000).

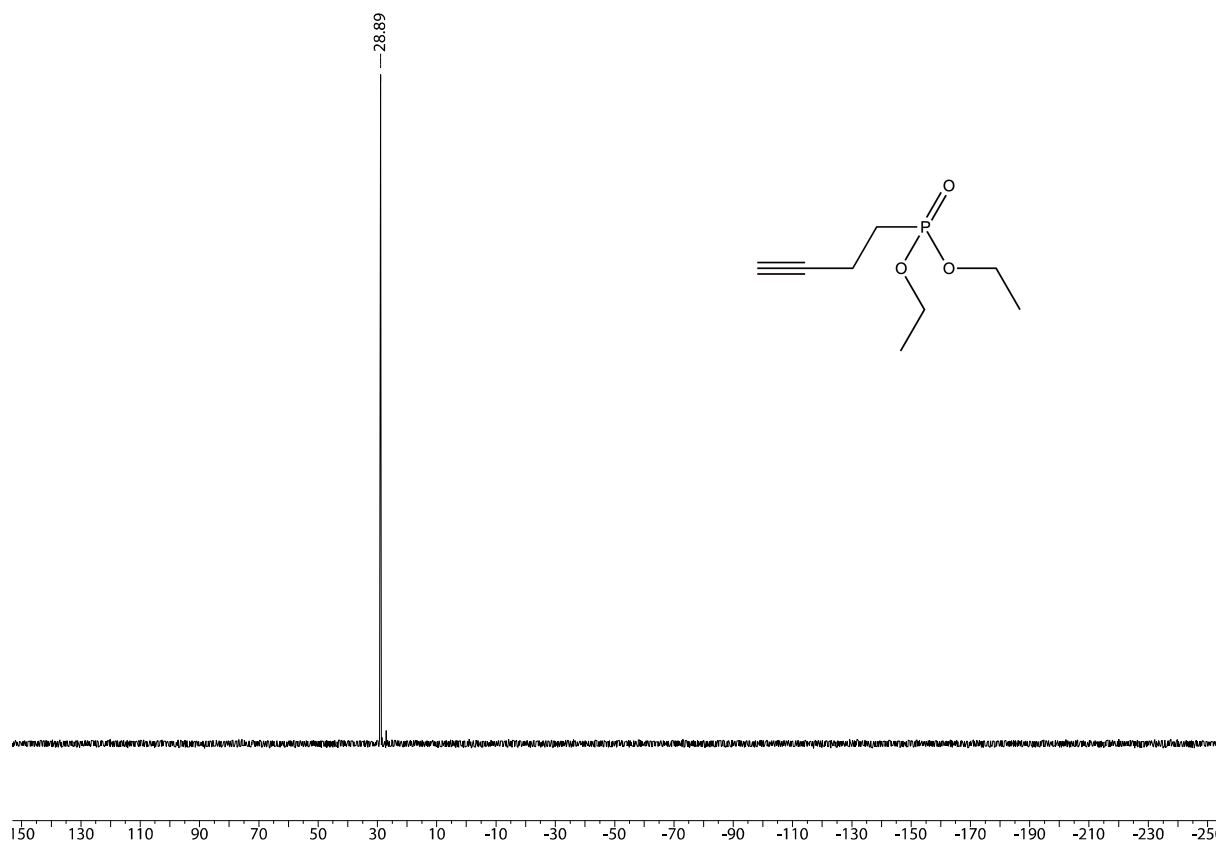
6. Appendix



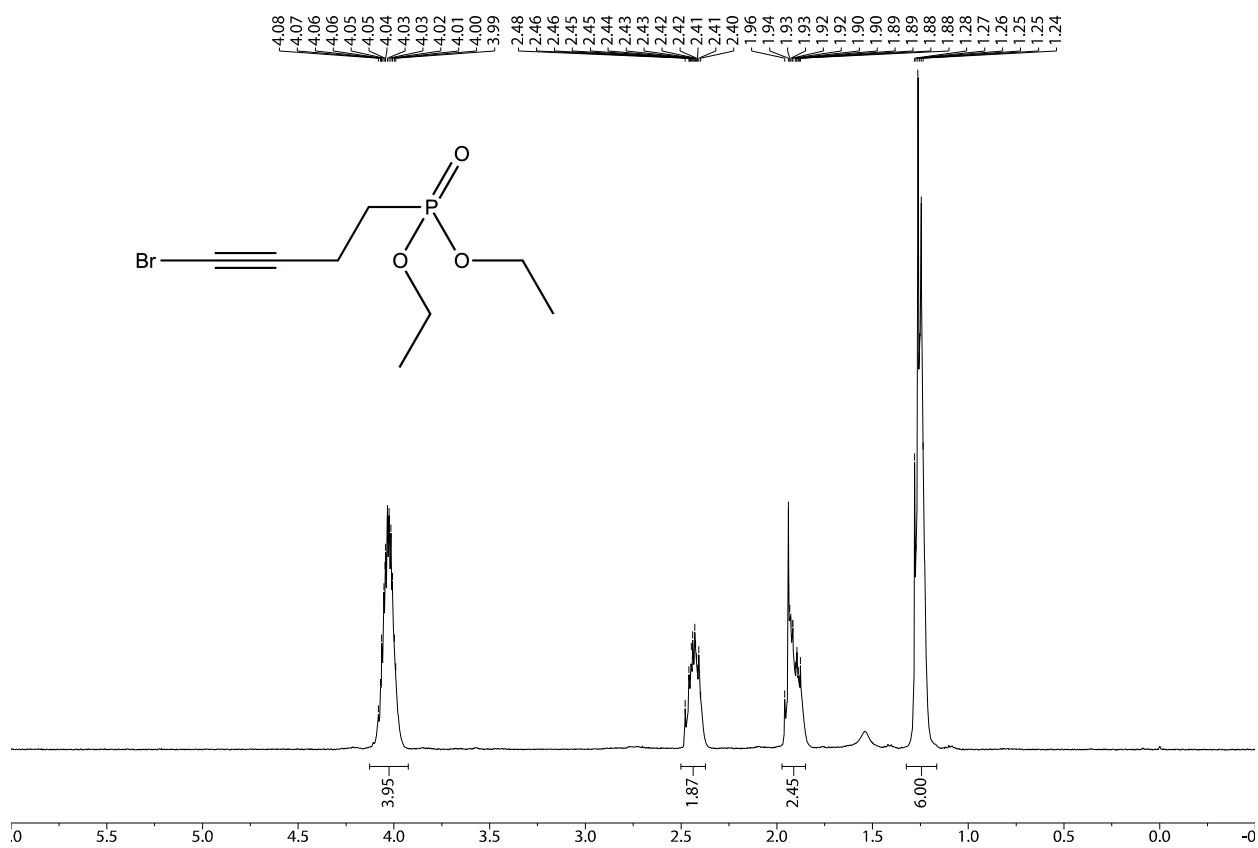
Appendix Figure 1: $^1\text{H-NMR}$ spectrum of **2** (400 MHz, CDCl_3).



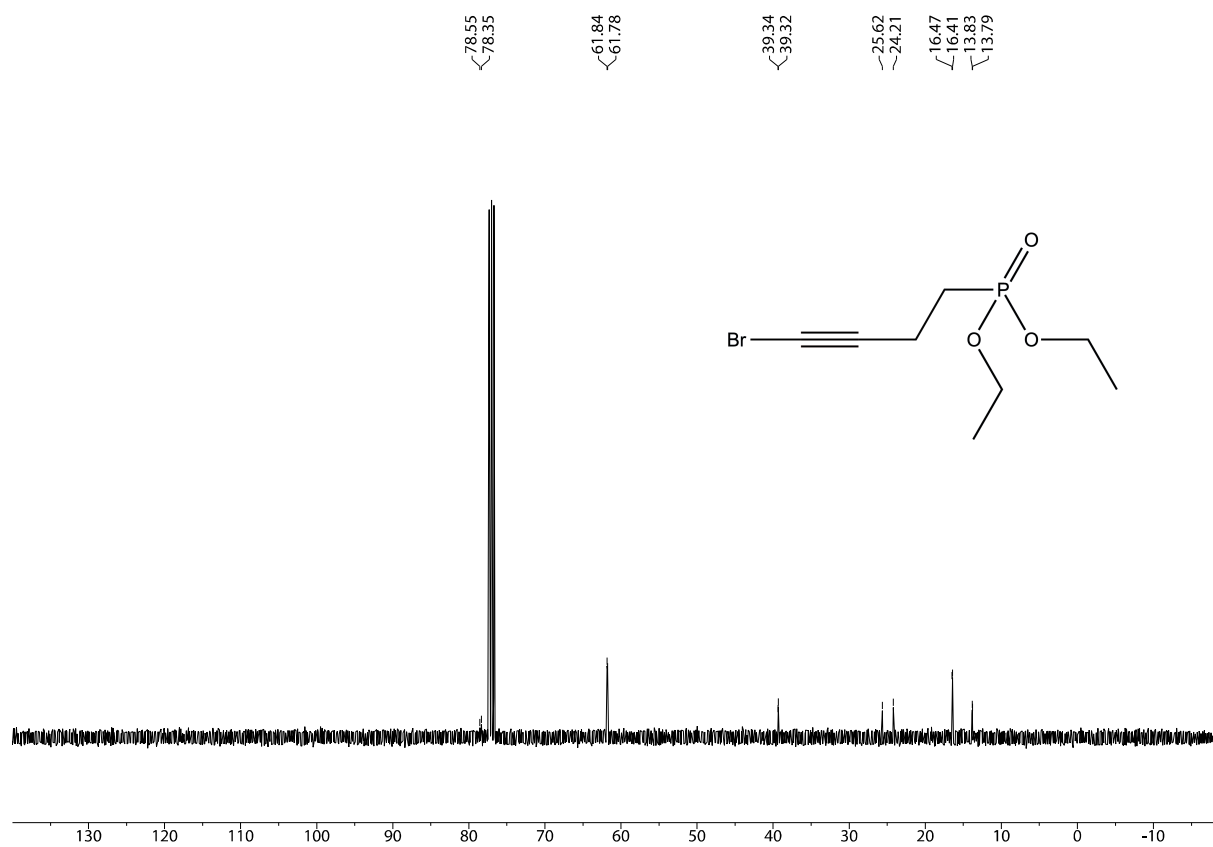
Appendix Figure 2: $^{13}\text{C-NMR}$ spectrum of **2** (101 Mhz, CDCl_3).



Appendix figure 3: ^{31}P -NMR spectrum of 2 (162 Mhz, CDCl_3)



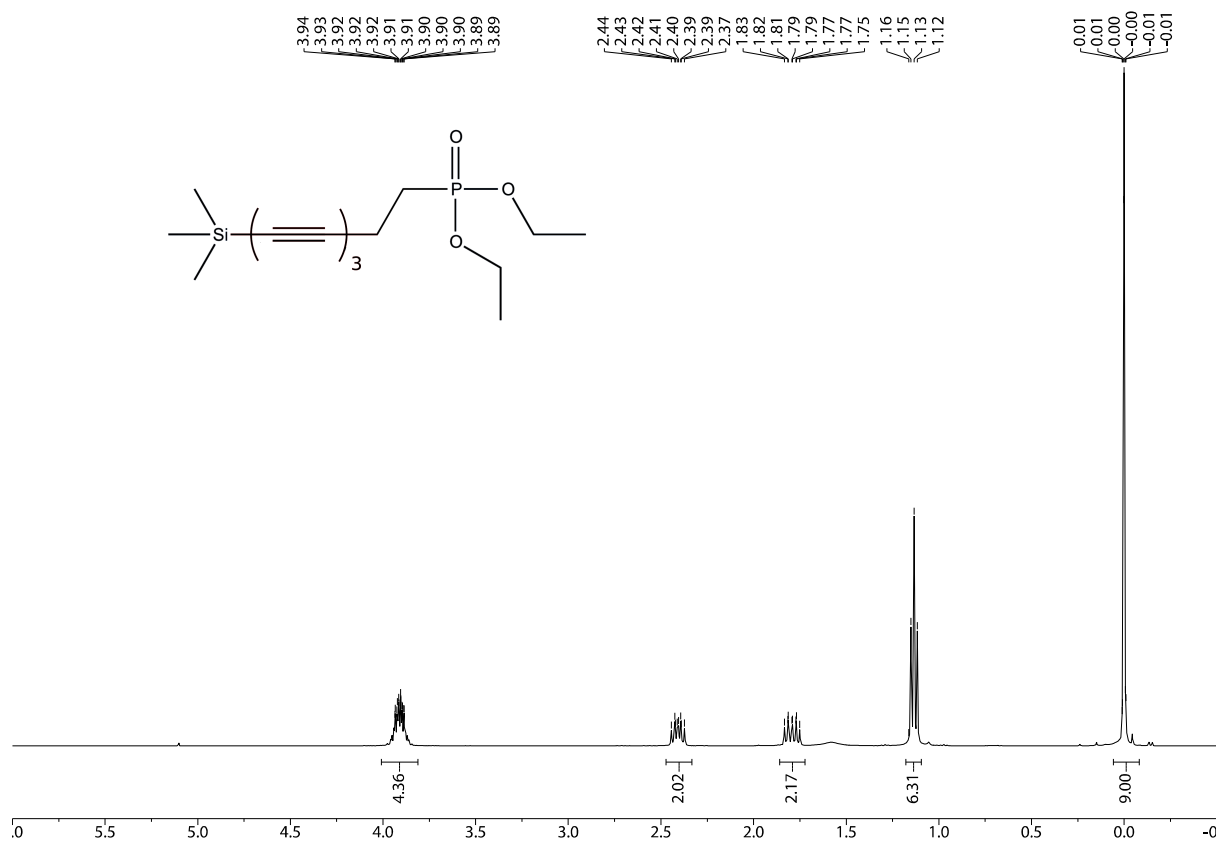
Appendix Figure 1: ^1H -NMR spectrum of 3 (400 MHz, CDCl_3).



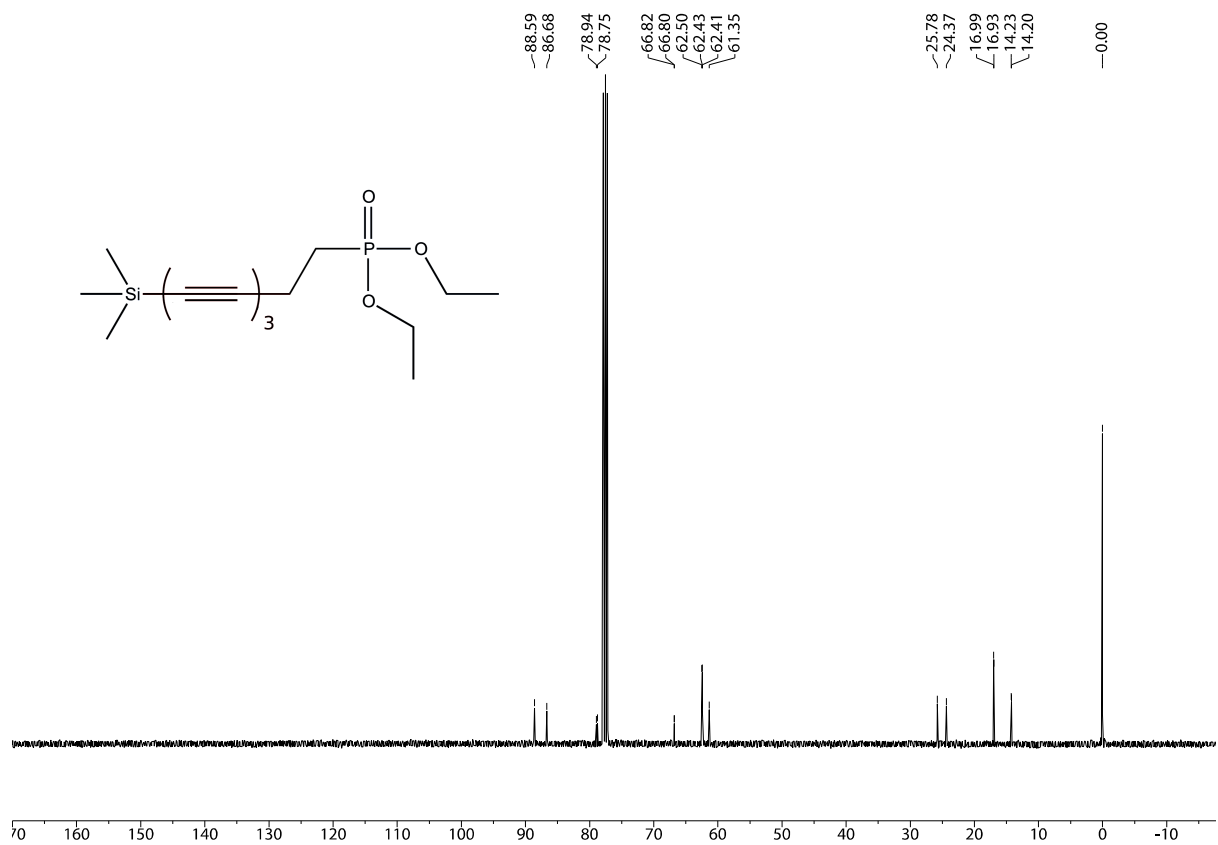
Appendix Figure 5: ^{13}C -NMR spectrum of **3** (101 MHz, CDCl_3).



Appendix figure 6: ^{31}P -NMR spectrum of **3** (162 MHz, CDCl_3).



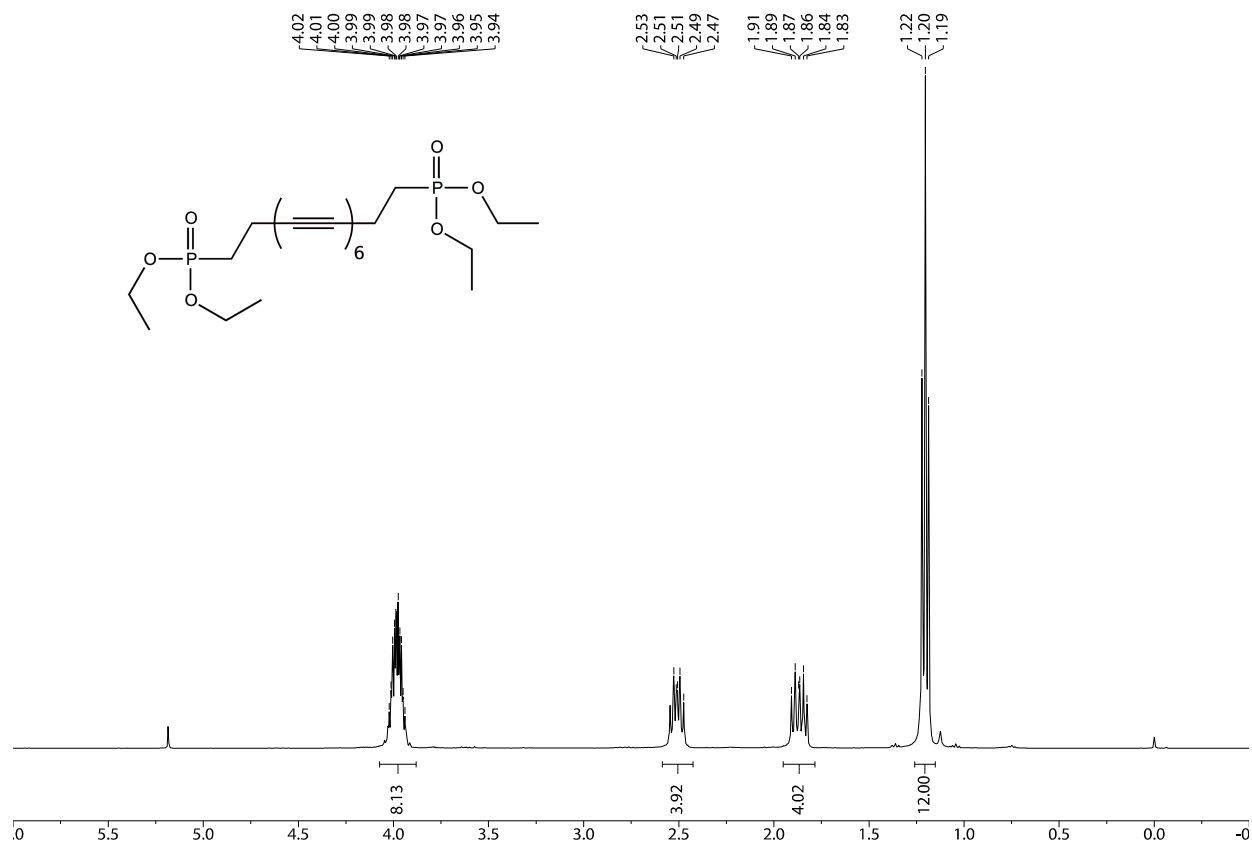
Appendix figure 7: ¹H-NMR spectrum of **4** (400 MHz, CDCl₃).



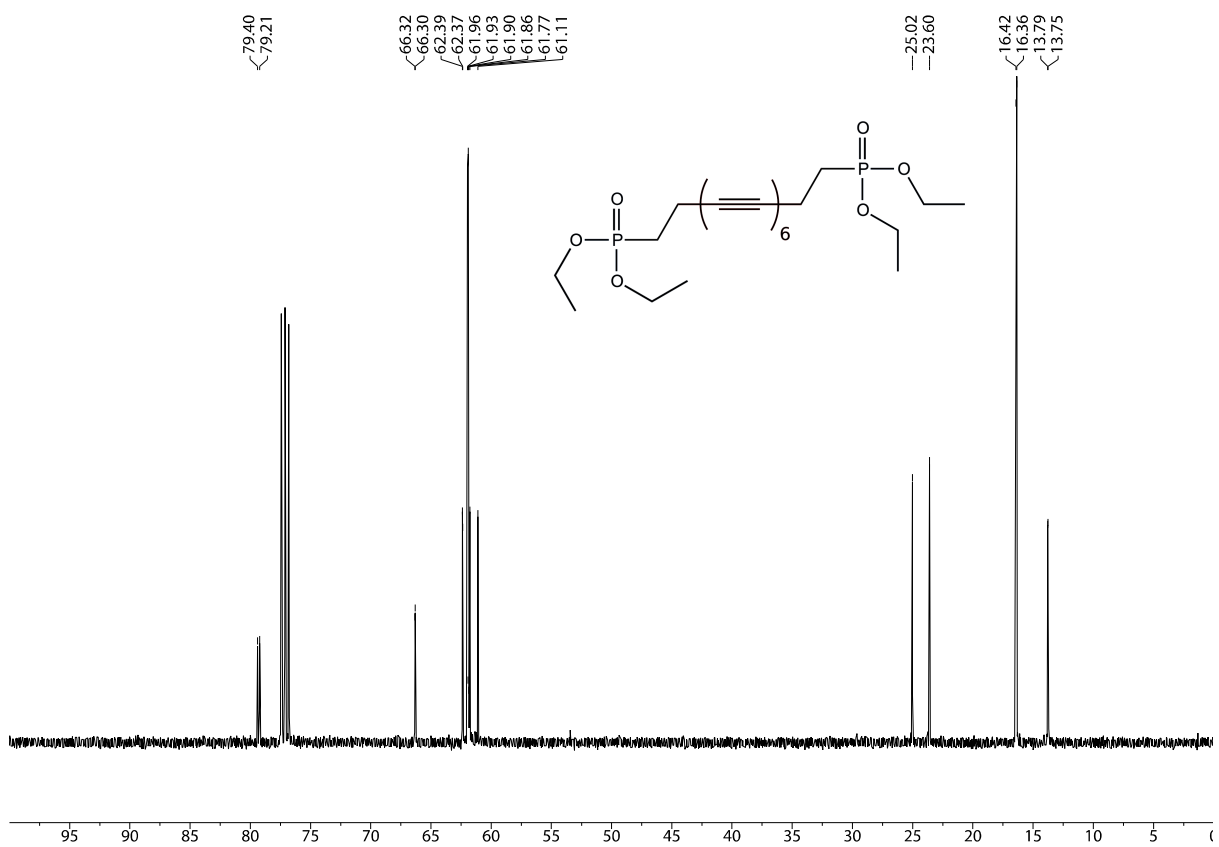
Appendix figure 8: ¹³C-NMR spectrum of **4** (101 MHz, CDCl₃).



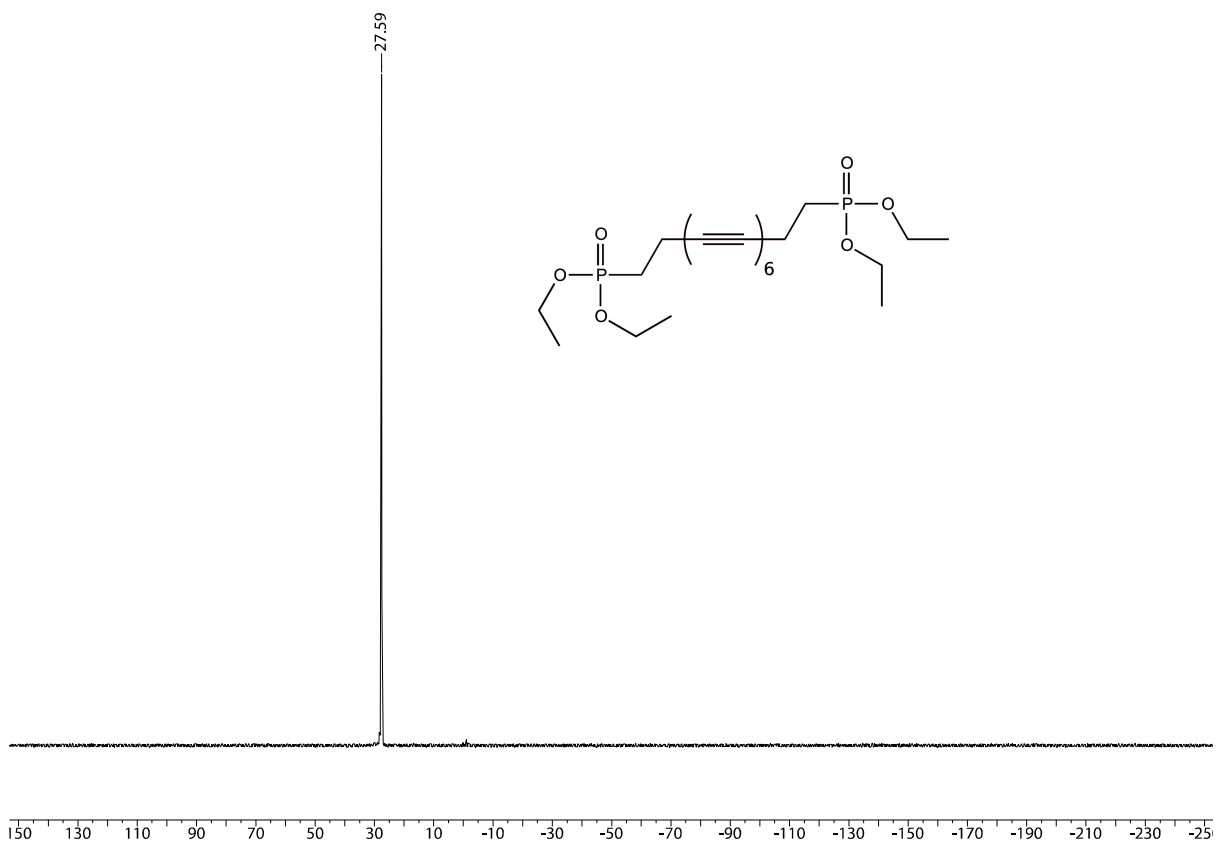
Appendix figure 9: ^{31}P -NMR spectrum of 4 (162 MHz, CDCl_3).



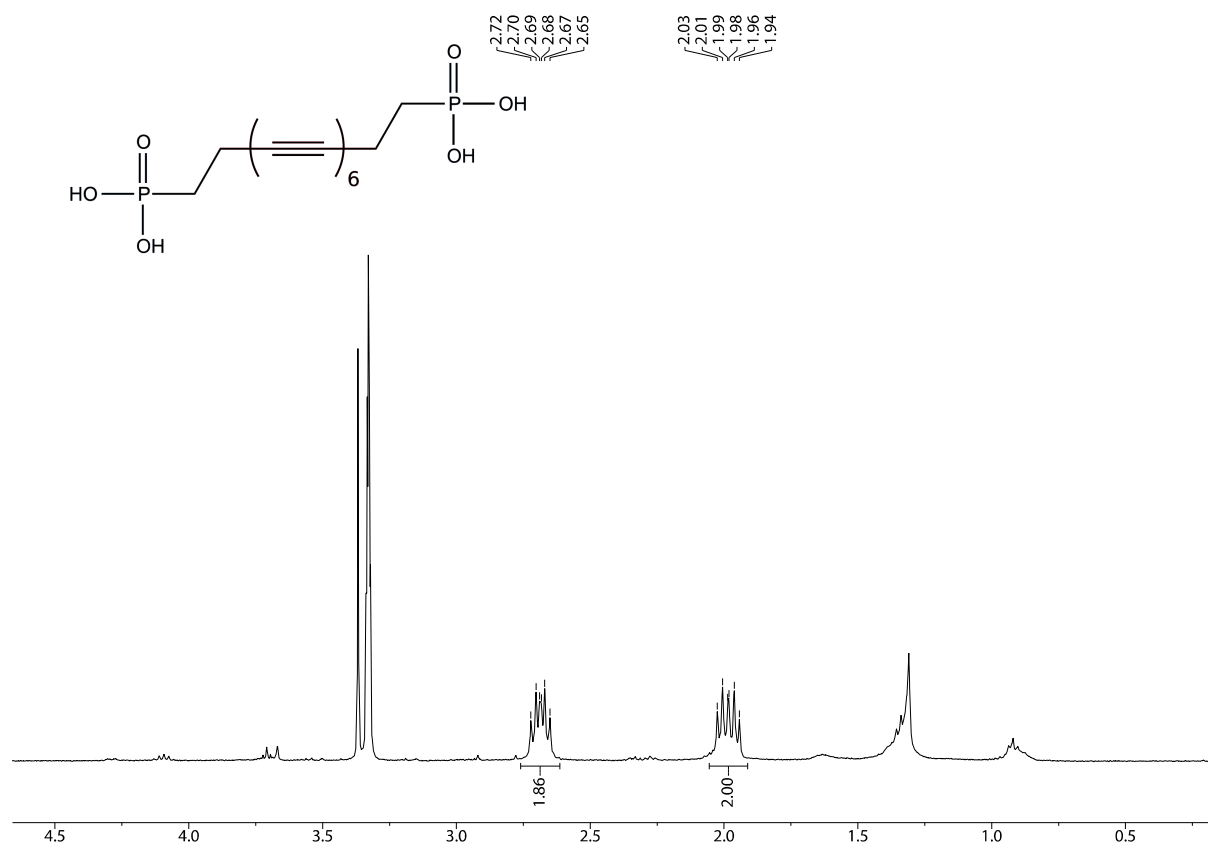
Appendix figure 10: ^1H -NMR spectrum of 5 (400 MHz, CDCl_3).



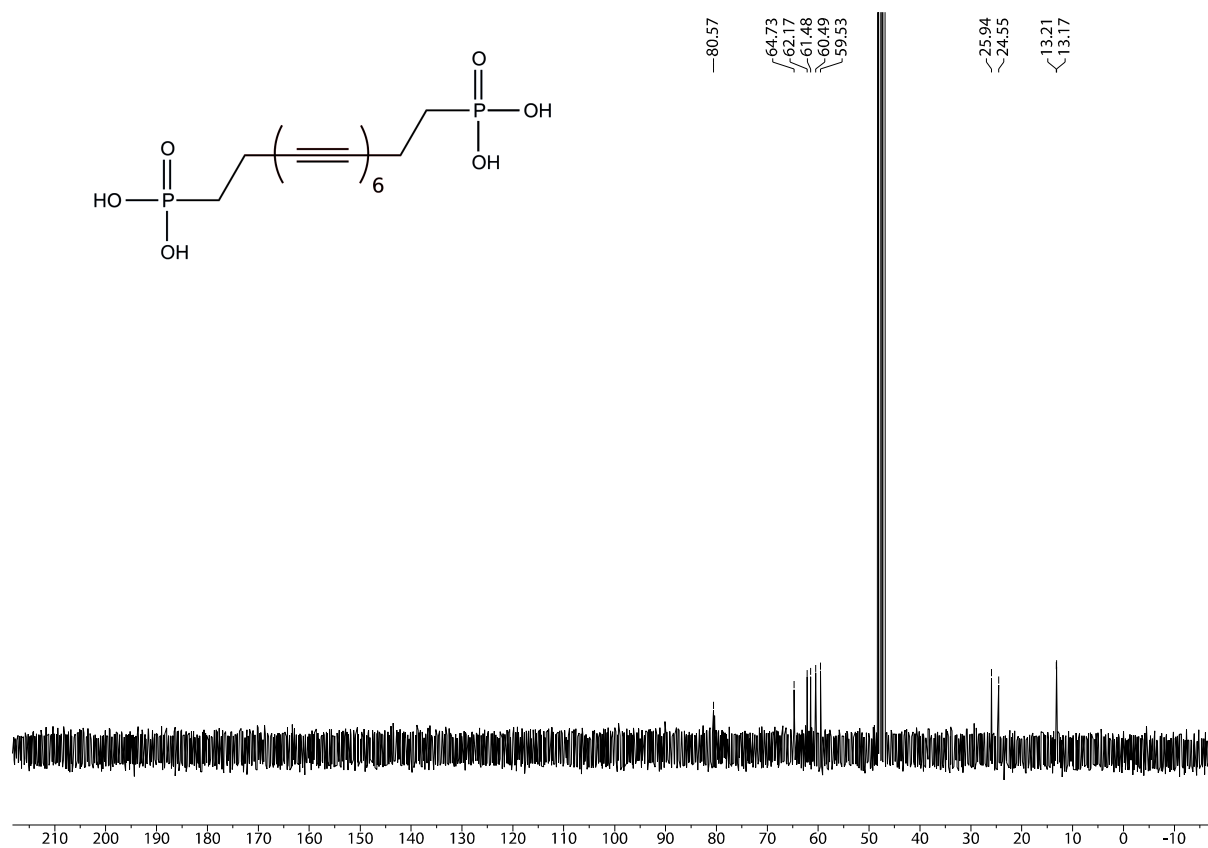
Appendix figure 10: ^{13}C -NMR spectrum of **5** (101 MHz, CDCl_3).



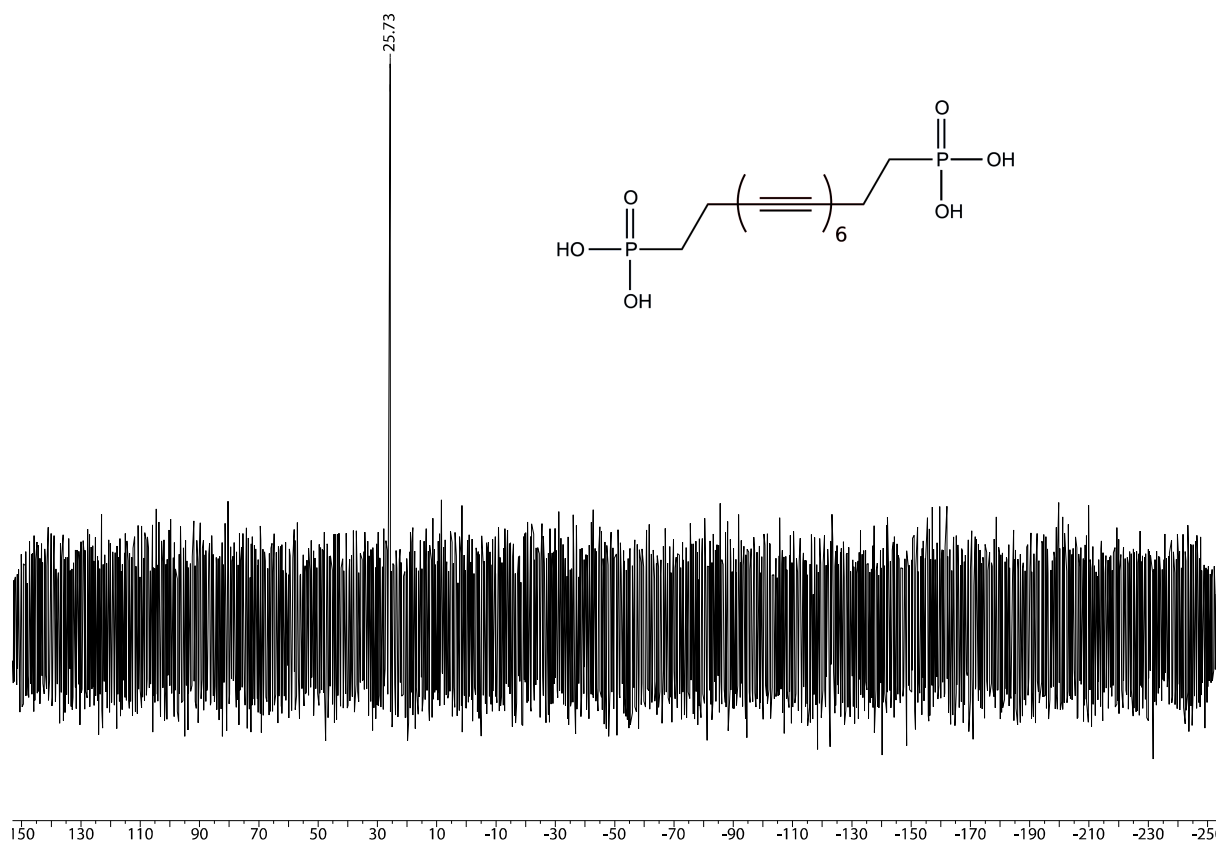
Appendix figure 12: ^{31}P -NMR spectrum of **5** (162 MHz, CDCl_3).



Appendix figure 13: ^1H -NMR spectrum of **6** (400 MHz, MeOD).



Appendix figure 14: ^{13}C -NMR spectrum of **6** (101 MHz, MeOD).



Appendix figure 15: ³¹P-NMR spectrum of **6** (162 MHz, MeOD).